BENCHMARKING OF MCNP MODELLING OF HTR CORES AGAINST EXPERIMENTAL DATA FROM THE ASTRA CRITICAL FACILITY

Z Zibi

20229127

Final

Dissertation submitted in partial fulfilment of the requirements for the degree of Master of Science in Engineering Science in Nuclear Engineering at the Potchefstroom Campus of the North-West University

Supervisor: Mr F Albornoz

May 2010

ABSTRACT

The subject of this dissertation is to validate a developed MCNP model of the ASTRA critical facility, through performing comparisons with experimental reactor physics parameters. This validation effort, along with others found in the literature that are focused both on the physics models embedded in MCNP and on the MCNP models of experiments, will help provide the basis for confidence in the use of the code. At PBMR, MCNP, along with other extensively used nuclear engineering computational tools help in the support of the design and eventually the definition of passive safety case for a High Temperature Reactor (HTR). The ASTRA critical facility was chosen as the basic analysis system for this work; with experimental results made available through an Eskom-Kurchatov Institute contract aimed at investigating some PBMR-neutronic characteristics.

The availability of the ASTRA experimental set-up information, executed experimental results and some code comparisons presents a very good opportunity for PBMR to validate its own computational tools as per the outcome of the contract collaboration between the two. Some of the experiments performed in support of the investigation of PBMR neutronic characteristics included the study of critical parameters, control rod worths, neutron and power spatial distributions (axial and radial) and reactivity effects.

The Monte Carlo n-particle transport code MCNP5 was used to perform all the analyses reported in this work. The findings of this thesis indicate that considering the experimental tasks analysed for the ASTRA critical facility Configuration No. 1 using our MCNP5 consideration (code, modelling approach and used cross section set), there is a relatively good prediction of experimental results (nuclear physics parameters), with control rod reactivity results in particular very well predicted, despite an overestimation in criticality of the modelled experimental configuration. However, there are areas of concern, both experimentally and in our MCNP5 consideration (both for reactivity and reaction rate results).

Concerning the experimental uncertainty, the MCNP5 results for the last side reflector block seem to consistently lack agreement with their experimental counterparts (something that is also seen from the Kurchatov Institute's computational tools used to calculate the same results), leading us to consider a lack of precise experimental information to be behind our models not being representative enough of the experimental set-up. On the model uncertainty, the arrangement of moderator, fuel and absorber spheres in the reactor cavity (particularly the core region) and the neutron flux spectrum and profiles throughout the assembly need to be further investigated in future.

This MCNP model validation effort for the ASTRA critical facility reports promising results, albeit not complete, as indicated above, and also a need to study further ASTRA critical facility configurations in order to make a final decision about MCNP5's suitability in modelling and performing nuclear engineering analysis on HTR cores.

DECLARATION

I, the undersigned, hereby declare that the work contained in this project is my own original work.

Zukile Zibi

Date: 23 February 2010

Centurion

ACKNOWLEDGMENTS

I would like to first and foremost pay my dues to the Almighty God whom I believe strongly that without, I would be no more. It is by Your Grace, Aid and Love that this project has been able to come to its completion in the manner it has, with everyone close to me contributing and providing support. For that and hopefully many blessings to follow from You, I say Thank You (Ndiyabulela).

This has been a draining, time-consuming, and a hugely rewarding task not only for me, but also my ever on point and supportive supervisor, Mr Felipe Albornoz. Let me say that I appreciate every discussion, comment, difficulty and resolution we went through together. I have personally learned a whole lot from you in most of my professional life at PBMR and will certainly carry that going forward as a professionally assured and content person.

I would also like to extend a word of thanks to the PBMR management and colleagues who contributed directly and indirectly in the project. People like Coenie Stoker (NEA Manager), Ronald Sibiya (NRT Sectional Manager) and Sharon Candasamy (Business Unit Training Manager) deserve a special mention amongst a host of others in showing unwavering support and providing me the time for performing various project activities. I would also like to thank the following colleagues; Sergio Korochinsky, Jeetesh Keshaw, Eric Dorval, Volkan Seker, Reuben Makgae, Oscar Zamonsky, Steven Maage, Sandy van der Merwe, and all those I might have missed mentioning, for their insights, discussions, support, editing, etc. during the duration of this project.

I would like to thank the IAEA and NNR for all the coordination effort on activities of the ASTRA critical facility experiment analysis, which are now being compiled as an official Tecdoc report. Diana Naidoo, Frederik Reitsma, Bismark Tyobeka and others are behind all of this and I would like to thank them for their efforts.

I would like to also thank the North-West University lecturers for the learning gained and the administration department for its help covering the duration of the project, with a special mention to the following people: Christel Eastes, Elmari Bester, Leanie du Plessis, Lillian van Wyk, and Susan Coetzee.

My sincere thanks go to my wife Theoline Mandilakhe Zibi for all her love and support during this journey, you deserve a large piece of credit for this work. I would like to also thank the inquisitive questions from Sisipho and Zandile (our two daughters) during some of the long nights and sometimes weekends at work.

CONTENTS

FIGURES

TABLES

ABBREVIATIONS

This list contains the abbreviations used in this document.

Abbreviation or Acronym	Definition
ANS	American Nuclear Society
AS	Absorber Sphere
atm	atom
AVR	*Arbeitsgemeinschaft Versuchsreaktor* (German for Jointly-operated Prototype Reactor)
BCC	Body Centred Cubic
BR	Bottom Reflector
CDF	Cumulative Distribution Function
CR	Centre Reflector
CR	Control Rod
FCC	Face Centred Cubic
FFMC	Fundamental Formulation of Monte Carlo
FS	Fuel Sphere
GT-MHR	Gas Turbine Modular High-temperature Reactor
HCP	Hexagonal Closed Packed
HTGR	High Temperature Gas-cooled Reactor
HTR	High Temperature Reactor
HTR-Modul	High-temperature Reactor – Modul
IAEA	International Atomic Energy Agency
ICSBEP	International Criticality Safety Benchmark Evaluation Project
IRR	Inner Reflector
MCNP	Monte Carlo N-particle Transport Code
MR	Manual Rod
MS	Moderator Sphere
NEA	Nuclear Energy Agency
NNR	National Nuclear Regulator (RSA)
No.	Number
NRT	Nuclear and Radiation Transport
OECD	Organization for Economic Co-operation and Development
PBMR	Pebble Bed Modular Reactor
PC	Personal Computer
PCD	Pitch Circle Diameter
PDF	Probability Distribution Function
PF	Packing Fraction
PIR	Pribor Izmereviya Reaktivnosti (Device for Measurement of Reactivity)
ppm	parts per million
PRNG	pseudo-random’ number generator

Abbreviation or Acronym	**Definition**
PWR	Pressurized Water Reactor
PyC	Pyrolytic Carbon
RD	Requirements Document (NNR)
RN	Random Number
RNG	Random Number Generator
RRC-KI	Russian Research Centre ‘Kurchatov Institute’
RV	Random Variable
SiC	Silicon Carbide
SR	Safety Rod
TBD	To be Determined
TR	Top Reflector
TRISO	Triple Coated Isotropic Particle
u	Atomic Mass Unit
UK	United Kingdom of Great Britain and Northern Ireland
US	User Specified
USA	United States of America
V&V	Verification and Validation
VGR	High-Temperature Gas-graphite Reactor
VRT	Variance Reduction Techniques=
VSOP	Very Superior Old Program

INTRODUCTION

.1 OVERVIEW AND BACKGROUND

The Pebble Bed Modular Reactor (PBMR) is a high-temperature gas-cooled reactor type that is graphite-moderated and fuelled (on-line) by spherical fuel elements containing coated particle uranium dioxide kernels. The core is arranged in an annular cylinder which is surrounded by a fixed graphite central column and by side, top and bottom graphite reflectors. The German High-temperature Gas-cooled Reactor (HTGR) programme, characterized by the Arbeitsgemeinschaft Versuchsreaktor (AVR) and subsequently the HTR-Modul, amongst other reactor designs, serve as the prototypes on which PBMR technology is based [1]. The current PBMR work is aimed at retaining all the safety aspects demonstrated by the AVR, while refining a cycle design that will address commercial viability in various markets (energy, process heat, etc.).

The Pressurized Water Reactor (PWR) design concept forms the basis of nuclear reactor deployment in the world, making up 73.6% of all (519) commercial nuclear power plants (referring to operable, under construction, or on-order reactors as of 31 December 2008). The footprint of HTGRs represents 3.47% (all gas-cooled reactor types from the UK) [2]. It is clear that the deployment of the HTGR type has not been as aggressive as that of the PWR; however, future deployment looks promising since in the past decade many more countries have shown renewed interest in this concept once more, mainly due to its safety aspects and flexibility (energy and process heat applications).

In support of the design and the passive safety case of a PBMR, various analysis groups are tasked to resolve and provide insight on some specific nuclear physics characteristics of the reactor. The groups perform their analysis utilizing various nuclear engineering analysis methods which are built into relevant computer codes. Some of the calculations performed with such codes focus on the following calculation examples: shielding, economical (e.g. material optimization), and system criticality which entails the determination of the system neutron multiplication factor. Due to more deployment and subsequently more design and operating experience of the PWR design concept, most nuclear engineering codes have been developed around this reactor type.

In utilizing the various codes, particularly in the nuclear environment, it is very important to ensure that each code used meets the standard Verification[a] and Validation[b] (V&V) requirements as outlined by the relevant regulatory organizations. The V&V of codes used in design and support of a nuclear plant are of utmost importance to all recognized nuclear engineering companies worldwide. The PBMR-specific computer code licensing requirements are outlined in the National Nuclear Regulator (NNR) requirements document [3]. It should be noted that the V&V process is quite extensive; therefore this investigation does not cover all the aspects but aids in its set-up by addressing the validation step of the ASTRA facility model.

Most of the available commercial computer codes used for nuclear reactor design and support applications have already been through an extensive verification and validation process, with supporting detailed V&V documentation distributed with the code package. The individual licensing of

---

[a] **Verification** is the process of ensuring that the controlling physical equations have been correctly translated into computer code, or in the case of hand calculations, correctly incorporated into the calculational procedure. For the purposes of this document, verification is taken to be part of the verification submission [3].

[b] **Validation** is defined as the evidence that demonstrates that the code or calculational method is fit for its purpose. When calculating physical processes, it may mean showing that the calculation is bounding with a suitable degree of confidence rather than a best estimate [3].

these codes in the area of use, whether the code is being used for analysis in a PWR or HTGR environment, is a delicate consideration which must still be addressed.

.2 MOTIVATION FOR THE RESEARCH PROJECT

The PBMR design process and operation needs to be carried out in a manner that demonstrates no potential danger to the environment at large. This is particularly important in the plant safety case and subsequent licence application to the NNR. In order to answer questions related to the plant design safety, a number of analyses are required. These analyses are normally carried out using a number of specific nuclear reactor design computational tools. Previous knowledge of similar reactor plants and their operational results helps to build a credible comparison base (benchmarks) for the computational tools to be evaluated against.

The codes used in the nuclear environment face strict safety regulations, since their outputs are used for nuclear licensing purposes in an environment that has potentially severe consequences. The NNR must be satisfied that the code validation submissions cover the complexity and level of understanding of the phenomena and processes involved, and the degree of extrapolation from experiment or practical experience to the situation being modelled, particularly for codes that are more important to the safety case basis [3].

In order to meet the NNR regulations regarding PBMR's licence application (to construct and operate a PBMR plant), it should be demonstrated that similar designs to that of PBMR can be modelled and analysed using the same computational tools, resulting in good agreement between benchmark experimental and calculational results. This demonstration covers the computational tool's validation leg of the V&V process. The V&V process of PBMR's computational tools is on-going and receives high priority.

The motivation for this research project is the need to help contribute towards the current PBMR V&V effort; as mentioned above. This project will address aspects related to the validation leg of the V&V process. This will include highlighting the evidence (the ability to get good agreement between experiments and calculations) that demonstrates that, for the considered reactor physics codes, the used code, its cross section data and the models are fit for their use through our calculations of specific reactor physics parameters.

In order to reduce design and, subsequently, licensing uncertainties, while making provision to address the verification and validation of computational tools, it is very important to perform relevant benchmark experiments, in particular for this case of HTGR-type benchmark experiments. The chosen benchmark experiment on which to do the analysis is the ASTRA critical facility [4]. This choice is based on the availability of the experimental data done at this facility ([5] to [11]) as per Eskom and RRC-KI contract. The experiments were done on a PBMR-like core configuration of the ASTRA critical facility as requested by the PBMR Company to investigate reactor physics parameters of the PBMR.

Benchmarking of Monte Carlo methods used to analyse HTR applications against experimental data from a variety of HTR configurations has been done in the past ([12] to [19]), with a variety of focus areas. In 2004, validation of PBMR computational tools using the ASTRA critical facility as a reference was done considering a diffusion code, VSOP [25] as a computational tool and, to a lesser extent, a Monte Carlo code; MCNP-4B. The current project is on benchmarking MCNP5 [26] for HTR applications (more specifically the PBMR), by using the code in the analysis of the ASTRA critical facility reactor physics characteristics.

VSOP [25] is used at PBMR to do comprehensive HTGR reactor physics simulations [27]. VSOP is a deterministic code that makes use of the diffusion approximation and phase-space discretization to numerically solve the neutron diffusion equation. The code can handle most of the level of detail required for the PBMR core design and is quick in executing the calculations, but its disadvantages include:

- The use of the diffusion approximation (inefficient near highly absorbing media).
- System convergence issues (large matrices).
- Discretization errors.
- Input data errors.
- VSOP does not have the capability to model detailed geometry.

The Monte-Carlo N-Particle transport code (MCNP) is one of PBMR's nuclear engineering analysis computational tools that is used to calculate reactor physics parameters as part of investigating plant shielding, economy (e.g. material optimization), and criticality. MCNP is a general Monte Carlo N-particle transport code that can be used to transport various particle types (neutrons, photons and electrons) while treating an arbitrary three-dimensional configuration of the system using point-wise cross-section libraries that represent most of the possible nuclear reactions (particularly for neutrons).

Other particle type reactions can also be represented using different cross-section data sets available in the code distribution package. These advantages for MCNP [26] are the main motivating factors for selecting MCNP as one of the main computational tools at PBMR.

MCNP is extensively used at PBMR to, among other things, determine reactor physics parameters such as the:

- Multiplication factor.
- Control rod worth.
- Particle flux.
- Power profile.
- Energy deposition in the reflector.
- Reaction rates.

Due to this extensive usage, it is critical to address the V&V of the code using a benchmark experiment similar to PBMR, i.e. the ASTRA critical facility as mentioned above. The current ASTRA critical facility benchmark analysis reports on most of the above-mentioned neutronic parameters, with the exception of the energy deposition in the reflector, flux and power distribution. It should be noted that this validation effort focuses on the validation of the MCNP model of the ASTRA critical facility.

.3 PROJECT AIMS

The project aims to:

- Describe a representative ASTRA critical facility MCNP5 model of the experimental set-up.
- Investigate the use of the MCNP code, its cross-section data and calculation models for calculating the ASTRA critical facility benchmark experiment nuclear physics parameters.
- Demonstrate the level of suitability of the considered package (code, cross section and models) versus the experimental results.
- Discuss findings and topics that require further investigation.

THE ASTRA CRITICAL EXPERIMENTS

.1 INTRODUCTION

The ASTRA critical facility was brought into operation in 1980 at the Russian Research Centre ‘Kurchatov Institute’, Moscow, in order to perform neutronic investigations of nuclear safety and critical parameter peculiarities of HTGRs. These investigations are also performed in order to support the validation of computational codes used to model and analyse aspects of similar configurations [28]. In particular, pebble-fuelled reactor configurations were the target market for such investigations. Core configurations that were investigated in the ASTRA critical facility included the VGR-50 (from Russia), PBMR (from South Africa) and GT-MHR (from the USA) [29].

.2 GENERAL FACILITY SPECIFICATIONS

.2.1 Facility overall specification

The ASTRA critical facility experimental set-up is represented by an upright circular cylinder of 380 cm in diameter and 460 cm in height. A cavity is provided in the centre of the reactor in order to build a variety of core configurations that include the use of Fuel, Moderator and Absorber Spheres (FS, MS and AS) in varying ratios of appearance. The cavity was filled with 35 526 to 46 216 spheres (depending on the loading height), based on the actual experimental configurations created in the recent past [4], with varying core heights, and thus varying assembly types. The cavity is made up of three regions: the inner reflector, mixing and core. Table 1 presents important overall specifications of the ASTRA critical facility.

Table 1: Overall ASTRA critical facility specifications (data taken from [8])

No.	Parameter	Value	Unit
1.	Outer Diameter	380	cm
2.	Height (side reflector)	460	cm
3.	Current Core Configuration consideration	Annular (with octahedron end-surfaces)	-
4.	Central Assembly cavity regions	Inner reflector/mixing/ core	-
5.	Inner diameter of Inner Reflector Region	10.5	cm
6.	Outer diameter of Inner Reflector Region	72.5	cm
7.	Outer diameter of Mixing Region	105.5	cm
8.	Equivalent outer diameter of the Core	181	cm
9.	Pebble-bed packing ratio	0.625	-
10.	Loading ratio in the Inner Reflector Region (FS/MS/AS)	0 / 100 / 0	-
11.	Loading ratio in the Mixing Region (FS/MS/AS)	47.5 / 50 / 2.5	-
12.	Loading ratio in the Core Region (FS/MS/AS)	95 / 0 / 5	-
13.	Number of Manual Rods	1	-
14.	Number of Shutdown Rods	8	-
15.	Number of Control Rods	5	-
16.	Number of Experimental Channels	9	-

Figure 1 shows a cross section schematic view of the ASTRA critical facility, whilst Figure 2 shows an axial schematic view of the system.

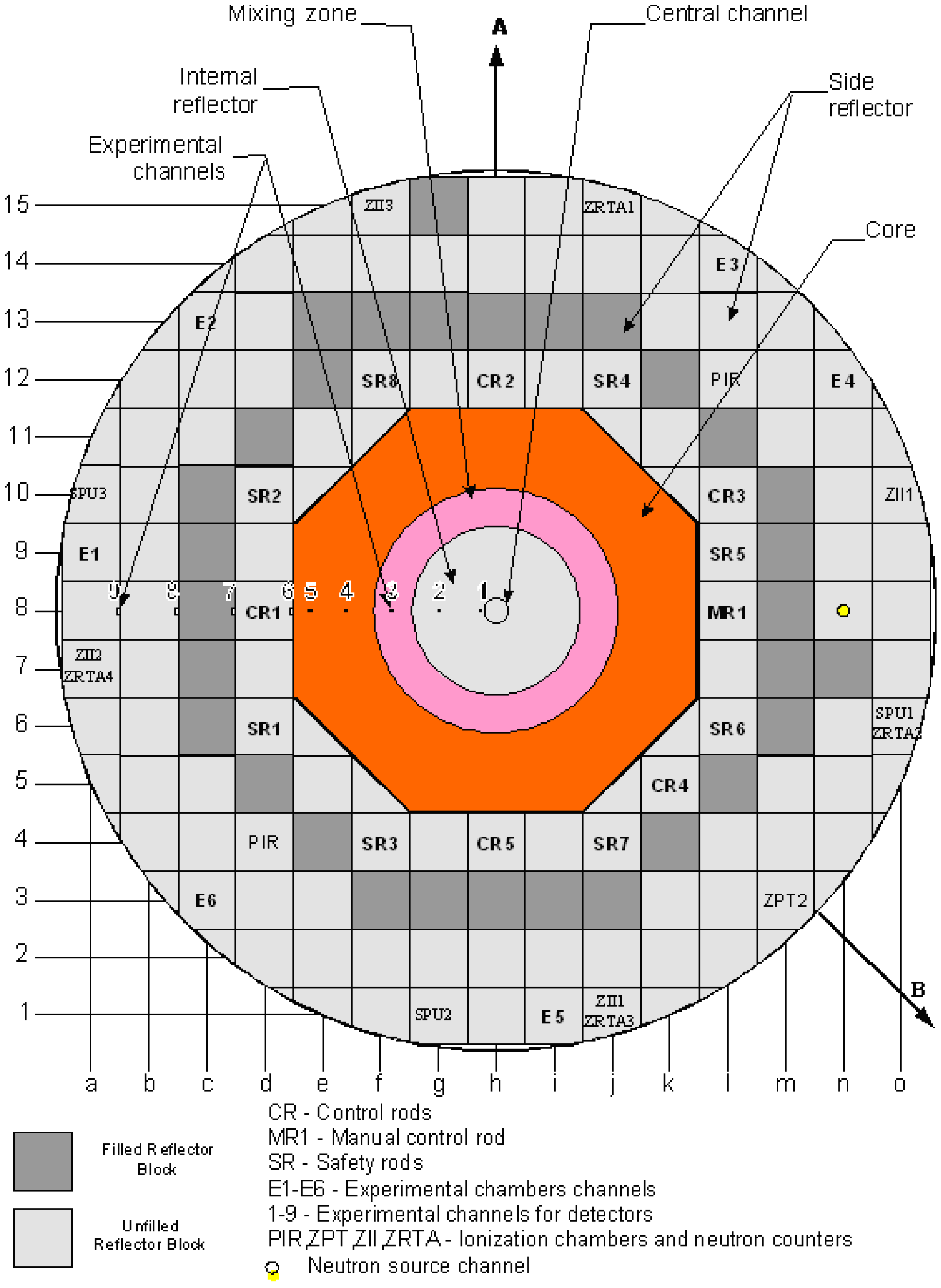

Figure 1: A cross section schematic view of the ASTRA critical facility (figure from [6])

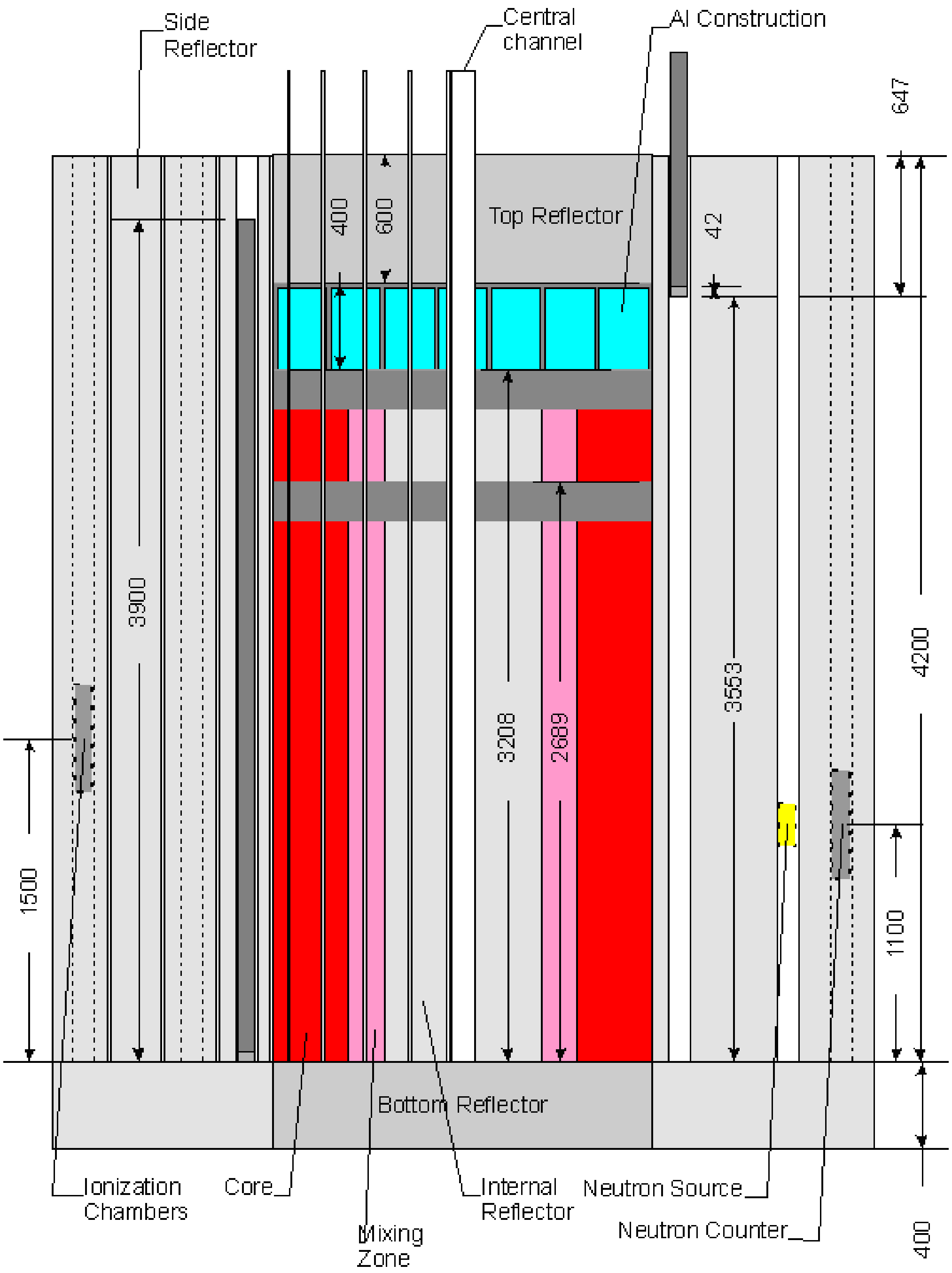

Figure 2: An axial schematic view of the ASTRA critical facility, dimensions in millimetre (figure from [6])

.2.2 Sphere Type and Specifications

There are three types of spheres that were used in the ASTRA critical facility:

- Fuel Spheres.
- Moderator Spheres.
- Absorber Spheres.

More detail on the sphere types is given in the following subsections (.2.2.1 to .2.2.3).

.2.2.1 Fuel Sphere specification

The fuel sphere design is characterized by numerous coated fuel particles embedded in a graphite matrix, with all this encased in an outer graphite shell. Figure 3 presents an illustration of the ASTRA critical facility fuel sphere design.

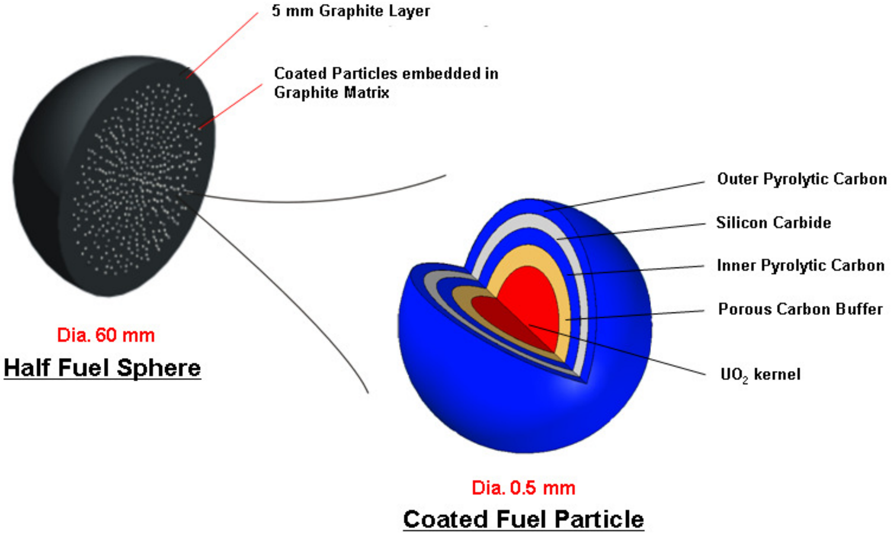

Figure 3: ASTRA critical facility Fuel Sphere design illustration (adopted from [30], data taken from [8])

Table 2 provides an overall account of the fuel sphere specification, while Table 3 gives the coated fuel particle specification.

Table 2: Overall Fuel Sphere specification (data taken from [8])

No.	Parameter	Value	Unit
1.	Enrichment (^{235}U)	21.01	atm. %
2.	Total mass of uranium in each FS	2.44	g
3.	Number of coated particles in each FS	4190	-
4.	Graphite matrix (fuel region) diameter	5	cm
5.	Graphite matrix density	1.85	g/cm^3
6.	Thickness of the graphite shell	0.5	cm
7.	Graphite shell density	1.85	g/cm^3
8.	Graphite impurity content	1.1	ppm

Table 3: Coated Fuel Particle (CFP) specification (data taken from [8])

No.	Region	Outer Radius (cm)	Material/Nuclide	Atm % or Density
1.	UO_2	0.025		10.1 g/cm^3
			U-234	0.20 atm.%
			U-235	21.01 atm.%
			U-236	0.16 atm.%
			U-238	78.63 atm.%
2.	Buffer	0.034	C-Nat	1.1 g/cm^3

No.	Region	Outer Radius (cm)	Material/Nuclide	Atm % or Density
3.	PyC	0.041	C-Nat	1.8 g/cm^3
4.	SiC	0.047	Si-Nat + C-Nat	3.2 g/cm^3
5.	PyC	0.053	C-Nat	1.8 g/cm^3

.2.2.2 Moderator Sphere specification

Each Moderator Sphere is made up of high-purity reactor-grade graphite. The overall specification for this sphere is presented in Table 4.

Table 4: Overall Moderator Sphere specification (data taken from [8])

No.	Region	Outer Radius (cm)	Material/Nuclide	Atm %, Density
1.	Graphite	3	C-Nat	1.68 g/cm^3
			B-Nat[c]	1.1 ppm by wt.

.2.2.3 Absorber Sphere specification

Each Absorber Sphere is characterized by numerous B_4C kernels (active content of the AS) which are embedded in a graphite matrix and the whole set-up is encapsulated in a graphite shell. The overall specification of the Absorber Sphere is presented in Table 5.

Table 5: Overall Absorber Sphere specification (data taken from [8])

	Region	Total Mass of Boron in AS	Outer Radius (cm)	Material/ Nuclide	Atm %, Density
1.	B_4C kernel	0.1 g	0.03	B_4C	2.52 g/cm^3
2.	Graphite matrix		2	C-Nat	1.75 g/cm^3
3.	Graphite shell		3	C-Nat	1.75 g/cm^3
4.	All			B-Nat[c]	1.1 ppm by wt.

.2.3 Side, Bottom and Top Reflector Configuration

The side reflector is characterized by a 380 cm outer diameter and a 460 cm height profile made up of 60 cm high graphite blocks (high-purity reactor-grade graphite). The blocks have a 25 cm x 25 cm square section. An 11.4 cm diameter axial channel (cavity) that can be closed with a plug of reactor-grade graphite, with the same diameter, is provided within the graphite block. Blocks with this channel are referred to as unfilled graphite blocks, whilst those without the hole are called filled graphite blocks. Side reflector specifications for an unfilled graphite block are presented in Table 6 and those for a filled graphite block in Table 7.

---

[c] B-Nat is composed of B-10 with 19.8 atm.% and B-11 with 80.2 atm.%.

Table 6: Side Reflector specifications for an unfilled graphite block (data taken from [8])

No.	Region	Material	Atm %, Density
1.	Side reflector	C-Nat	1.65 g/cm^3
		B-Nat^c	1.1 ppm by wt.

The core, mixing and internal reflector regions are situated on top of a 40 cm thick graphite Bottom Reflector (BR). The bottom reflector is assembled from the 25 cm x 25 cm high purity reactor-grade graphite blocks similar to those used for the filled side reflector. The axial channel in each graphite block was closed using a graphite plug, the same as indicated in the side reflector paragraph above. Table 7 presents the bottom reflector block specification.

Table 7: Bottom Reflector and Side Reflector specifications for a filled graphite block (data taken from [8])

No.	Region	Material	Atm %, Density
1.	Bottom reflector	C-Nat	1.65 g/cm^3
		B-Nat^c	1.3 ppm by wt.

The top of the core, mixing and internal reflector region is provided with a 60 cm thick Top Reflector (TR) made up of high-purity reactor-grade graphite blocks, which is used in some ASTRA critical facility configurations and not in others. The block specification for the bottom reflector is the same as that used for the top reflector block.

.2.4 Control, Safety and Manual Control Rod Specifications

All the reactor control elements (Control Rod (CR), Safety Rod (SR) and Manual Rod (MR) are situated in the axial channels of the Side Reflector. Figure 1 provides the actual positions of the reactor control elements. The design for the CR and SR is the same and is characterized by a cluster of 15 steel tubes arranged in a Pitch Circle Diameter (PCD) of 76 mm. Each tube has an outer diameter of 12.5 mm, and is filled with natural boron carbide with an outer diameter of 10.1 mm. Figure 4 shows the CR and SR configuration. The overall specification for the CR and SR is outlined in Table 8.

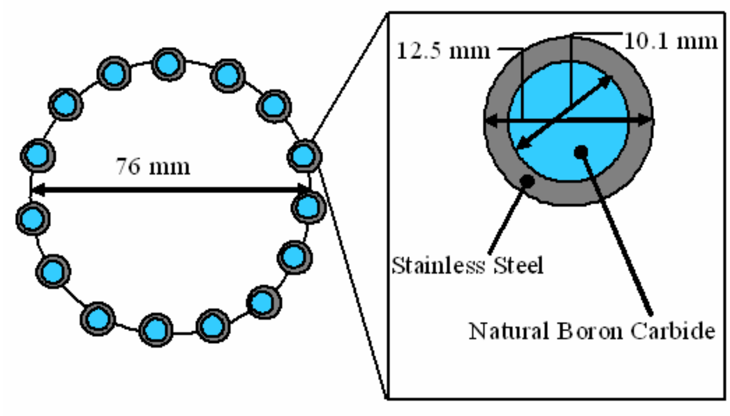

Figure 4: A Control Rod and Safety Rod configuration for the ASTRA critical facility (illustration from [35], data from [8])

Table 8: Overall Control Rod and Safety Rod specification (data taken from [8])

No.	Region	Outer Diameter (mm)	Nuclide/Material	Wt. %, Density
1.	Boron interior	10.1	B_4C[d]	1.53 g/cm^3
2.	Stainless steel shell	12.5	Stainless Steel (Type 12X18H10T)-(composed of ⇩)	7.9 g/cm^3
			Fe	69.1 wt.%
			C	0.12 wt.%
			Si	0.08 wt.%
			Mn	2.0 wt.%
			Cr	18.0 wt.%
			Ni	10.0 wt.%
			Ti	0.7 wt.%

One of the reactor control elements is the Manual Rod (MR). The design for this rod is characterized by a co-axial arrangement of double-walled tubes of aluminium alloy. Figure 5 shows the MR configuration for the ASTRA critical facility. The specification for the MR is outlined in Table 9.

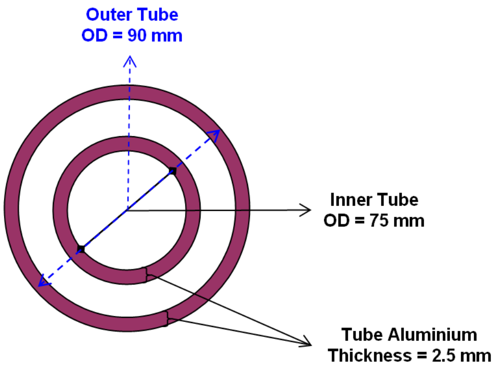

Figure 5: A Manual Rod configuration for the ASTRA critical facility (data taken from [6])

Table 9: Manual Rod material specification (data taken from [6])

No.	Region	Material/Element	Weight %, Density
1.	Aluminium MR shell	Aluminium alloy – AV (GOST 21488-76) – composed of ⇩	2.7 g/cm^3
		Al	95.95
		Cu	0.5 wt.%
		Mg	0.9 wt.%
		Mn	0.35 wt.%
		Zn	0.2 wt.%
		Fe	0.5 wt.%
		Si	1.2 wt.%

---

[d] B-Nat is composed of ^{10}B with 19.55 atm.% and ^{11}B with 80.45 atm.%.

No.	Region	Material/Element	Weight %, Density
		Ti	0.15 wt.%
		Cr	0.25 wt.%

.3 BENCHMARK EXPERIMENTS

In support of the verification of PBMR neutronics computational tools, a number of reactor physics experiments were carried out in the ASTRA critical facility under the Eskom-Kurchatov Institute contract [7]. A number of tasks were necessary in order to facilitate a detailed, accurate, regulated, and traceable process for running the experiments. These are outlined below (refer to [7] for full details about the experimental tasks):

a. Computational analyses of the experiments at the ASTRA critical facility (modelling and results).
b. Laboratory and chemical analyses for the main components of the ASTRA critical facility.
c. k_{eff} study of the configuration, taking into account varying pebble bed height.
d. Control rod worths study, depending on control rod positions on the side reflector and their interference.
e. Control rod differential reactivity study, depending on their depth of insertion in the side reflector.
f. Assembly kinetics measurements.
g. Spatial distribution of reaction rates, neutron fluxes and power in axial and radial direction measurements.
h. Measurement of absolute values of neutron fluxes in different parts of the assembly using composite activation detectors, energy spectra and evaluation of the assembly power.
i. Measurement of reactivity effects of the ASTRA critical facility components and materials essential for the PBMR reactor.
j. Reactivity effects evaluation considering an ingress of hydrogenous media into the pebble bed, and of their influence on the distribution of neutrons and worth of control rods.
k. Investigation of methods used for profiling radial distribution of fuel element power over the core and mixing region.
l. Investigating accidental entry of fuel elements into the PBMR inner reflector region.
m. Measurement of the thermal neutron diffusion length in a prism of the ASTRA critical facility graphite blocks.

The detail for each task is further described in [7]. However, for the purposes of this project other relevant information for some of the listed tasks, specifically c, d, e, and g, is given in the following sections.

.3.1 Criticality parameters considering varying height of the assembly pebble bed (TASK 1)

This section describes the task of performing criticality parameter measurements while considering an increasing pebble bed height. The reactivity effect of the loaded pebbles and the movement of control elements is assessed and reported on.

The pebble bed height was built up after attainment of first criticality. The core was broken down into eight regions, the mixing region into four regions, and the internal reflector region into two regions. The loading was done using 212 spherical elements per small portion loaded. Criticality was attained after every loading of four small portions; this represented one layer of the pebble bed, equal to 848 spherical elements. After this loading, the pebble bed height was measured from the top surface of the bottom reflector to the top boundary of the pebble bed, with an average value reported for each loading region and, finally, for the whole configuration.

The positional movement of Control Rod #5 (CR5) was used to determine and compensate for the reactivity margin during the loading. CR5 was calibrated occasionally while building the pebble bed. Nine layers of the pebble bed were loaded in succession.

.3.2 Control rods worth depending on side reflector position and their interference (TASK 2)

This section provides some information for the control rod worth experiments, taking into account their side reflector position and interference. This is done to quantify both the importance of control rods as their distance from the core boundary increases, and the effect of control rod interference.

One of the distinguishing features of the PBMR is the location of the control elements in the side reflector, which is provided for in the current ASTRA critical facility configuration. The worth of these rods decreases drastically as their distance from the core boundary increases. The rod drop method was used to study the worth of control rods.

Two control rods, CR2 and CR4, were individually moved in direction A and B respectively (directions illustrated in Figure 1). Figure 1 also shows which graphite blocks in the side reflector are plugged (those shown in a darker colour) and which are unplugged (shown in a lighter colour); the latter provide channels for control rod movement. Measurements were carried out using the rod drop method.

.3.3 Control rod differential reactivity depending on side reflector insertion depth (TASK 3)

This section gives some information for the control rod differential reactivity experiments taking their side reflector insertion depth into consideration. These experiments are important for the determination of the reactivity compensation that the control rods provide, and especially for the system nuclear safety (operation, shutdown, etc.).

The rod drop method was used to determine the control rod worth by considering its depth of insertion in the side reflector. Calibration curves were obtained for CR5 and MR1.

.3.4 Spatial distribution of reaction rates in axial and radial directions (TASK 4)

This section provides some information about the spatial distribution of reaction rates experiments, considered in axial and radial directions within the entire reactor. These experiments are measurements of the radial and axial neutron flux profiles.

In order to measure the spatial distribution of neutron fluxes, reaction rates and power in the ASTRA critical assembly; in axial and radial directions, the assembly was provided with in-core aluminium experimental tubes of diameter 1.2 cm and wall thickness 0.1 cm for the placement of activation detectors. The tubes run through the vertical length of the pebble bed, covering the internal reflector, mixing and core regions. The side reflector was provided with rectangular channels of 1.5 cm x 3 cm (vertical grooves), placed on faces of the blocks.

The aluminium tubes were located at the following radial distances (measured from the centre of the internal reflector): 6.75 cm, 24.75 cm, 45.15 cm, 64.85 cm and 80.35, while the side reflector vertical grooves were located at 90.05 cm, 113.2 cm, and 163.2 cm (from the centre of the internal reflector).

The detectors were fabricated as thin foils, rectangular in shape and made up of the following materials:

- Natural dysprosium and indium.
- Uranium in the form of U_3O_8 (enriched to 90% in U^{235}) uniformly distributed in Teflon.

Figure 6 shows a schematic of the assembly longitudinal section for configurations without the TR along ray 8 running through experimental channels NN 1-9, showing uranium detectors and the monitor for the measurement of reaction rates along the assembly radius.

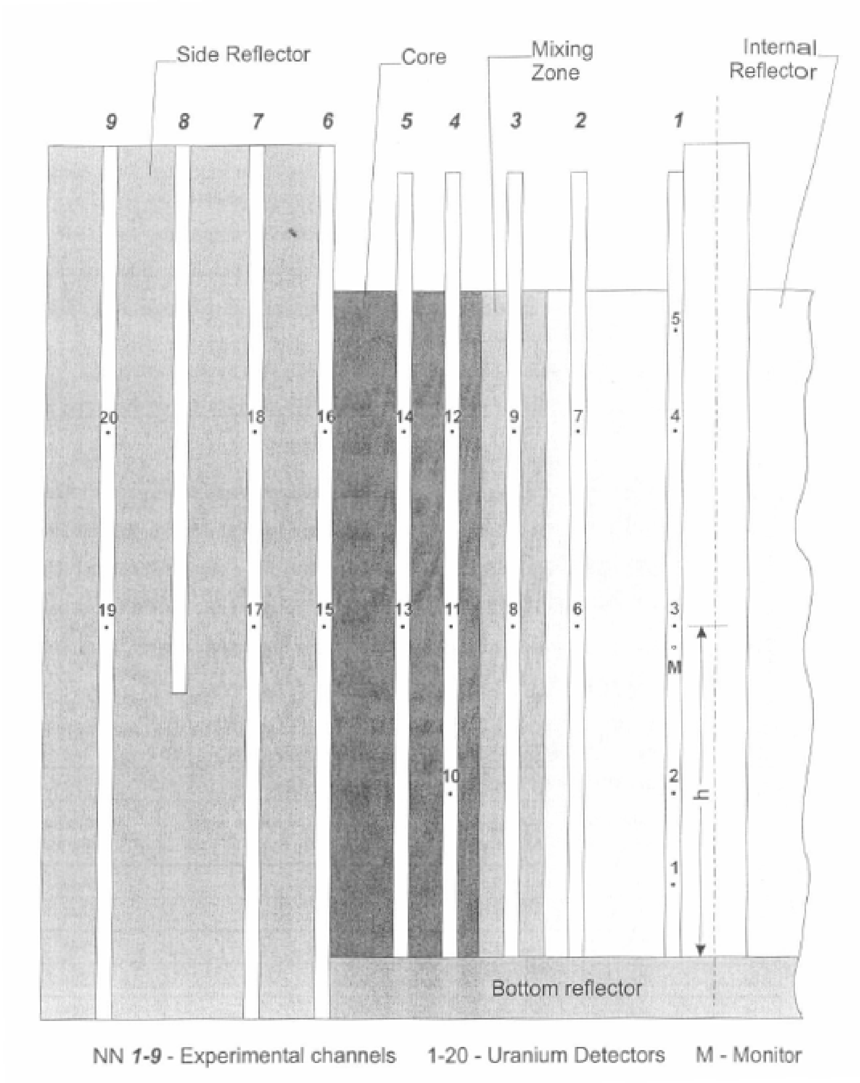

Figure 6: A schematic of the assembly longitudinal section for configurations without the TR (Top Reflector) along ray 8 running through experimental channels NN 1-9, showing uranium detectors and the monitor for the measurement of reaction rates along the assembly radius (figure from [10])

NEUTRON TRANSPORT

Nuclear engineering is an important application field for neutron transport theory; especially noting that since the 1940s this theory has been built into various computational tools, which aid in the design and operation of many nuclear engineering applications. These computational tools are constantly being developed and improved for better and faster execution in performing analysis, while representing the most important nuclear physics characteristics of the problem considered.

Two main solution methods are applied to neutron transport, specifically in the nuclear engineering analysis field; these include the deterministic and Monte Carlo methods. The deterministic method, broadly known as 'neutron transport theory', makes use of discretization for the problem (depending on the method applied, angle, space, energy, etc. can all be discretized). Following on the discretization, a system of algebraic equations can be generated and solved numerically using a few solution strategies, e.g. discrete ordinates, spherical harmonics, finite difference - to mention but a few [31].

The advantages of the deterministic method include:

- System homogenization (resulting in a less complex space discretization - fewer unknowns - faster execution).
- Multigroup treatment (provided that the initial pre-processing of cross sections is done, this results in faster execution in subsequent calculations).
- The solution to the deterministic problem is across the entire system (no need to re-run calculations to obtain specific solutions in certain portions of the geometry).
- Short execution time (which is a result of the above considerations).

The disadvantages associated with the deterministic method include, amongst others:

- Discretization errors (e.g. ray effects, spatial oscillations, etc.).
- System convergence (affected by large matrices with many unknowns to solve).
- Input data errors.

Monte Carlo methods are characterized by events (e.g. particle interaction, die throwing, coin tossing, etc.) which are determined via probabilities or sequences thereof. In the past, the use of this method was justified for complex problems and for benchmarking deterministic methods. However, with the development of more efficient computers (including parallel systems) and improvements in the methodology of executing these calculations, this method has become more attractive.

It should also be noted that it is becoming more common nowadays to use the advantages of deterministic and Monte Carlo codes when creating hybrid simulation methods, and thereby aiming to suppress the weaknesses of each method. This is done in the following way:

- Deterministic methods can provide the Monte Carlo methods with an inexpensive (typically adjoint) calculation to enhance the Monte Carlo method efficiency in its subsequent calculation.
- The opposite is not as common but is still applicable. A Monte Carlo calculation can provide cross sections for the initial deterministic calculation, thereby also improving the deterministic calculation efficiency [32].

This section gives an introduction to neutron transport theory, Monte Carlo methods as applied to neutron transport, and the relevance of this method and its application to the ASTRA critical facility.

.1 TRANSPORT THEORY

Transport theory roots go back more than a century, and are linked to the Boltzmann transport equation (refer to Appendix A, paragraph .1.1), which was initially formulated to address diluted gas kinetic theory. Since the application of the theory in the study of radiation transport in stellar atmospheres (the outer region of the volume of a star), a number of analytical solutions to transport problems were developed as early as the 1930s.

Interest in this theory and solution grew stronger with the introduction of nuclear chain reactors in the 1940s.

The neutron transport equation is used in nuclear reactor analysis to represent the distribution and behaviour of neutrons in the facility considered. Numerical methods are used to model the neutron behaviour, based on a selected method (e.g. deterministic: finite difference, discrete ordinates; Stochastic: Monte Carlo), and thus they are able to be used to calculate specific quantities of neutron behaviour in the system modelled. These may include, but are not limited to, neutron flux, power, reaction rate and system criticality. The general form of this equation can be written as follows [33]:

$$\begin{aligned}&\frac{1}{\upsilon}\frac{\partial\varphi}{\partial t}+\hat{\Omega}\cdot\nabla\varphi+\Sigma_t(\mathbf{r},E)\varphi(\mathbf{r},E,\hat{\Omega},t)\\&=\int_{4\pi}d\hat{\Omega}'\int_0^{\infty}dE\,\Sigma_s(E'\rightarrow E,\hat{\Omega}'\rightarrow\hat{\Omega})\varphi(\mathbf{r},E',\hat{\Omega}',t)+s(\mathbf{r},E,\hat{\Omega},t),\end{aligned}\tag{1}$$

where:

$\mathbf{r}$ is the position vector (i.e. x, y, z)

υ is the neutron speed

$\hat{\Omega}$ characterizes the direction of motion

t is Time

E is Energy

$\varphi(\mathbf{r},E,\hat{\Omega},t)$ is the angular neutron flux

$\Sigma_t(\mathbf{r},E)$ is the macroscopic total cross section

$\Sigma_s(E'\rightarrow E,\hat{\Omega}'\rightarrow\hat{\Omega})$ is the double differential scattering cross section

$s(\mathbf{r},E,\hat{\Omega},t)$ is the source term

The neutron transport equation holds under the following strict assumptions [34] (which are critical for its derivation):

- Particles may be considered as points.
- Particles travel in straight lines between points.
- Particle-particle interactions may be neglected.
- Collisions may be considered instantaneous.
- The material properties are assumed to be isotropic.
- The properties of nuclei and the composition of materials under consideration are assumed to be known and time-independent unless explicitly stated otherwise.
- Only the expected or mean value of the particle density distribution is considered.

.2 MONTE-CARLO METHODS AS APPLIED TO NEUTRON TRANSPORT

This section provides details about the Monte Carlo method as applied to neutron transport. An overview section that links to the components of the method is discussed (presented in Appendix A, paragraph .1.2).

.2.1 Overview

One of the major earlier experiments that helped to define the Monte Carlo method is the estimate of π (Buffon (1777) and Laplace (1886)). Earlier in its development, this method was regarded as a method of last resort and as very expensive (in terms of time and money), with deterministic methods dominating reactor computational analysis, mainly because of its cumbersome application. However, as discussed above, the improvements in computer systems and methodology application have made this method just as attractive in the field of reactor analysis.

The first major use of the Monte Carlo technique was during World War II for the Manhattan Project by J von Neumann, S Ulam and E Fermi. Today it is used in a variety of fields; including economics, aerospace engineering, electrical engineering, and mathematics, to mention just a few.

The Monte Carlo methods are unlike the deterministic method in that no set of differential equations is required to start the analysis; all the physics of the problem is simulated by sampling Probability Density Functions (PDFs). Random sampling from the PDFs can proceed when the PDFs are known. Repeated simulations (called ‘histories’) are then done and the desired result is taken as an average over the number of observations. This method is accompanied by a statistical error estimate of the average result, and since this is linked to a certain number of Monte Carlo histories, it is possible to determine how many histories are needed to reach a particular error.

In order to go forward with the discussion of the Monte Carlo method, one needs to be aware of the following primary components of the Monte Carlo method:

a. Random variable.
b. Random number.
c. Random number generator.
d. Probability Distribution Functions (PDFs).
e. Cumulative Distribution Functions (CDFs).
f. Fundamental Formulation of Monte Carlo (FFMC).
g. Sampling procedure.
h. Scoring (or tallying).
i. Statistics.
j. Variance reduction techniques.
k. Parallelization and vectorization.

Brief descriptions of each of the above primary components of the Monte Carlo method are provided in Appendix A, paragraph .1.2. It is important to note that since the focus of the project is on the modelling and calculating experiments related to the ASTRA critical facility benchmark, the theoretical basis is discussed satisfactorily for the purposes of completing the analysis.

CALCULATIONAL/SIMULATION TOOLS

.1 INTRODUCTION

The importance of computational tools used to perform numerical analysis, taking into account nuclear physics characteristics of nuclear installations, in the nuclear engineering field is demonstrated in the worldwide deployment of nuclear reactors [2] amongst other nuclear installations. Computational tools form part of the design process of nuclear reactors and their contribution is used to understand certain fundamental characteristics (control, radiation levels, etc.) of the overall systems, which helps in the definition of a safety basis for the considered system.

A number of nuclear engineering computational analyses may be required to arrive at an optimum and safe design, depending on an installation size, its composition, potential usage plan, cost (material optimization), and decommissioning considerations. As was discussed in the previous chapter, neutron transport numerical solutions are classified by two methods - particularly in the nuclear engineering field - the deterministic and Monte Carlo methods.

This project makes use of one of the prominent Monte Carlo computational tools, MCNP, which is particularly attractive for PBMR simulation since some of the advantages of this code are that it can handle detailed geometry modelling, continuous energy physics representation, the capability to handle a variety of particles, a variety of source-term representations, the application of population control methods (variance reduction) for efficient particle transport through the problem geometry.

Monte Carlo computational tools (such as MCNP, MONK, TRIPOLI and MORET amongst others) have been used to model HTR-type configurations ([12] to [24]) for more than a decade, and particularly in the case of PBMR, MCNP has been used quite extensively in the analysis of radiation transport, criticality and shielding problems.

The bulk of this HTR-type configuration simulation knowledge, represented in articles [12] to [19], focuses on modelling room temperature experiments, taking into consideration the full representation of the coated fuel particles, spheres and overall experimental structure. A more detailed account of the modelling of HTRs using Monte Carlo methods is discussed in the next chapter.

The following section provides a description of the MCNP code used for this project.

.2 MCNP

MCNP is a general-purpose Monte Carlo N-particle Transport code that can be used to transport various particle types while treating an arbitrary three-dimensional configuration of the system, considering point-wise continuous energy cross-section libraries that represent all the possible nuclear reactions in the energy range from 10^{-11} to 20 MeV. The code is based on the Monte Carlo methodology that simulates events tracking, with all the physics contained in probability density functions. Specified results are made available through the use of tallies (these are recordings of some aspects of particle average behaviour), which must be requested prior to the execution of the calculation.

MCNP is one of the most widely utilized computational tools at PBMR for the calculation of some core parameters, deep penetration and shielding problems. Due to this extensive usage, it is very important to address the issue of verification and validation for this code for HTR applications, which are similar to the PBMR application.

MCNP, version 5, release 1.40, and with ENDF/B VI release 8 cross-section data [26], was used for this project.

MCNP MODEL OF THE ASTRA CRITICAL FACILITY

.1 INTRODUCTION

In order to build a representative MCNP model of the ASTRA critical facility, all the facility detail that is presented in section .2 is used. The considered MCNP model of the ASTRA critical facility covers all the details within the top, bottom and side reflectors. This includes:

- The reactor central cavity which contains the core, mixing and reflector regions, which are assembled using spheres.
- The reactivity control elements, which are located in the side reflector channels.
- The experimental tubes and channels, which are located in the core and side reflector blocks, respectively.

The model was built as precisely to the experimental configuration as possible, with inherent MCNP geometrical modelling inadequacies introduced in the process. These will be discussed in the subsequent sections (subsections .2.1.1, .2.3, and .2.4).

The model description and assumptions are discussed in the ensuing sections (section .2 and .3).

.2 MODEL DESCRIPTION

.2.1 Reactor Central Cavity

The reactor central cavity of the ASTRA critical facility is made up of spherical elements (fuel, absorber and graphite spheres) and experimental tubes. The following sections explicitly address each reactor central cavity model item.

.2.1.1 Spherical Elements

The ASTRA critical facility central cavity has three types of spherical elements:

- fuel sphere.
- absorber sphere.
- graphite sphere.

This section provides some modelling background for a fuel sphere; which is extended to the modelling of the other sphere types considered in this ASTRA critical facility configuration.

In considering any pebble-fuelled HTGR, one needs to be mindful of the existence of double heterogeneity in two modelling levels, and as such properly represent this in the simulation model. The first level of heterogeneity is represented by the random distribution of coated fuel particles (in a FS) and boron carbide kernels (in an AS) in a graphite matrix. The second level of heterogeneity is represented by randomly distributed pebbles (FS, AS and MS) loaded in the reactor central cavity in varying loading ratios.

Up until recently it was common practice to model double heterogeneity within pebble-fuelled HTGR configurations through the use of a common MCNP feature called the regular lattice distribution. The regular lattice approach is made available within MCNP in order to treat problems that require the repeated structures capability (whether this is an array of storage tanks or in the current case, kernels in a graphite matrix or pebbles in the reactor cavity), but it should be noted that in applying the method any randomness is ignored.

In order to represent the randomness of kernels in each fuel and absorber sphere, MCNP makes use of its new stochastic capability, implemented through the use of a URAN card [23]. This capability works on the principle that whenever a neutron enters a lattice element containing an embedded universe that is flagged as stochastic (as would be stipulated in the URAN card), the universe coordinates are transformed randomly to a new position within the unit lattice and the kernel is moved to that position. This capability was not used in this work; but the plan is to include it as part of future work.

The current MCNP model was built using the regular lattice option. It is clear that this approach does not represent the stochastic nature of the problem, for both the coated fuel particles and the fuel spheres. However, various investigations ([14], and [19] to [24]) have been performed to account for the resultant bias due to the use of regular lattices.

Some of the findings from these investigations indicate that, in general, the effect of using a cubic lattice when modelling coated fuel particles instead of an exact stochastic representation is relatively small: 0.2% Δk in reactivity. This is considering a fixed 5x5x5 lattice of fuel kernels, resulting in a 30% packing fraction (PF), whilst for the current configuration only 4% PF is encountered. Other findings indicate that, for the consideration of TRISO particle coating layers homogenized into the graphite matrix, there is no significant difference in the k_{eff} results between two repeated structure models considered (triangular and square) [17], a difference of no more than 0.06% Δk in reactivity is reported. The same study reports that a computational saving of 30% can be realized by using this homogenization approach.

Findings from [22] highlight subtle effects depending on the way in which pebbles in a container are modelled, indicating that this effect could prove important depending on the pebble-fuelled HTGR system considered. However, within the PBMR design, a 1 m^3 box containing PBMR fuel was modelled in both random distribution (pebble positions explicitly represented) and Hexagonal Closed Packed (HCP) lattice and it was demonstrated that no significant differences in k_{eff} results are identified. This outcome is supported by limiting packing fraction fluctuations in the system and ascertaining that the loaded heavy mass is kept below 1% of its target values. Therefore, it is concluded that the HCP lattice can be used to model the PBMR equilibrium core in a reasonable and accurate way to simulate random distribution of spheres in the core [21].

The work performed as part of the same report [21] also highlights that there is no significant difference in k_{eff} results between various regular lattice configurations (Body Centred Cubic (BCC), HCP, and Face Centred Cubic (FCC)).

Given all the findings discussed above and the specifications for the fuel sphere presented in Table 10, the ASTRA critical facility model only makes use of the regular lattice considerations at both coated fuel particle and sphere level, and thus represents the fuel in the following way:

- A unit cell containing a UO_2 kernel and surrounding graphite matrix are organized in a cubic array that fills the whole inner region of each fuel sphere. Due to the need to respect the uranium mass load of 2.44 g in each sphere, a pitch = 0.25 cm was chosen. Figure 7 depicts a representation of how the kernels are arranged in a fuel sphere.
- A volume homogenization approach for the four coating layers into the graphite matrix is adopted as discussed above and introduced in [17].
- The fuel sphere graphite shell is modelled explicitly.

Table 10: ASTRA critical facility FS MCNP model inputs

No.	Parameter	Value	Unit
1.	UO_2 kernel radius	0.025	cm
2.	TRISO coated particle outer radius	0.053	cm
3.	Fuel region radius (matrix)	2.5	cm
4.	Fuel Sphere outer radius	3	cm
5.	UO_2 density	10.1	g/cm^3
6.	Uranium load per Fuel Sphere	2.44	g
7.	U^{235} Enrichment	21.01	wt%
8.	Number of coated particles/Fuel Sphere	4189	-
9.	Lattice side (cubic lattice for kernels)	0.2500	cm

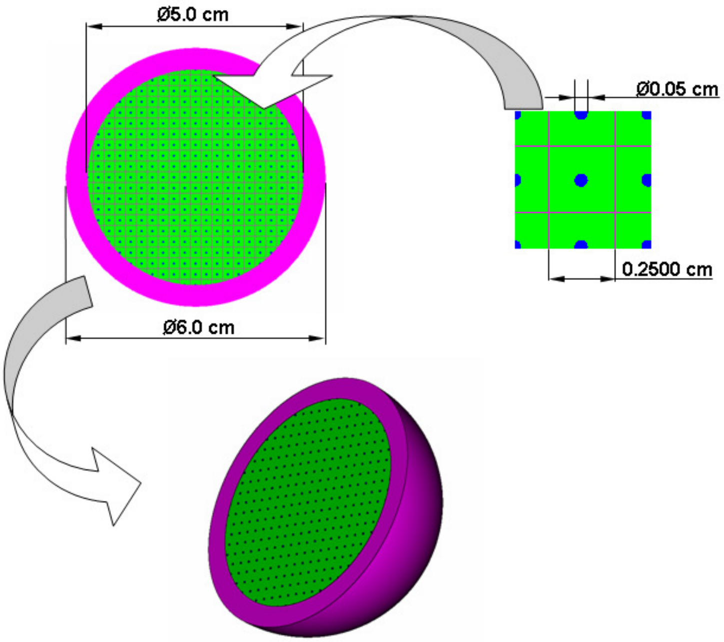

Figure 7: An MCNP Model for the ASTRA critical facility FS, showing dimensions for the kernel, Inner Fuel Matrix Region and FS as well as a Regular Lattice distribution of kernels in the graphite matrix

The methodology adopted during the modelling of each Fuel Sphere, as explained and illustrated above, is also applied in the ASTRA critical facility MCNP modelling of the Absorber Sphere, with all the specifications for the Absorber Sphere presented in Table 11. No illustrations of the Absorber Sphere resultant figures are presented, as they are similar to the Fuel Sphere MCNP representations in Figure 7.

Table 11: ASTRA critical facility AS MCNP model inputs

No.	Parameter	Value	Unit
1.	B_4C kernel radius	0.003	cm
2.	Absorber region radius (matrix)	2	cm
3.	Absorber Sphere outer radius	3	cm
4.	B_4C kernel density	2.52	g/cm^3
5.	Boron load per Absorber Sphere	0.1	g
6.	Number of B_4C kernels/Absorber Sphere	4.482×10^5	-
7.	Lattice side (cubic lattice for kernels)	0.0421	cm

To complete the inventory of the spheres used to build the assembly, we now consider the moderator sphere. This sphere type was modelled as a normal sphere filled with high-purity reactor-grade graphite, with specifications outlined in Table 12.

Table 12: ASTRA critical facility MS MCNP model inputs

No.	Parameter	Value	Unit
1.	Moderator Sphere outer radius	3	cm
2.	Moderator density	1.68	g/cm^3
3.	Equivalent boron impurity	1.1	ppm by weight

The modelling of spheres in the reactor cavity, as discussed at the beginning of this section, was done using a BCC regular lattice distribution. This choice is supported by the analysis performed to investigate the effect of using different regular packing arrangements in a 1 m^3 box filled with fuel spheres, where it was shown that there was no significant difference in k_{eff} results between various regular lattice configurations (BCC, HCP and FCC) [21].

The reactor cavity was radially divided into three regions where specific types of spheres were arranged in each; this included the Inner Reflector (IRR), mixing (MR) and core zones (CR). The choice of regular lattice packing (BCC) distribution for spheres was made based on a few characteristics to be represented in the model. These included respecting all the loading ratios and masses of spheres in different regions, the total number of spheres needed to build the configuration, and respecting the packing fraction of the overall pebble bed, which was 0.625.

The internal reflector region is 31 cm thick (radially) and is made up of only graphite spheres. The mixing region is 16.5 cm thick and is made up of absorber, fuel, and moderator spheres in a loading ratio of 2.5:47.5:50. The core region is 37.75 cm thick and is made up of fuel and absorber spheres in a loading ratio of 95:5. Taking into account the thickness of each region, the required packing fraction of 0.625 and the loading ratios described above, a common BCC unit lattice was chosen and implemented in all the regions. This unit lattice is made up of 40 spheres situated in a 7.12635 cm pitch. An illustration of this unit lattice dimensions and various sphere loading scenarios in each loading region is shown in Figure 8.

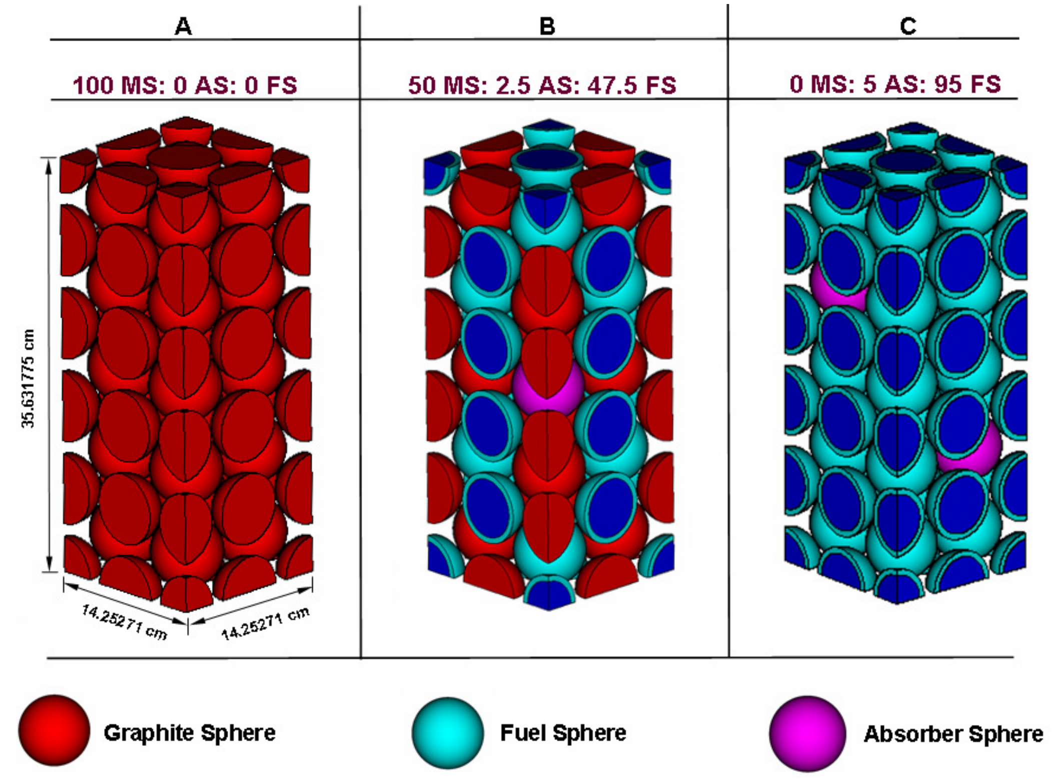

Figure 8: An MCNP Body-Centred-Cubic lattice illustration showing lattice dimensions and loading scenarios in each loading region; A - Inner Reflector, B - Mixing, and C - Core. The illustration also indicates each pebble type by colour identification and labelling.

The pebble height for this considered experimental configuration of the ASTRA critical facility is 268.9 cm ±1.5 cm; therefore, in order to fill up this total height, approximately eight unit cells as described in Figure 8 are modelled. This is an important consideration when employing the repeated structures methodology in filling the core, as it is generally understood that the lower the number of repetitive unit lattices used, the more difficult it is to respect the different sphere loading ratios in each region. The consequence of using repeated structures in MCNP modelling of the pebble-type fuel is the cutting of the spheres on the problem geometry boundaries.

Figure 9 gives an illustration of the ASTRA critical facility MCNP modelling; showing the loading of pebbles in the core, whilst Figure 10 gives an illustration of the MCNP model, showing sphere cutting.

Dimensions in cm

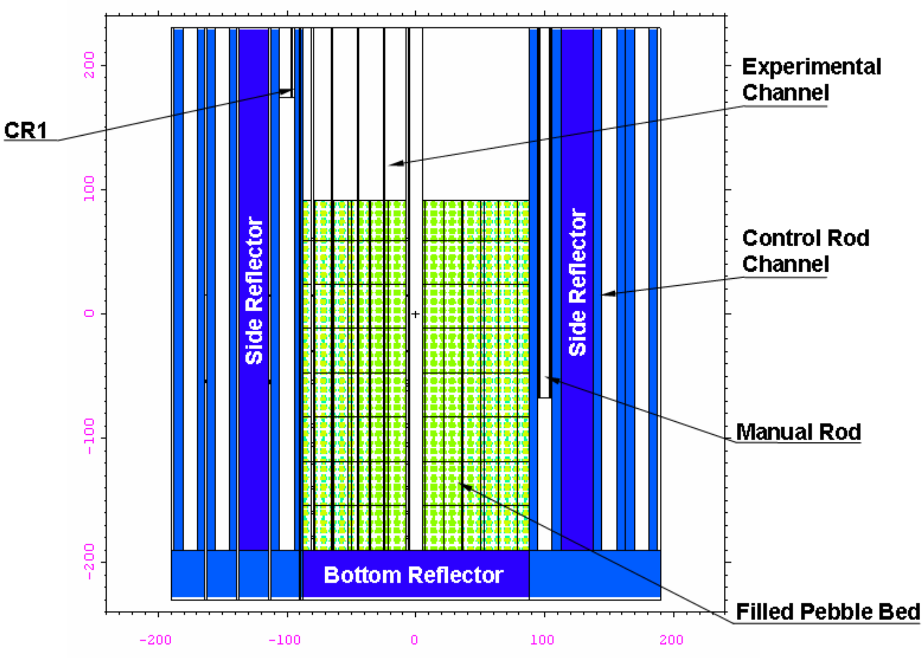

X-Z cut at Y = 0 cm, Plot origin at (0, 0, 190)

Figure 9: ASTRA critical facility MCNP model, showing an X-Z section example of spheres loaded in the reactor central cavity

Dimensions in cm

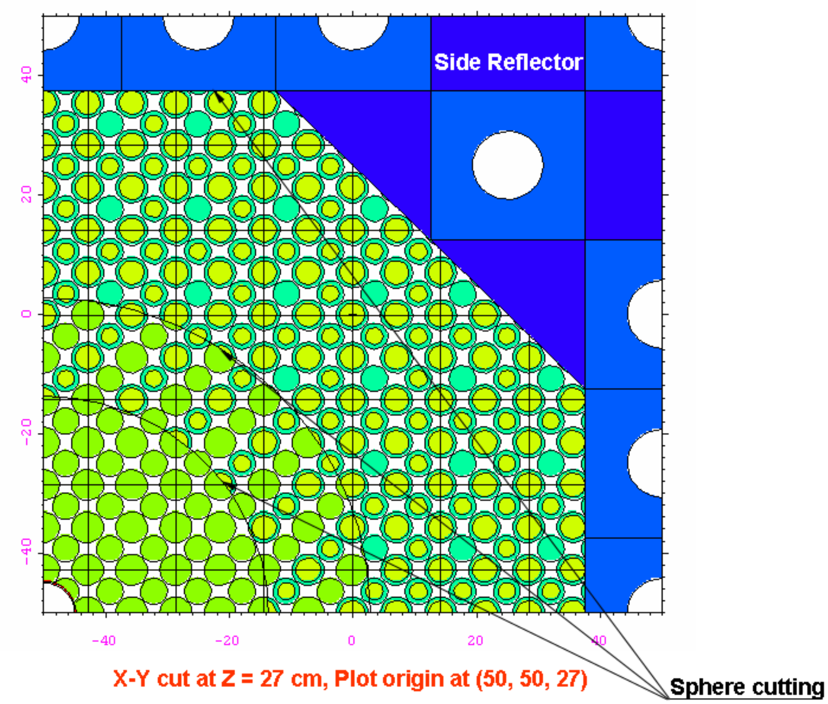

X-Y cut at Z = 27 cm, Plot origin at (50, 50, 27)

Figure 10: ASTRA critical facility MCNP model, showing; an X-Y section example of sphere cutting

A volumetric analysis was performed using the current model as a way of checking some of its characteristics, including whether or not the packing ratio is properly respected throughout the model and whether the number of spheres loaded into the assembly is also properly respected. The results of this study are presented in Appendix C. No significant deviations were observed in this analysis (a difference to reference value of -1.7% was reported in the total number of loaded spheres modelled versus those reported in the experimental set-up 38 584), which supported the model approach confidence in light of not considering the stochastic nature of the problem. However, no final conclusions can be made until this is explicitly addressed and planned for future work. The next step in the validation effort is the use of the MCNP model of the ASTRA facility to calculate reactor physics parameters for a variety of benchmark configurations. This is done for Configuration No. 1 [6] and is presented in the following sections of this document.

.2.2 Side and Bottom Reflectors

Side and bottom graphite reflectors as detailed in section .2.3 were modelled in MCNP. The side reflector was built using 25 cm x 25 cm square blocks that are modelled to run the full length of the side reflector. The side reflector is made up of two types of the side reflector blocks:

- an unfilled; and
- a filled side reflector block.

The unfilled configuration of the block has an 11.4 cm diameter axial channel, used in subsequent calculations as a control rod movement channel.

The two side reflector block types also differ in their reactor grade graphite impurity content, with the unfilled block containing 1.1 ppm by weight of natural boron whilst the filled block contains 1.3 ppm. The bottom reflector was modelled as a single disc-type graphite block which has the same graphite material as that used for the filled side reflector block. Figure 11 illustrates the MCNP model of the side reflector configuration, with colours and channels depicting the different graphite block materials.

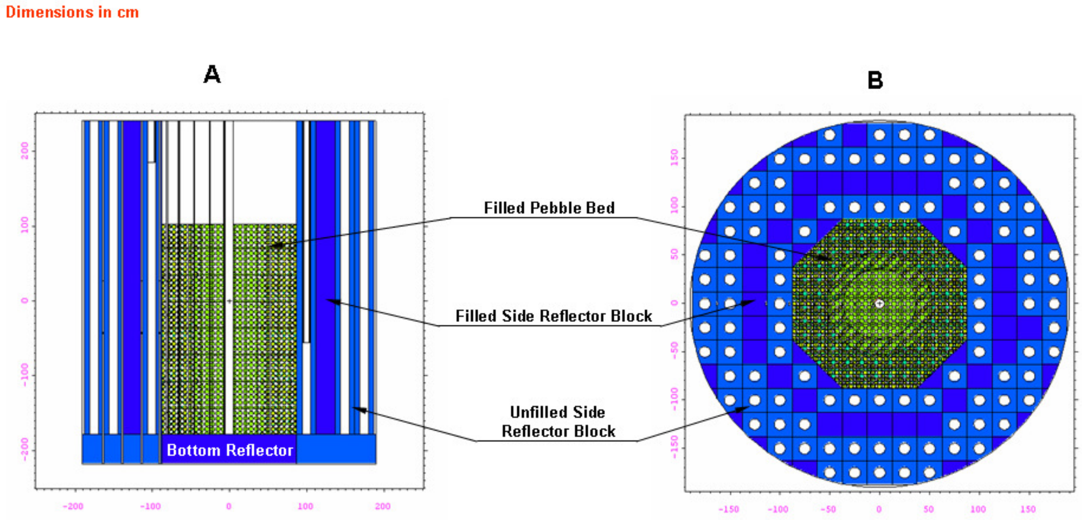

X-Z cut at Y = 0 cm,
Plot origin at (0, 0, 195)

X-Y cut at Z = 27 cm, Plot
origin at (0, 0, 27)

Figure 11: An X-Z (A) and X-Y (B) sections of the ASTRA critical facility MCNP model showing bottom and side reflectors; two side reflector configurations are identified with a channel

.2.3 Control Elements

Control elements as detailed in section .2.4 were modelled in MCNP. Two configurations of control elements were modelled. One covered both the Control and Safety Rods (CR and SR, respectively) while the other covered the Manual Rod (MR). The model configurations of the CR and SR are the same: a cluster of 15 tubes arranged in a PCD of 76 mm. Each tube is modelled with an outer stainless steel shell which is filled with natural boron carbide. The Manual Rod (MR) is modelled as a co-axial arrangement of double-walled tubes of aluminium alloy. Figure 12 shows the control elements arrangement in the ASTRA critical facility assembly and their detailed arrangement.

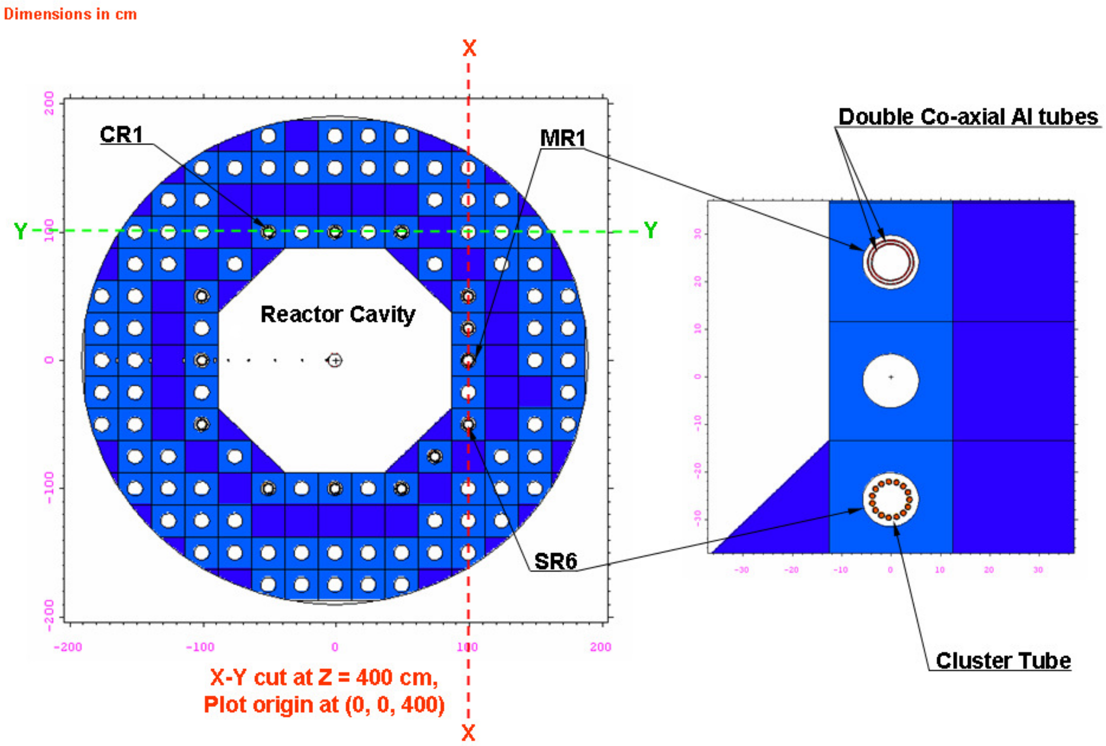

Figure 12: An X-Y section of the ASTRA critical facility MCNP model showing the Control, Safety and Manual Rods; the section plots are made at Z = 400 cm

The control element full insertion and extraction positions along the side reflector are listed in Table 13. Note that all the numbers are given relative to the top of the Bottom Reflector.

Table 13: Control, Safety and Manual Rods extraction and insertion depth limits along the side reflector of the ASTRA critical facility MCNP model relative to the top of the Bottom Reflector (data taken from [6])

Control Element	h_{out}, cm	h_{in}, cm
CR1#	364	7.7
CR2#	361	2.6
CR3#	355	4.7
CR4#	367	2.8
CR5#	354	10.7
MR1#	356	11.8
SR#**	362	6.3

** These positions refer to all Safety Rods (on average).

Figure 1 shows all the control element positions in the side reflector.

It should be noted that for the base experiment considered (Configuration No. 1 [6]), with a pebble bed height of 268.9 cm and considering both the reactivity control requirements and the location of the control elements in the side reflector, the control, safety and manual rods have specific heights (normal positions) of insertion into the side reflector. Due to reactivity effects that need to be investigated as part of the benchmark, the normal positions will be modified to reflect the test objective (e.g. reactivity effect as a function of control rod insertion depth, position away from the core, etc.). However, it must be clear that the control elements normal positions for the Configuration No. 1 assembly are those represented by the extraction positions outlined in Table 13, except for the MR1 position, which is inserted up to 122.8 cm (measured above the top surface of the bottom reflector).

As an illustration of the control elements' final insertion heights in the side reflector channels for Configuration No. 1, Figure 13 shows representative plots.

Dimensions in cm

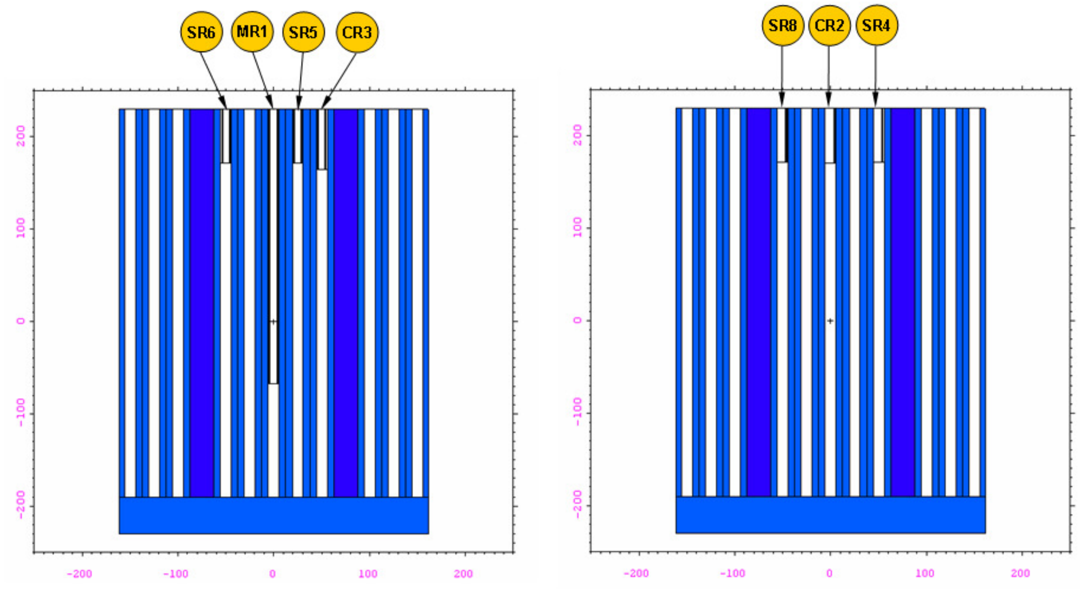

Y-Z cut at X = 100 cm, Plot origin at (100, 0, 190)

X-X cut from Figure 12

X-Z cut at Y = 100 cm, Plot origin at (0, 100, 190)

Y-Y cut from Figure 12

Figure 13: Y-Z and X-Z sections of the ASTRA critical facility MCNP model, Configuration No. 1, illustrating some of the insertion depths of control elements in the side reflector. MR1 inserted to 122.8 cm, other rods on out position presented in Table 13.

.2.4 Experimental Channels and Detectors

Experimental channels and detectors used for measuring spatial distribution of radiation as detailed in section .3.4 were modelled with MCNP. Figure 14 is a general location illustration for the experimental channels as well as for the detectors modelled.

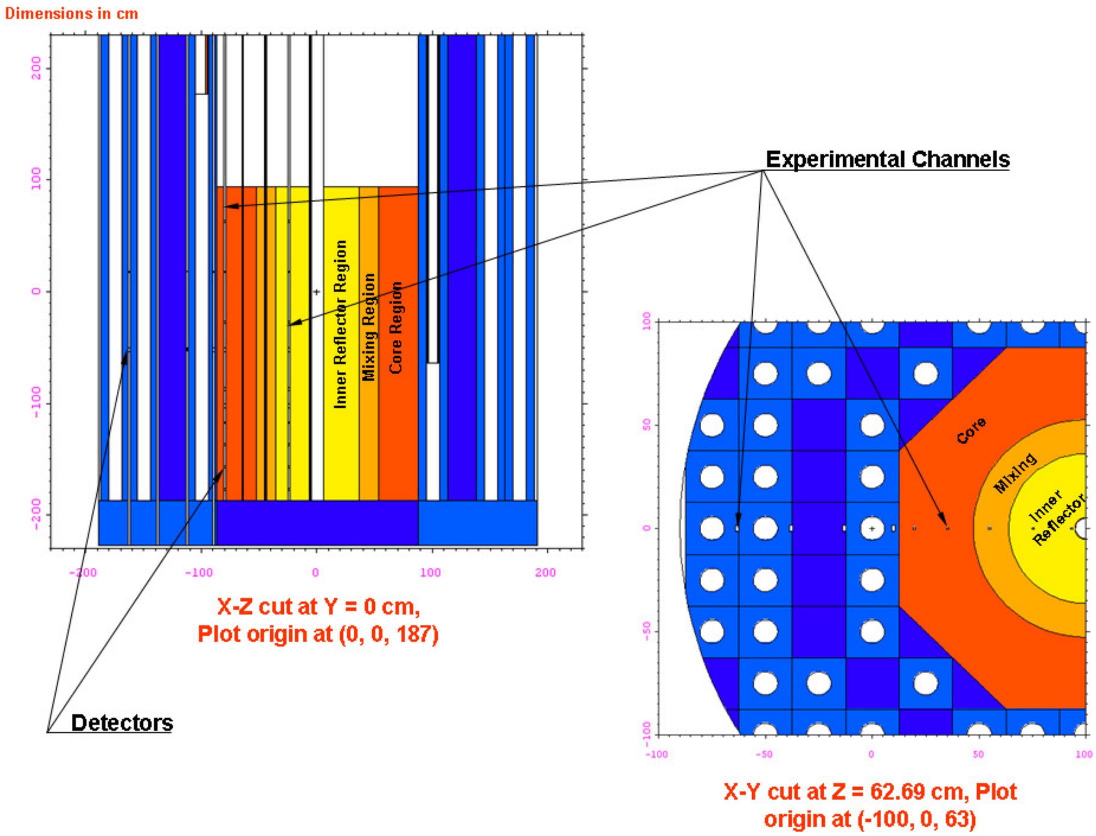

Figure 14: X-Z and X-Y sections of the ASTRA critical facility MCNP model showing the location of experimental channels and detectors

In terms of the detectors used to measure the spatial distribution of reaction rates, two considerations were made when modelling these:

- Detector size.
- Multiple reaction rate considerations.

Considering the detector size, the detectors detailed in section .3.4 are very small and thus present a difficult task in terms of collecting statistics for meaningful average results.

A few test calculations were done using different-sized detectors, after which it was decided to model the original small-sized detectors with increased size. The final dimensions for the final selection of detector sizes (those used at the centre and tail) are presented in Figure 15 for the reactor cavity detectors, and rectangular cubes with dimensions: for the 'centre Detector': *l* = 3 cm, *w* = 1 cm, *h* =1 cm, and for the 'Tail Detector': *l* = 1.4 cm, *w* = 1 cm, *h* = 1 cm for the side reflector detectors.

Following the selection of larger detectors, the detectors were further selected to represent the gradient profile of the experimentally measured reaction rates. A steep gradient is observed at the tail (ends) measurements of the channel while a more flat profile can be observed at the centre position. The idea is that one needs to use a smaller F4 (path-length estimator) tally (detector) at the ends in order to accurately represent the steep slope of the profile, while a larger F4 tally is used in the middle. All of this is to ensure that the size is just large enough to provide adequate results.

Considering the multiple reaction rates to be calculated, a 'Tally Multiplier' methodology within MCNP was used. This approach is applied in such a way that only the empty detector volumes (refer to Figure 15 as an example) are represented in the geometry and the calculated reaction rates are represented in the F4 tally calculation part of the MCNP input file through the use of the 'Tally Multiplier' that works (using relevant cross sections and material specification – refer to Table 14 to Table 16) on the calculated flux in the detectors.

Table 14: Uranium-235 reaction rates detector specification

	Side Reflector		**Reactor Cavity**	
	Tail	**Centre**	**Tail**	**Centre**
Parameter				
Length (cm)	1.4	3	1.4	3
Breadth (cm)	1	1		
Width (cm)	1	1		
Radius (cm)			0.5	0.5
Mass (mg)	7.5	7.5	7.5	7.5
Atom Density [atom.(b. cm)$^{-1}$]	1.35x10^{-5}	6.41x10^{-6}	1.75x10^{-5}	8.16x10^{-6}
MCNP ID [26]	92235.30y (Dosimetry data library)			

Table 15: Indium $^{(a)}$ reaction rates detector specification

	Side Reflector		**Reactor Cavity**	
	Tail	**Centre**	**Tail**	**Centre**
Parameter				
Length (cm)	1.4	3	1.4	3
Breadth (cm)	1	1		
Width (cm)	1	1		
Radius (cm)			0.5	0.5
Mass (mg)	30	30	30	30
Atom Density [atom.(b. cm)$^{-1}$]	1.12x10^{-4}	5.24x10^{-5}	1.43x10^{-4}	6.68x10^{-5}
MCNP ID [26]	49113.30y (Dosimetry data library) 49115.30y (Dosimetry data library)			

$^{(a)}$ – as part of MCNP5 material specification, this material is further broken down into the In-113 and In-115 isotopes.

Table 16: Dysprosium reaction rates detector specification

	Side Reflector		**Reactor Cavity**	
	Tail	**Centre**	**Tail**	**Centre**
Parameter				
Length (cm)	1.4	3	1.4	3
Breadth (cm)	1	1		
Width (cm)	1	1		
Radius (cm)			0.5	0.5
Mass (mg)	60	60	60	60
Atom Density [atom.(b. cm)$^{-1}$]	1.59x10^{-4}	7.42x10^{-5}	2.02 x10^{-4}	9.45x10^{-5}
MCNP ID [26]	66164.26y (Dosimetry data library)			

One of the MCNP options of tallying spatial reaction rates is the use of point detectors. This option was not used in the current study because there was enough confidence in the calculation of reaction rates using the F4 tally along with a tally multiplier option.

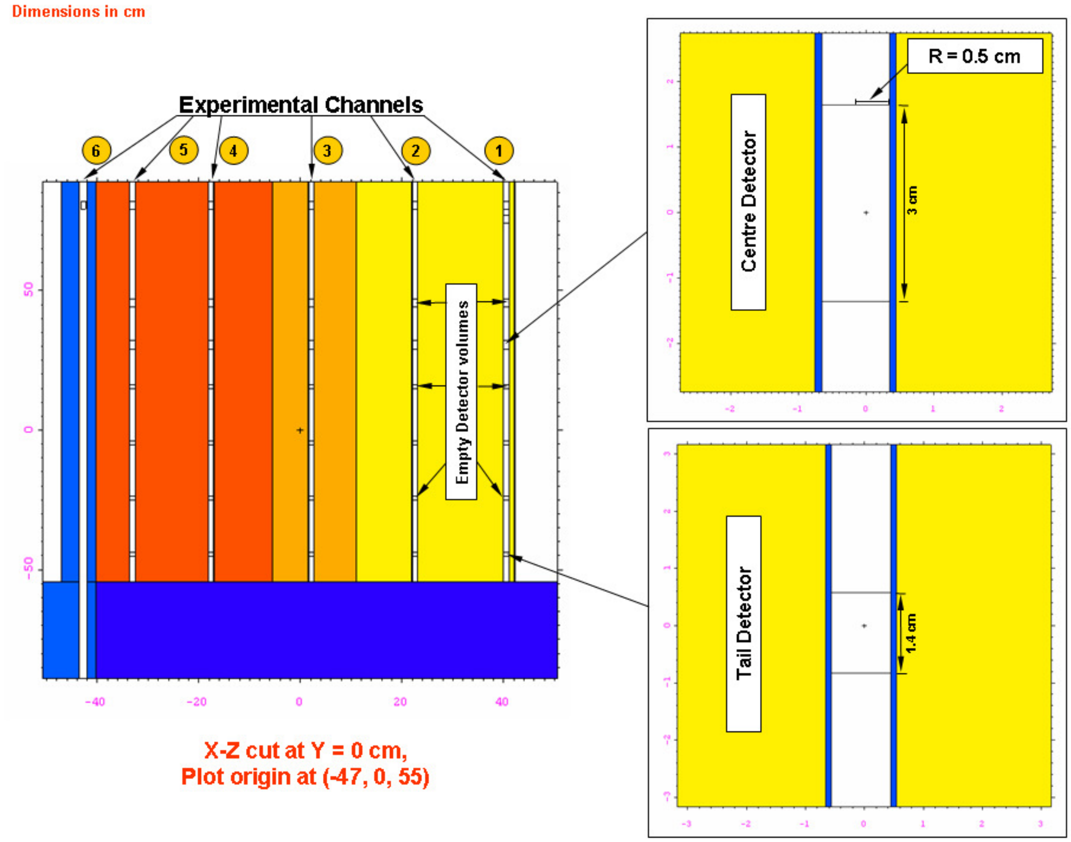

Figure 15: X-Z sections of the ASTRA critical facility MCNP model showing the modelled detector specifications

.2.5 Materials

Table 17 to Table 28 list all the relevant materials used in the model development, along with their references and general specifications used during the incorporation of such materials into the MCNP model of the ASTRA critical facility.

Table 17: FS UO_2 kernel material specification as modelled in MCNP (data taken from [8])

Region	Material	Nuclide	Atom Density [atom./(b. cm)]	MCNP ID [26]
Fuel kernel	UO_2	U-234	4.515 x10^{-05}	92234.69c
		U-235	4.743 x10^{-03}	92235.69c
		U-236	3.612 x10^{-05}	92236.69c
		U-238	1.775 x10^{-02}	92238.69c
		O-16	4.515 x10^{-02}	8016.62c

Table 18: FS volume homogenized coating layers and graphite matrix material specification as modelled in MCNP (data taken from [8])

Region	Material	Nuclide	Atom Density [atom./(b. cm)]	MCNP ID [26]
Graphite matrix [FS]	Graphite, Boron and Silicon Carbide	C-Nat.	9.1661 x10^{-02}	6000.66c
		Si-Nat.	4.5087 x10^{-04}	14000.60c
		B-10	2.3266 x10^{-08}	5010.66c
		B-11	8.5711 x10^{-08}	5011.66c

Table 19: AS B_4C kernel material specification as modelled in MCNP (data taken from [8])

Region	Material	Nuclide	Atom Density [atom./(b. cm)]	MCNP ID [26]
Absorber kernel	B_4C	C-Nat.	2.74467 x10^{-02}	6000.66c
		B-10	2.17378 x10^{-02}	5010.66c
		B-11	8.8049 x10^{-02}	5011.66c

Table 20: FS graphite shell material specification as modelled in MCNP (data taken from [8])

Region	Material	Density [g/cm^3]	Nuclide	Atom fraction	MCNP ID [26]
Shell [FS]	Graphite	1.85	C-Nat.	9.999989 x10^{-01}	6000.66c
			B-10	2.178 x10^{-07}	5010.66c
			B-11	8.822 x10^{-07}	5011.66c

Table 21: AS graphite shell and matrix material specification as modelled in MCNP (data taken from [8])

Region	Material	Density [g/cm^3]	Nuclide	Atom fraction	MCNP ID [26]
Shell & matrix [AS]	Graphite	1.75	C-Nat.	9.999989 x10^{-01}	6000.66c
			B-10	2.178 x10^{-07}	5010.66c
			B-11	8.822 x10^{-07}	5011.66c

Table 22: MS material specification as modelled in MCNP (data taken from [8])

Region	Material	Density [g/cm^3]	Nuclide	Atom fraction	MCNP ID [26]
Moderator Sphere [MS]	Graphite	1.68	C-Nat.	9.999989 x10^{-01}	6000.66c
			B-10	2.178 x10^{-07}	5010.66c
			B-11	8.822 x10^{-07}	5011.66c

Table 23: BR and SR – filled block material specification as modelled in MCNP (data taken from [8])

Region	Material	Density [g/cm^3]	Nuclide	Atom fraction	MCNP ID [26]
Side (filled) & Bottom reflector	Graphite	1.65	C-Nat.	9.999987 x10^{-01}	6000.66c
			B-10	2.574 x10^{-07}	5010.66c
			B-11	1.0426 x10^{-06}	5011.66c

Table 24: SR – unfilled block material specification as modelled in MCNP (data taken from [8])

Region	Material	Density [g/cm^3]	Nuclide	Atom Fraction	MCNP ID [26]
Side reflector (unfilled)	Graphite	1.65	C-Nat.	9.999989 x10^{-01}	6000.66c
			B-10	2.178 x10^{-07}	5010.66c
			B-11	8.822 x10^{-07}	5011.66c

Table 25: CR and SR B_4C inner tube material specification as modelled in MCNP (data taken from [8])

Region	Material	Nuclide	Atom Density [atom./(b. cm)]	MCNP ID [26]
CR & SR Inner Tube	B_4C	C-Nat.	1.6664 x10^{-02}	6000.66c
		B-10	1.3031 x10^{-02}	5010.66c
		B-11	5.3625 x10^{-02}	5011.66c

Table 26: CR and SR Stainless Steel (Russian ID: 12X18H10T) outer tube material specification as modelled in MCNP (data taken from [8])

Region	Material	Nuclide	Atom density [atom./(b. cm)]	MCNP ID [26]
CR & SR Outer Tube	Stainless Steel	Fe-54	3.45 x10^{-03}	26054.62c
		Fe-56	5.46 x10^{-02}	26056.62c
		Fe-57	1.25 x10^{-03}	26057.62c
		Fe-58	1.78 x10^{-04}	26058.62c
		C-Nat.	1.03 x10^{-04}	6000.66c
		Si-28	6.35 x10^{-05}	14028.62c
		Si-29	3.21 x10^{-06}	14029.62c
		Si-30	2.13 x10^{-06}	14030.62c
		Mn-55	1.72 x10^{-03}	25055.62c
		Cr-50	6.74 x10^{-04}	24050.62c
		Cr-52	1.30 x10^{-02}	24052.62c
		Cr-53	1.47 x10^{-03}	24053.62c
		Cr-54	3.66 x10^{-04}	24054.62c
		Ni-58	5.87 x10^{-03}	28058.62c
		Ni-60	2.25 x10^{-03}	28060.62c

Region	Material	Nuclide	Atom density [atom./(b. cm)]	MCNP ID [26]
		Ni-61	9.72 x10^{-05}	28061.62c
		Ni-62	3.09 x10^{-04}	28062.62c
		Ni-64	7.83 x10^{-05}	28064.62c
		Ti-Nat.	6.02 x10^{-04}	22000.62c

Table 27: MR Aluminium (Russian ID: GOST 21488-76 – AV (1340)) tube material specification as modelled in MCNP (data taken from [6])

Region	Material	Nuclide	Atom density [atom./(b. cm)]	MCNP ID [26]
MR Tube	Aluminium	Fe-54	1.71 x10^{-05}	26054.62c
		Fe-56	2.71 x10^{-04}	26056.62c
		Fe-57	6.19 x10^{-06}	26057.62c
		Fe-58	8.85 x10^{-07}	26058.62c
		Cu-Nat.	2.95 x10^{-04}	29000.50c
		Si-28	6.53 x10^{-04}	14028.62c
		Si-29	3.31 x10^{-05}	14029.62c
		Si-30	2.19 x10^{-05}	14030.62c
		Mn-55	2.06 x10^{-04}	25055.62c
		Cr-50	6.41 x10^{-06}	24050.62c
		Cr-52	1.24 x10^{-04}	24052.62c
		Cr-53	1.40 x10^{-05}	24053.62c
		Cr-54	3.48 x10^{-06}	24054.62c
		Mg-12	5.31 x10^{-04}	12000.62c
		Ti-Nat.	8.85 x10^{-05}	22000.62c
		Zn-Nat.	1.18 x10^{-04}	30000.42c
		Al-27	5.66 x10^{-02}	13027.62c

Table 28: Experimental Channels Aluminium tube material specification as modelled in MCNP (data taken from [8])

Region	Material	Nuclide	Atom density [atom./(b. cm)]	MCNP ID [26]
Experimental Channel Tube	Aluminium	Fe-54	1.73 $\times10^{-05}$	26054.62c
		Fe-56	2.74 $\times10^{-04}$	26056.62c
		Fe-57	6.26 $\times10^{-06}$	26057.62c
		Fe-58	8.95 $\times10^{-07}$	26058.62c
		Cu-Nat.	5.96 $\times10^{-05}$	29000.50c
		Si-28	2.75 $\times10^{-04}$	14028.62c
		Si-29	1.39 $\times10^{-05}$	14029.62c
		Si-30	9.24 $\times10^{-06}$	14030.62c
		Mn-55	5.96 $\times10^{-05}$	25055.62c
		Mg-12	5.96 $\times10^{-05}$	12000.62c
		Ti-Nat.	8.95 $\times10^{-05}$	22000.62c
		Zn-Nat.	5.96 $\times10^{-05}$	30000.42c
		Al-27	5.87 $\times10^{-02}$	13027.62c

.3 MODEL ASSUMPTIONS

The assumptions made in the development of the ASTRA critical facility MCNP model (as described in section .2) are listed below:

a. The four layers that are part of the coated fuel particle have been modelled as part of the fuel sphere graphite matrix. This volume homogenization is assumed to not bias the model, with this concept discussed and substantiated as part of the introductory paragraphs to section .2.1.1.

b. A regular lattice distribution of fuel kernels, absorber kernels and different sphere types (FS, AS and MS) loaded in the reactor cavity was assumed. This approach is also discussed and substantiated as part of the introductory paragraphs to section .2.1.1.

c. A BCC lattice distribution of the spheres in the core is assumed over a few other possible distributions. This is discussed once more and substantiated in the introductory paragraphs to section .2.1.1.

d. All the modelled detectors to be used for the spatial distribution of reaction rates calculations were assumed at larger volumes. This is due mainly to the need to increase the statistical counting in their volumes with the view of obtaining better average results. This concept is also discussed in section .2.4.

e. The detectors are also assumed as empty inner volumes and only tally multipliers are considered in order to account for the needed reaction rates.

f. Void instead of air is assumed to fill all the empty volumes of the ASTRA critical facility MCNP model.

CALCULATION PROCEDURE

.1 INTRODUCTION

The ASTRA critical facility benchmark experiments considered, which are represented under Configuration No. 1, provide a representative experimental set-up of the PBMR design. Results for three basic reactor physics parameters are obtained:

- System criticality – Tasks 1 and 3b.
- Control rod worth – Tasks 2 and 3a.
- Reaction rate – Task 4.

This section focuses on giving an introduction to the above-mentioned reactor physics parameters and the calculation procedure followed in quantifying them using MCNP. Further detail on the above parameters will be given, as required.

.2 SYSTEM CRITICALITY

Nuclear criticality or, in short, ‘criticality’, is the ability to sustain a fission chain reaction by fission neutrons from one generation to another. The ratio between the number of neutrons in a specific generation and the number of neutrons in the previous generation is quantitatively represented by the multiplication factor k_{eff}. If this factor has a value of less than one, the system is subcritical (the fission reaction is not self-sustaining), whilst a value that is greater than one represents a supercritical system (neutron population in one generation is more than that in the previous).

The calculation of k_{eff} consists of the estimation of the mean number of fission neutrons produced in each generation per started fission neutron. A generation is regarded as a neutron life from birth in fission to death by leakage or absorption. MCNP regards the computational equivalent of a fission generation as a k_{eff} cycle (a cycle is a computed estimate of an actual fission generation) [26].

In order to begin a criticality calculation in MCNP (taking into account that a model with geometrical and material specifications has already been done, refer to Chapter 0), there is a need to describe information about a KCODE card (used by MCNP to do nuclear criticality calculations).

A typical KCODE card contains the following information:

- Nominal source size for each cycle.
- Initial guess for k_{eff}. In all the benchmark task calculations this is 1.
- Number of cycles to skip before beginning tally accumulation (in case initial source guess is poor). After these cycles are discarded, it is assumed that the fission source distribution has converged to its stationary state (the fundamental mode) and tallies for reaction rates and a k_{eff} value may be accumulated.
- Number of cycles to be done before the problem ends.

In MCNP, this card works in conjunction with a specified initial spatial source distribution of fission points, which in this work was defined using an SDEF card that employs a rejection procedure. The rejection procedure is based on generating a fixed amount of potential fission points over a large volume and subsequently accepting those points that belong to fissile materials and rejecting all others. This is only done for the first k_{eff} cycle.

The Task 1 reactor physics parameter, the system's multiplication factor (also referred to as the criticality eigenvalue) is quantified as explained in the paragraphs above. This k_{eff} is used to calculate core reactivity as discussed below:

The core reactivity is given by a mathematical expression shown below. It represents the fraction of neutrons created that are in excess or deficiency to those required to keep the neutron population constant. This quantity is normally represented using the symbol ρ, which is computed using the following equation [33]:

$$\rho = \frac{k_{eff} - 1}{k_{eff}} \tag{2}$$

where:

k_{eff} is the multiplication factor which characterizes the system.

The reactivity is zero for a critical reactor, positive for a supercritical reactor and negative for a sub-critical reactor. The calculational procedure for quantifying the Task 3b reactor physics parameter (dependence of k_{eff} with varying pebble bed height) involves the substitution of the calculated k_{eff} into Equation (2). Since this parameter is reported in dollars [$] in the experimental documentation, then the calculated ρ for a given pebble bed height is also reported in the same units by using the delayed neutron fraction for ^{235}U, $\beta_{\mathbf{eff}} = 0.0072$ [9].

.3 CONTROL ROD WORTH

Control rod worth is computed by considering a change in reactivity between two plant states; e.g. by considering a reference plant state and an altered one by rod movement. The difference in reactivity between both plant states results in the 'control rod worth' between those states.

.4 REACTION RATES

The spatial distribution of reaction rates measured in the ASTRA critical facility provides a good indication of the radial and axial neutron flux profiles throughout the assembly configuration making up the Task 4 experiments - refer to section .3.4.

A reaction rate gives an indication of how many reactions of a particular type (e.g. fission or absorption) occur per unit time and volume in a given position of the assembly configuration. In accounting for each reaction rate of a particular type, MCNP makes use of an FMn card, which is used to calculate quantities of the form [26]:

$$C\int \varphi(E) R_m(E) dE \tag{3}$$

Where $\varphi\ (E)$ is the energy-dependent fluence (particles/cm^2) and $R_m\ (E)$ is an energy-dependent response function taken from the MCNP cross-section library or specifically designated quantities. The constant C is an arbitrary scalar quantity that can be used for normalization. The subscript m refers to a material identifier.

In the considered case, the units for the above variables are as follows:

- C = Atomic density [atom/b/cm].
- $\varphi(E)$ = fluence [neutrons/cm^2].
- R_m = Microscopic reaction cross section [b].

The response function operator (in this case representing the reaction cross section) has a variety of reaction types. In this analysis, only the fission and absorption reaction microscopic cross section are considered. This covers what is required in terms of the experiments performed for Configuration No. 1, in terms of the uranium, indium and dysprosium detectors considered in section .3.4. Knowledge of the atom density factor, C, was not needed in our analysis since all the experimental results were reported as a fraction of their respective normalization detector values. More information about normalization detectors is given in the Task 4 results section (.6).

RESULTS AND DISCUSSION OF THE ASTRA BENCHMARK

.1 INTRODUCTION

In the following sections, reactor physics parameter calculational results are presented as a function of the configuration update. The basic MCNP model represents Configuration No. 1, which as explained before has a $H_{PB} = 268.9$ cm and all the control elements are in out positions except for MR1, which is inserted to 122.8 cm (measured from the top of the bottom reflector). Updates to the basic MCNP model include configurations that represent different locations and insertion depths of control rods and spatial reaction rate distribution as discussed in detail in section .3.

.2 TASK 1 - CORE CRITICAL HEIGHT

The first ASTRA critical facility benchmark calculations to be done were the determination of the pebble bed height at which the modelled configuration achieves criticality (k_{eff} = 1). Experimentally this height was determined to be 268.9 cm [6]. The considered configuration for the Task 1 calculation is characterized by the control elements in out positions, as presented in Table 13, except for MR1, which is located 122.8 cm from the top surface of the bottom reflector. This represents Configuration No. 1.

A number of MCNP5 criticality calculations at various pebble heights (including the experimentally measured height of 268.9 cm) were done for this benchmark task. The associated standard deviation for these k_{eff} calculations was less than 0.00009 in all cases. The criticality calculation at the experimental height results in a k_{eff} value of 1.01136 (standard deviation is 0.00003), representing a 1 123 pcm overestimation in reactivity. The critical pebble bed height as calculated using MCNP5 was determined to be 255 cm.

A number of other results from different benchmark participants who have also performed this Task 1 analysis and reported their results are available mainly in [28] and the VSOP result in [35]. Note that [28] is a draft International Atomic Energy Agency (IAEA) Tecdoc which is currently undergoing independent review. The version used is available on the CD accompanying this thesis. Participants' results are included in this work only for purposes of comparison.

Table 29 lists the calculated pebble bed height for the ASTRA critical facility Configuration No. 1, as determined by each benchmark participant. The code used is also indicated.

Table 29: Critical pebble bed height of the ASTRA critical facility as measured and predicted by various computational methods from benchmark participants, all control elements in out positions, except MR1 which is at 122.8 cm insertion

Benchmark Participant	**Code Used**[a]	**Critical Height (cm)**	**(C-E)/E [%]**
Experiment [RUS]	n/a	268.9±1.5 [9]	n/a
South Africa [SA]	<u>This Work</u>[b]	<u>255</u>	<u>-5.2</u>
	VSOP94	*	-
China	MCNP4A	253.6[#]	-5.7
Indonesia [INDO]	WIMSD4	259[#]	-3.7
Turkey [TUR]	MCNP4B[c]	270.5/255.1[#+]	+0.6/-5.1
France [FRA]	TRIPOLI4.3	[**]	-
United Kingdom [UK]	WIMS9	263.4[#]	-2.1

[a] The codes used for comparison purposes are described in various sections of this report; i.e. TRIPOLI in section .1 and VSOP94 in section .2, except for the WIMS code, which is a general lattice cell and burn-up program.

[b] Refers to this report’s MCNP5 result. Note that in subsequent tables and figures, the same underlined words will be used.

[c] MCNP4B results presented within the whole document are all calculated for a model with a packing fraction of 0.61 (not the experimental 0.625) [28].

* Only one VSOP94 k_{eff} value is reported in [35], that is $k_{eff} = 1.0053$.

\# Results extracted from document [28].

\+ Results shown for cases in which side reflector channels were all unplugged and plugged, respectively.

** The Tripoli4.3 pebble bed critical height was not reported in [28], however, criticality estimation at the experimental height of 268.9 cm is reported as 1.01185, with a standard deviation of approximately 0.00070.

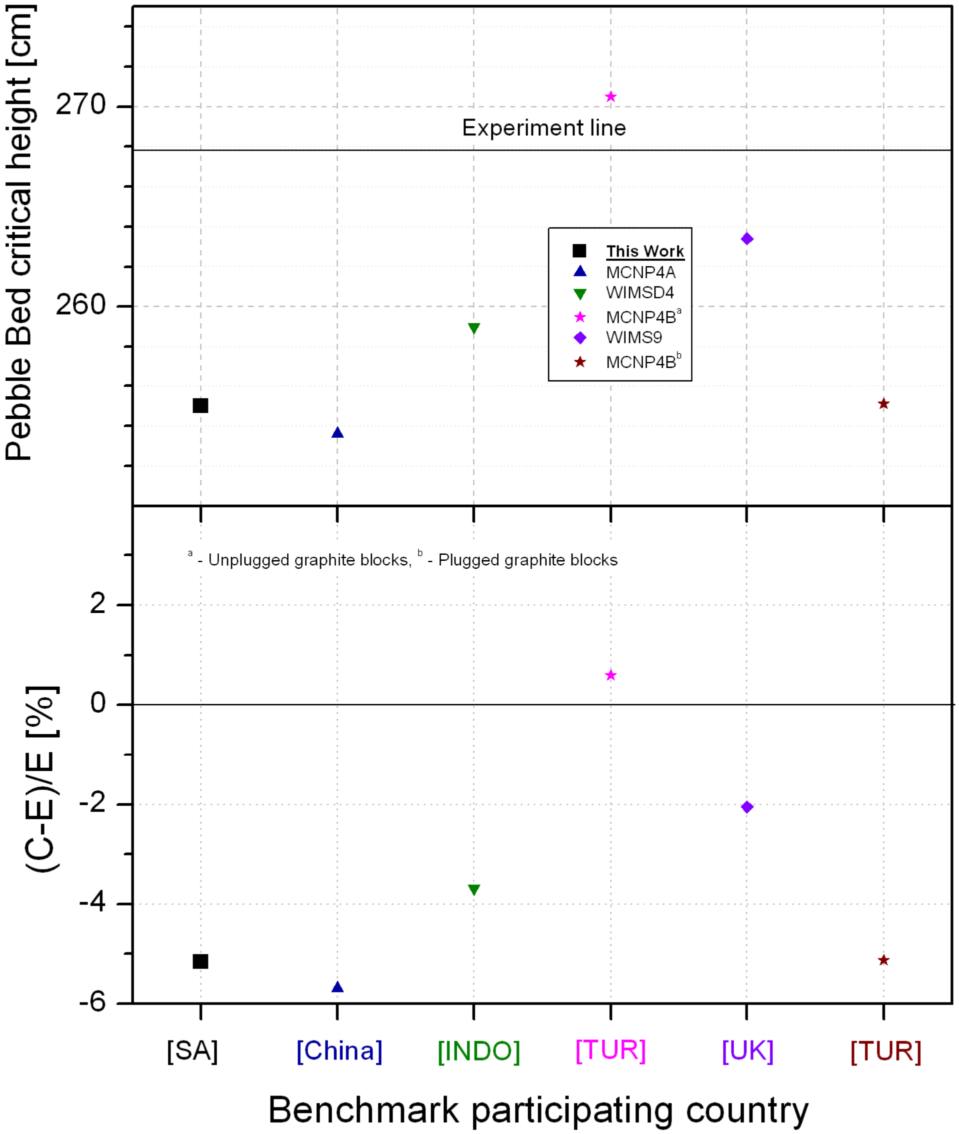

Figure 16: ASTRA critical facility (Configuration No. 1) calculated pebble bed critical height as a function of considered computational tools and benchmark participating country. The calculated (C-E)/E values are also presented

The MCNP5 calculated pebble bed critical height is far from the experimental value - about 5% below the experimental critical height. This represents an underestimation of the pebble bed height by about 14 cm (this is equivalent to 1 954 spheres).

In order to gain more insight on why our model reports a higher k_{eff} than the experimental value for the critical height of 268.9 cm, a stochastic volume calculation was done. This is a ray tracing MCNP volume calculation of kernels, coating layers, graphite matrix, FS, AS, MS, total volume occupied by the spheres in different regions and gaps between them, amongst others. The results of this study indicate an overall sphere underestimation of 1.7% (this is equivalent to 37 940 spheres modelled instead of the experimental 38 584 value) while the underestimation of fuel and moderator spheres is each less than 2% and that of the absorber spheres is almost 4% (refer to Appendix C). This could be one of the reasons why our MCNP5 model reports an overestimation in reactivity.

There is clear evidence of measurements of pebble bed height and total number of loaded spheres for the assembly in the experimental documentation, along with a reported average porosity value of 0.375 (packing fraction 0.625). However, a simple calculation using the total number of spheres in the core (38 584) and the measured critical height of 268.9 cm indicate that only a packing fraction of 0.635 is possible for the reported experimental assembly specifications (refer to section .2). The French effort (Tripoli4.3 code) declares the same for this issue [28]. An MCNP5 model calculation taking into account this packing fraction was done with a resultant k_{eff} of 1.02026. The stochastic volume calculation for this model shows an improvement (the total sphere underestimation is 0.1%, fuel and moderator sphere underestimation is less than 0.3%, and absorber sphere underestimation is 1.6%).

The calculated k_{eff} value for the current MCNP5 model with a packing fraction of 0.625 and a pebble bed height of 268.9 cm is 1.01136. The French effort, with a similar assembly and modelling approach, reports a similar overestimation of the k_{eff} value (1.01185) [28].

One of the studies done by the French in order to understand their overestimation of the k_{eff} value was that of testing various sphere arrangements in the mixing and core regions. The most significant effect from such an investigation came from a study of absorber sphere arrangement in the core region. Normally, with this Tripoli4.3 model, absorber spheres are modelled to reside within the inner core region boundary. However, in this study two further cases were investigated. This included the movement of the absorber spheres to the centre and outer boundary of the core region. The difference in reactivity between the normal (inner boundary) absorber sphere location in the core region and the outer boundary results in 1 419 pcm [28]. This is something we were not able to test with our MCNP5 model due to time constraints. However, with some effort this already indicates an area for investigation in future.

In spite of the overestimation of the experimental reactivity, MCNP5 and Tripoli4.3 model results are in close agreement for similar model representation and approach, both with (C-E)/E values in the 5-6% range.

A strong effort to represent the experiment as accurately as possible was made in this task and in the analysis. However, the following geometrical modelling, cross section and lack of experimental information aspects could not be satisfactorily investigated:

- The ability of the geometrical modelling and lack of experimental information to respect the overall detail of the experiment, i.e.
  - Packing fraction: The correct reporting of a packing fraction is important since any deviations from the real experimental value could easily lead to an incorrect model, as discussed above. Better clarity from the experimentalists can help understand how this aspect of the experiment should be represented in the model.
  - Sphere arrangement in mixing and core regions: According to the French study, this may affect the overall calculated k_{eff} significantly, particularly for the core region (discussed above). A similar study needs to be done for the MCNP5 model in future.
  - Control element design: According to the International Criticality Safety Benchmark Evaluation Project (ICSBEP) database [42] involving the ASTRA critical facility, control rods do have more axial design detail which has not been reported in the current experimental documentation. It could be beneficial to seek more information in this regard from the experimentalists as part of future work.
  - Plugged and unplugged side reflector blocks: All the necessary steps to represent this detail as accurately as possible were taken with the information from the experimental documentation. However, associated pictures from [41] indicate that more side reflector block design detail may need to be represented in the model. Once more, better clarity from the experimentalists can help better understand how this aspect of the experiment should be represented in the model.
- The cross-section data sets used for the analysis. A few sets are available; their usage could be explored further in future.

In summary, the critical pebble bed height analysis using the current MCNP5 model is underestimated by a significant amount (14 cm), a few tests were done to check aspects of the model (sphere representation and packing fraction) and even though more work needs to be done on testing aspects of the model, comparison of the model calculated k_{eff} with the Tripoli4.3 code on a similar configuration shows a similar underestimation margin.

.3 TASK 2 - CONTROL ROD WORTH DEPENDING ON CONTROL ROD POSITION IN THE SIDE REFLECTOR AND INDIVIDUAL CONTROL ROD WORTH WITH THEIR INTERFERENCE

In this section, experimental and calculational control rod worth results are presented, considering different positioning of control rods (CR2 and CR4) in the side reflector, individual control rod worth (CR1, CR2, CR4 and CR5) and control rod combination interference, representing Task 2a and 2b respectively.

Note that for the control rod worth experimental results, the PIR-4 reactivity meter was used (see Appendix B of [9]). The range of reactivity measurements with this system is from $+0.9\beta_{eff}$ to $-26\beta_{eff}$ (0.072 pcm to -18720 pcm) with resolution $0.0001\beta_{eff}$ (all this experimental measurement information is from Appendix B of [9]).

The related ASTRA critical facility configuration as described in the previous section serves as a basis for this task: H_{PB} = 268.9 cm, control elements in out positions, as presented in Table 13 except for MR1, which is located 122.8 cm from the top surface of the bottom reflector.

Task 2a configuration updates cover the full insertion of CR2 and CR4 (insertion limits, h_{in}, as in Table 13) in dedicated unplugged side reflector control rod channels (H-12 and K-5 for CR2 and CR4 respectively, refer to Figure 1) and in varying distance iterations away from the core boundary. The varying distance movement was done in directions A and B (refer to Figure 1) for CR2 and CR4, respectively. Task 2b configuration updates include the full insertion of individual control rods (CR1, CR2, CR4 and CR5), followed by control rod groups insertion into the assembly to determine the effect of interference.

Table 30 presents the measured and calculated control rod worth results as a function of CR2 or CR4 position in the side reflector.

Table 30: Individual control rod worth depending on CR position in the side reflector of Configuration No. 1: H_{PB}= 268.9 cm, all control elements in out positions (refer to Table 13), except MR1 which is inserted to 122.8 cm.

CR type[a]	Block Coordinates		Experimental Control Rod Worth [%][c] [9]	This Work			Control Rod Worth, ρ [%]		
	Block No.	L_N[b], cm		k_{eff}[d]	ρ[e] [%]	(C-E)/E [%]	VSOP94 [36]	PNK[f] [9]	MCNP4B[g] [28]
CR2(h)	H12	12.5	-1.8	0.99285	-1.84	2	-1.72	-1.87	-1.62
CR2	H13	37.5	-0.63	1.00448	-0.68	7	-0.54	-0.56	-0.35
CR2	H14	62.5	-0.16	1.00933	-0.2	24	-0.14	-0.13	-0.15
CR2	H15	87.5	-0.02	1.01081	-0.05	169	-0.02	-0.05	-0.02
CR4	K5	17.7	-1.4	0.99674	-1.45	4	-1.38	-1.43	-1.54
CR4	L4	53	-0.25	1.00885	-0.25	-2	not provided	-0.24	-0.41

[a] Two types of CRs (CR2 and CR4); CR2 was moved along direction A (Figure 1), whilst CR4 was moved along direction B.

[b] L_N - distance between the core boundary and the axis of the CR rod in the graphite block channel (arrangement of the blocks is shown in Figure 1)

[c] The control rod worth for the experiment was processed as $\rho_{CR}\cdot\beta_{eff}$ [%], where ρ_{CR} - is the individual control rod worth and β_{eff} = 0.0072 is the delayed neutron fraction for U^{235} [9]. The experiment's relative error is 0.5%, which translates to at most 7 pcm and a minimum value close to 0.1 pcm for the block CR2 stationed in the H15 graphite block.

[d] The standard deviation for the MCNP5 criticality calculation results is 0.00003.

[e] $\rho = (k_{eff}-k_o)/(k_{eff}\cdot k_o)$, where k_o = 1.01136 is the multiplication factor of the reference plant state, and k_{eff} is calculated for every rod position in the side reflector in the same way.

[f] This is a two-group diffusion approximation code (deterministic) that is used to calculate the effective multiplication factor, neutron fluxes and adjoint functions for cylindrical reactor geometry.

[g] MCNP4B results presented within the document from this point are all calculated for a model with a packing fraction of 0.61 (not the experimental 0.625) and an estimated pebble bed height of 270.5 cm [28].

[h] When measuring the worth of the CR2 rod along direction A (refer to Figure 1), the graphite plug was removed from the channel of block H13.

Figure 17 shows the control rod worth as a function of their position in the side reflector (CR2 and CR4 values are used in the plot as reported in Table 30) together with respectively calculated (C-E)/E values in percentage. The figure also gives more detail on previous contributions of computational tools to the same study.

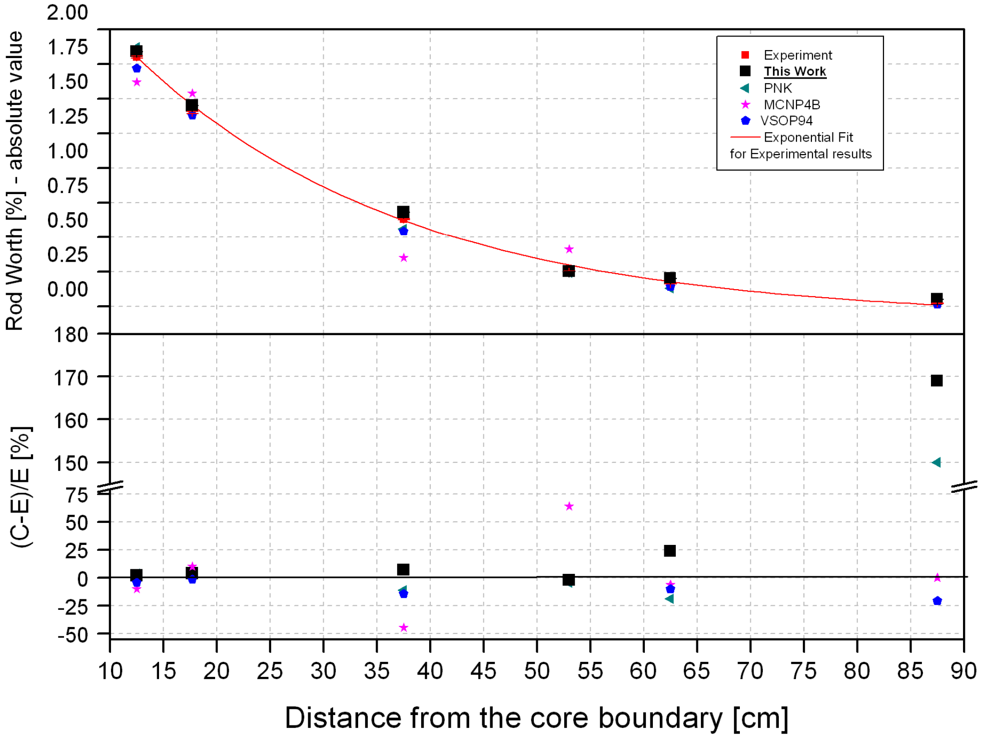

Figure 17: Individual worth of a control rod as a function of its position in the side reflector; CR2 and CR4 are considered, absolute values used and the calculated (C-E)/E values are also presented

MCNP5 control rod worth results for those rods located in graphite block channel axes less than 53 cm from the reactor core boundary indicate a good agreement with experimental values for this benchmark analysis - the reported (C-E)/E values are less than 7% (refer to Table 30). The agreement between the MCNP5 and experimental results is, however, not as good for graphite block channel axis distances beyond 53 cm (measurements and calculations only done for CR2, located at block channel axes of 62.5 cm and 87.5 cm). The two graphite block channel axis steps (C-E)/E values for CR2 are 24% and 169%, respectively. There is an oddly high disagreement for the last CR2 graphite block control rod worth MCNP5 result.

A few trials were done to investigate the CR2 disagreement identified above for the last side reflector block, including plugging and unplugging of the H-13 channel and further converging of the results to a 3 pcm standard deviation.

The first trial covering the plugging and unplugging of the side reflector block, H-13, was done in spite of the experimentalists reporting clearly that this block has been removed from this channel for all the direction A control rod worth experiments (also refer to the note on Table 30). However, this trial was done to discount any potential reasons for the disagreement. Test calculations did not reveal any information leading to the full understanding of the CR2 disagreement.

The second trial covering the need to further converge the calculated k_{eff} values (which are used to calculate the control rod worths) was necessary due to the need to distinguish between the control rod worth results of the last two CR2 positions in the side reflector (these are in close proximity as compared to other control rod worth results; refer to Figure 17). As discussed above, it was decided that a standard deviation of 0.00003 was adequate to address this. Once more, this trial did not reveal any information leading to full understanding of the CR2 disagreement.

The PIR-4 reactivity measurement system covers the range of reactivity measurement required to measure CR2 reactivity, with good reactivity resolution as discussed in the introduction of this section, however, it is also noted that the Kurchatov Institute's PNK results at the same position indicate this disagreement within a similar magnitude, pointing to a possibility that the modelling efforts are missing some experimental detail around the outer side reflector block.

One of the effects that need further investigation in order to find the source of the disagreement is included within the future Task 1 geometrical modelling and a lack of experimental information aspect investigations (see section .2, in particular those which deal with control element design and plugged and unplugged reflector blocks).

In spite of all the above discussions, an important consideration in analysing the control rod worth for the two rods is where the peak neutron flux location is relative to both rods' radial location (one rod could be closer to this than the other, which would affect their neutron absorption effectiveness); this will be investigated further in Task 4. It is important to note that CR2 and CR4 have the same design, however, they are located in slightly different positions around the critical assembly, i.e. CR2 has a centre axis point of 12.5 cm, whilst the CR4's centre axis point is 17.7 cm (this represents a 5.2 cm distance difference measured from the core boundary). Noting these issues, we believe that the different control rod worth capacity of the two rods at similar locations in the side reflector are expected (refer to Table 30). This difference is also confirmed by the experimental results.

In summary, control rod worth results as a function of control rod position in the side reflector, as analysed using MCNP5, show good agreement with the experimental results for positions that are within 53 cm from the core boundary. However, there is a challenge in obtaining similar agreement for positions beyond this distance. In particular, the biggest disagreement with the experimental results is seen at the last side reflector position for CR2, indicating that there is a need to ascertain that there is no possible missing modelling detail for such a case.

At this stage, note that we are moving to Task 2b, which covers the individual control rod worths, their different combination worth and interference.

A collection of all the individual and combination of control rod worths and their interference is listed in Table 31, Note that this represents the ASTRA critical facility Configuration No. 1, where all the control elements in the system are in h_{out} positions (refer to Table 13), except MR1 which is at 122.8 cm and the moved control elements (CR1, CR2, CR4, and CR5) insertion depending on the case being analysed.

Table 31: Individual control rod worth (CR1, CR2, CR4 and CR5), the control rod worth for a combination of rods and their interference coefficients, ASTRA critical facility Configuration No. 1: H_{PB}= 268.9 cm, all control elements in out positions (refer to Table 13), except MR1 which is inserted to 122.8 cm

CR Type[a]	Block Coordinates		Experimental Control Rod Worth [%][b] [9]	This Work			Control Rod Worth, ρ [%]		
	Block No.	L_N[a], cm		k_{eff}[c]	ρ[d] [%]	(C-E)/E [%]	VSOP94 [36]	PNK [9]	MCNP4B [28]
CR1	D8	13	-1.77	0.99279	-1.85	4	-1.68	-1.82	-1.74
CR2[e]	H12	12.5	-1.84	0.9929	-1.84	0	-1.72	-1.87	-1.62
CR4	K5	17.7	-1.4	0.99674	-1.45	4	-1.38	-1.43	-1.54
CR5	H4	12.5	-1.83	0.993	-1.83	0	-1.73	-1.87	-2.21
CR1 + CR5	D8 + H4		-3.72 (1.03)[f]	0.97382	-3.81 (1.07)	2	-3.69 (1.08)	-3.83 (1.04)	-4.13 (1.05)
CR2 + CR5	H12 + H4		-4.01 (1.09)	0.97162	-4.04 (1.14)	1	-3.98 (1.15)	-4.14 (1.11)	-4.39 (1.15)
CR4 + CR5	K5 + H4		-3.11 (0.96)	0.98042	-3.12 (0.99)	0	-3.12 (1)	-3.09 (0.94)	-3.41 (0.91)
CR1 + CR2 + CR5	D8 + H12 + H4		-6.06 (1.11)	0.95148	-6.22 (1.17)	3	-6.07 (1.18)	-6.29 (1.13)	-6.55 (1.18)
CR1 + CR4 + CR5	D8 + K5 + H4		-5.16 (1.03)	0.95994	-5.3 (1.08)	3	-5.26 (1.1)	-5.26 (1.03)	-5.89 (1.07)
CR2 + CR4 + CR5	H12 + K5 + H4		-5.45 (1.07)	0.95789	-5.52 (1.12)	1	-5.59 (1.16)	-5.6 (1.08)	-5.91 (1.1)

[a] L_N - distance between the core boundary and the axis of the CR rod in the graphite block channel (arrangement of the blocks is shown in Figure 1).

[b] The experimental control rod worth is reported as $\rho_{CR}.\beta_{eff}$ [%], where ρ_{CR} - is the individually measured control rod worth and β_{eff} = 0.0072 is the delayed neutron fraction for ^{235}U [9]. The experiment's relative error for individual control rod measurements is 2.5%, whilst that of the combination of control rods is 0.5%.

[c] The standard deviation for the MCNP5 criticality calculation results is no more than 0.00004 for single rod worth calculations and 0.00021 for all the combinations of control rods calculations.

[d] $\rho = (k_{eff}-k_o)/(k_{eff} \cdot k_o)$, where k_o = 1.01136 is the multiplication factor of the reference plant state, and k_{eff} is calculated for every rod position in the side reflector in the same way.

[e] When measuring the worth of the CR2, the graphite plug was inserted in the channel of block H13.

[f] The value within the brackets is the coefficient of control rod interference ξ, which is determined as $\xi = \Delta R/\Sigma\rho_I$. ΔR is the total worth of the corresponding combination of rods, ρ_I is the worth of individual rod I being inserted in the critical assembly (only MR1 inserted).

The MCNP5 control rod worth results for both the individual and group control rods agree well with the measured values (refer to Table 31). The reported (C-E)/E percentage values are no more than 4%. The control rod worth interference MCNP5 results also show a good agreement when compared with experimental values. The calculated (C-E)/E percentage values are below 5%.

It can also be seen in Table 31 that for interference coefficients computed as part of accounting for a combination of control rod worths, the MCNP5 results show the same behaviour as that of the experiment. This means that for a combination of two control rods, the minimum interference (reference for no interference is coefficient equal to 1) of -0.01 is seen for rods that make a 45° angle between themselves (CR4+CR5) and the maximum interference of 0.14 (reference for no interference is coefficient equal to 1) is seen for rods that are opposite each other, at a 180° angle (CR2+CR5).

In order to fully understand the meaning of the reported interference coefficients, more information is needed about the thermal flux profiles during the execution of the experiment. This has not been done in this work and is planned for future work.

The maximum interference (reference for no interference is coefficient equal to 1) of 0.17 was obtained for the combination of three rods CR1+CR2+CR5; the same observation can be seen for the experimental results.

This task was also modelled and calculated by other benchmark participants using other computational tools. In general, for both types of computational tools (Monte Carlo and deterministic), there is a good agreement between the experimental and calculated results for the individual and combination control rod worths.

MCNP5 seems to be quite good at representing this benchmark task. (C-E)/E results are all less than 5%.

.4 TASK 3A - CONTROL ROD REACTIVITY DEPENDING ON DEPTH OF INSERTION IN SIDE REFLECTOR

This section presents experimental and calculational control rod worth results for CR5 and MR1 as a function of their depth in their respective side reflector channels (both part of Task 3a). Note that this analysis is done for two Configuration No. 1 updates, with the first represented by all the control elements in the system to be in h_{out} positions (refer to Table 13), except for MR1 which is at 122.8 cm, and for CR5, which is inserted in the side reflector channel in a stepwise manner. The second Configuration No. 1 update is done in the same way as the CR5 update, except that in this case an MR1 is inserted in the side reflector channel in a stepwise manner.

Table 32 lists the first update control rod worth results for CR5 as a function of its depth of insertion in the side reflector channel and Figure 18 presents the normalized CR5 differential reactivity as a function of its depth of insertion in the side reflector.

Table 32: CR5 worth and (C-E)/E results as a function of varying depth of insertion in the side reflector ASTRA critical facility Configuration No. 1: H_{PB}= 268.9 cm, all control elements in out positions (refer to Table 13), except MR1 which is inserted to 122.8 cm

Insertion Step	**Experimental Depth of the Rod Insertion in the Assembly ($H-H_o$) [a] [cm]**	**MCNP5 Insertion Coordinate[b] [cm]**	**Experimental Control Rod Worth [$][c] [9]**	**This Work**			**Control Rod Worth, ρ [$]**	
				k_{eff}	ρ^d **[$]**	**(C -E)/E [%]**	**VSOP94[e] [36]**	**MCNP4B [28]**
1	0	354	0	1.01136 (3)[f]	0	N/A	0	
	50.3	303.7					0.006	
	92.7	261.3					-0.041	
	127.7	226.3					-0.04	
2	128.1	225.9	-0.112	1.01047 (3)	-0.121	8		-0.221
3	145.6	208.4	-0.207	1.00962 (4)	-0.237	14		-0.353
	149.8	204.2					-0.076	
	172.5	181.5					-0.186	
4	181.2	172.8	-0.533	1.00695 (4)	-0.601	13		-0.87
	195.2	158.8					-0.395	
5	198.6	155.4	-0.757	1.00534 (4)	-0.822	9		-1.02
	218	136					-0.708	
6	224.7	129.3	-1.143	1.00243 (4)	-1.223	7		-1.722
	240.8	113.2					-1.094	
7	244.9	109.1	-1.469	1.00000 (8)	-1.56	6		-1.978
8	261.6	92.4	-1.737	0.99845 (7)	-1.776	2		-2.0202
	262.4	91.6					-1.507	
9	276.9	77.1	-1.95	0.99676 (8)	-2.012	3		-2.244
10	284.4	69.6	-2.067	0.99635 (9)	-2.069	0		-2.629
	286.4	67.6					-1.904	
11	300.5	53.5	-2.253	0.99490 (9)	-2.272	1		-2.828
	308.5	45.5					-2.217	
	331.9	22.1					-2.426	
12	342.7	11.3	-2.543	0.99297 (8)	-2.543	0		-3.664
		0					-2.53	

[a] H – current position of the rod along the assembly height by the measuring scale attached to the outside of the rod.

H_o = 100.6 cm – initial point of reading position of the rod withdrawal from the assembly by the measuring scale.

[b] Measured from the top surface of the bottom reflector.

[c] The experimental control rod worth units are $, obtained by dividing the reactivity calculated via k_{eff} values with β_{eff}, where $\beta_{eff} = 0.0072$ is the delayed neutron fraction for U^{235} [9]. The experimental error in measured reactivity is a maximum of 2.5%.

[d] $\rho = (k_{eff}-k_o)/(k_{eff}\cdot k_o)*(1/\beta_{eff})$, where $k_o = 1.01136$, k_{eff} is calculated for every rod position in the side reflector and $\beta_{eff} = 0.0072$.

[e] VSOP data digitized from Figure 7 [36].

[f] Read as 1.01136 ± 0.00003, similar for following cases.

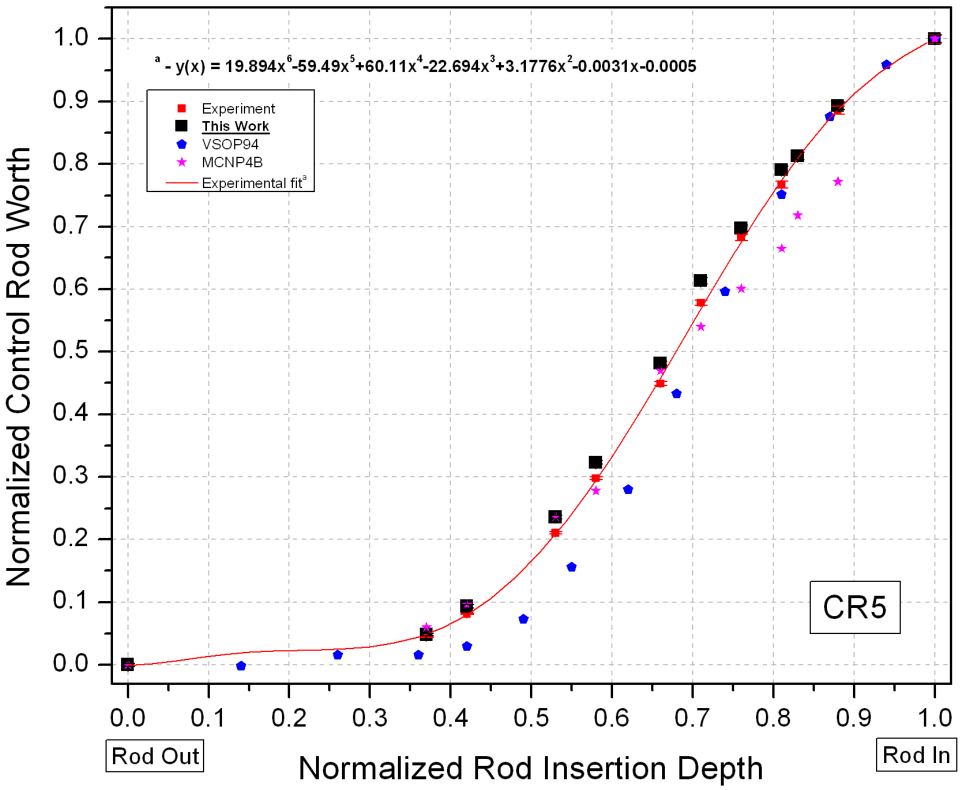

Figure 18: Normalized CR5 differential reactivity as a function of its insertion in the side reflector, Configuration no.1, H_{PB} = 268.9 cm

The calculated MCNP5 control rod worth results as reported in Table 32 indicate a good agreement with experimental results for all the insertion depths. In general the (C-E)/E values for all insertion depths are below 14%.

The control rod worth values for each of the first two insertion depths (Rod Out) are quite close to one another, thus for MCNP5 k_{eff} calculations that are not well converged, it is impossible to separate between the two plant state results. In order to address this issue, we converged each of the k_{eff} calculations to a 0.00003 standard deviation. Since the control rod worth results for rest of the insertion depth cases did not present the same convergence problem, the k_{eff} standard deviation for these cases did not exceed 0.00009. Judging by the comparison between the calculated and experimental control rod worths (presented via the (C-E/E) values in Table 32) for all the cases, no convergence issues could be further identified following the resolution for those mentioned above.

The control rod worth trends from other computational tools used to calculate this benchmark task are similar as compared to the experimental results.

MCNP5 is good at representing this benchmark task, (C-E)/E results are all less than 14%.

Concerning the differential reactivity worth for the MR1 rod, Table 33 lists the control rod worth as a function of depth of its insertion in the side reflector channel. Figure 19 shows the normalized MR1 differential reactivity as a function of its depth of insertion in the side reflector.

Table 33: MR1 reactivity worth and (C-E)/E results as a function of varying depth of insertion in the side reflector ASTRA critical facility Configuration No. 1: H_{PB}= 268.9 cm, all control elements in out positions (refer to Table 13)

Insertion Step	Experimental Depth of the Rod Insertion in the Assembly $(H-H_o)$[a] [cm]	MCNP5 Insertion Coordinate[b] [cm]	Experimental Control Rod Worth [$][c] [9]	**This Work**			Control Rod Worth, ρ [$]
				k_{eff}	ρ^d [$]	(C-E)/E [%]	MCNP4B [28]
1	0	356	0	1.01212 (3)[e]	0	n/a	0
2	76.5	279.5	-0.001	1.01212 (3)	0	-100.0	-0.141
3	146.6	209.4	-0.015	1.01199 (3)	-0.018	17.5	-0.280
4	180.6	175.4	-0.047	1.01184 (3)	-0.038	-19.2	-1.061
5	221.3	134.7	-0.076	1.01156 (4)	-0.076	0	-1.314
6	247	109	-0.1	1.01134 (4)	-0.106	5.8	-1.499
7	267.7	88.3	-0.118	1.01114 (4)	-0.133	12.7	-2.161
8	291.1	64.9	-0.135	1.01096 (3)	-0.157	16.6	-2.242
9	345.9	10.1	-0.157	1.01077 (4)	-0.183	16.7	-2.657

[a] H – current position of the rod along the assembly height by the measuring scale attached to the outside of the rod.

H_o = 99.3 cm – initial point of reading position of the rod withdrawal from the assembly by the measuring scale.

[b] Measured from the top surface of the bottom reflector.

[c] The experimental control rod worth units are $, obtained by dividing the reactivity calculated via k_{eff} values with β_{eff}, where β_{eff} = 0.0072 is the delayed neutron fraction for U^{235} [9]. The experimental error in measured reactivity is a maximum of 2.5%.

[d] $\rho = (k_{eff}-k_o)/(k_{eff}\cdot k_o)*(1/\beta_{eff})$, where k_o = 1.01212 (MR1 in completely out position, not the normal 122.8 cm), k_{eff} is calculated for every rod position in the side reflector and β_{eff} = 0.0072.

[e] Tead as 1.01212 ± 0.00003, similar for following cases.

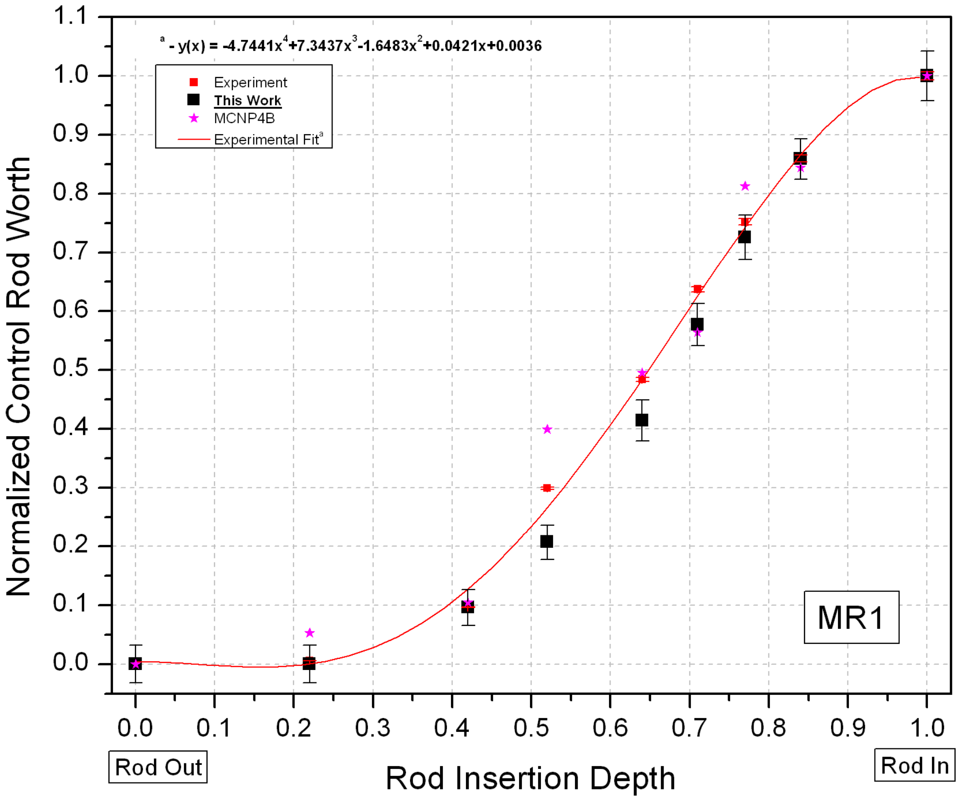

Figure 19: Normalized MR1 differential reactivity as a function of its insertion in the side reflector, ASTRA critical facility, Configuration No.1, H_{PB} = 268.9 cm

The calculated MCNP5 control rod worth results (Table 33) reasonably agree with the experimental values below the insertion depth of 209.4 cm. The reported (C-E)/E values are below 19.2%. However, the MCNP5 result for the initial insertion step does not agree with the experiment, with a large (C-E)/E value reported.

Note that MR1 on full insertion in the side reflector channel (ρ = -0.183$) provides approximately 14 times less control rod worth than CR5 rod (ρ = -2.543$). This means that the calculational effort to quantify MR1 worth is in general expected to be higher, thus indicating a general further convergence requirement for the k_{eff} calculations. Experimentally, the kind of MR1 control rod worth magnitude and resolution reported seems to be well covered by the PIR-4 reactivity measurement system.

Once more, the MR1 control rod worth for each of the first three insertion depths (Rod Out) is quite close to one another, thus for MCNP5 k_{eff} calculations that are not well converged, it is impossible to separate the three plant state results. In order to address this issue, we converged each of the three k_{eff} calculations to a 0.00003 standard deviation and 0.00004 for the rest of the k_{eff} calculations.

MCNP5 is reasonably good at representing most of this benchmark task at insertion distances below 209.4 cm, with (C-E)/E results less than 19.2%. However, there is a challenge in getting the same agreement in the initial insertion step, with the need to converge this k_{eff} calculation further; a large (C-E)/E value is reported.

.5 TASK 3B - ASSEMBLY REACTIVITY AS A FUNCTION OF PEBBLE LOADING HEIGHT

This section presents experimental and calculational reactivity worth results for various ASTRA pebble loading heights.

Experimentally (see [9] for details), pebble layers were loaded in a stepwise manner, on top of the initial critical pebble bed height of 268.9 cm ±1.5 cm, up to a pebble height of 320.8 cm and at each step, integral assembly and differential layer reactivity measurements were performed.

It is worth remembering that the ASTRA critical facility Configuration No. 1 as modelled in Task 1, using MCNP5, overestimates k_{eff} by 1 123 pcm. Even though this configuration gives an overestimation of the calculated k_{eff}, it was used as the basis for loading the necessary layers in the same manner as the experiment, with the final reactivity calculations done taking this state as the reference state.

Table 34 lists the assembly and pebble layer reactivity results as a function of pebble loading height and Figure 20 primarily shows the assembly reactivity as a function of pebble bed loading height.

Table 34: ASTRA critical facility assembly reactivity as a function of the pebble bed loading height, Configuration No. 1: H_{PB}= 268.9 cm, all control elements in out positions (refer to Table 13), except MR1 which is inserted to 122.8 cm

Pebble Bed Height (cm)	**Number of Pebbles**	**Experiment**		**This Work**					**Assembly Reactivity [$],ρ**
		Assembly Reactivity [$], ρ	**Pebble Layer Reactivity [$], Δρ**	k_{eff}	**ρ^a [$]**	**Assembly (C-E)/E [%]**	**$\Delta\rho^b$ [$]**	**Layer (C-E)/E [%]**	**MCNP4B [40]**
268.9	38584	0.1 ± 0.01	-	1.01136 (3)[c]	0.090	-10	-	-	0.1
274.4	39432	0.64 ± 0.01	0.54 ± 0.01	1.01524 (4)	0.615	-4	0.525	-3	0.566
281.4	40280	1.14 ± 0.01	0.50 ± 0.02	1.01969 (6)	1.212	6	0.597	19	1.227
285.9	41128	1.58 ± 0.01	0.44 ± 0.02	1.02242 (6)	1.575	0	0.364	-17	1.795
291.8	41976	2.01 ± 0.01	0.43 ± 0.02	1.02605 (6)	2.056	2	0.481	12	2.459
297.4	42824	2.43 ± 0.02	0.42 ± 0.02	1.02896 (19)	2.439	0	0.383	-9	2.907
303.5	43672	2.85 ± 0.02	0.42 ± 0.02	1.03266 (20)	2.922	3	0.484	15	3.360
309.4	44520	3.26 ± 0.02	0.41 ± 0.02	1.03547 (20)	3.287	1	0.365	-11	3.695
315.2	45368	3.66 ± 0.02	0.40 ± 0.02	1.03882 (19)	3.720	2	0.433	8	4.211
320.8	46216	4.03 ± 0.02	0.37 ± 0.02	1.04091 (21)	3.988	-1	0.268	-27	4.602

[a] This is the assembly reactivity in dollars, calculated as: $\rho = (k_{eff}-k_o)/(k_{eff}\cdot k_o)*(1/\beta_{eff})$, where k_o = 1.01136, k_{eff} is calculated for every pebble layer load and β_{eff} = 0.0072. Note that in order to maintain the same experimental reference (which takes into account the MR1 control rod worth inserted to 122.8 cm – measured from the top of the bottom reflector) from which to calculate MCNP5 assembly and layer reactivity, the MR1 control rod reactivity of -0.09$ (as interpolated from Table 33 MCNP5 results) is included on all MCNP5 assembly reactivity results presented.

[b] This is the pebble layer reactivity in dollars, calculated as: $\rho - \rho_{PR}$, where ρ is the assembly reactivity for a given pebble bed load and ρ_{PR} is the previous pebble bed load reactivity.

[c] Read as 1.01136 ± 0.00003, similar for following cases.

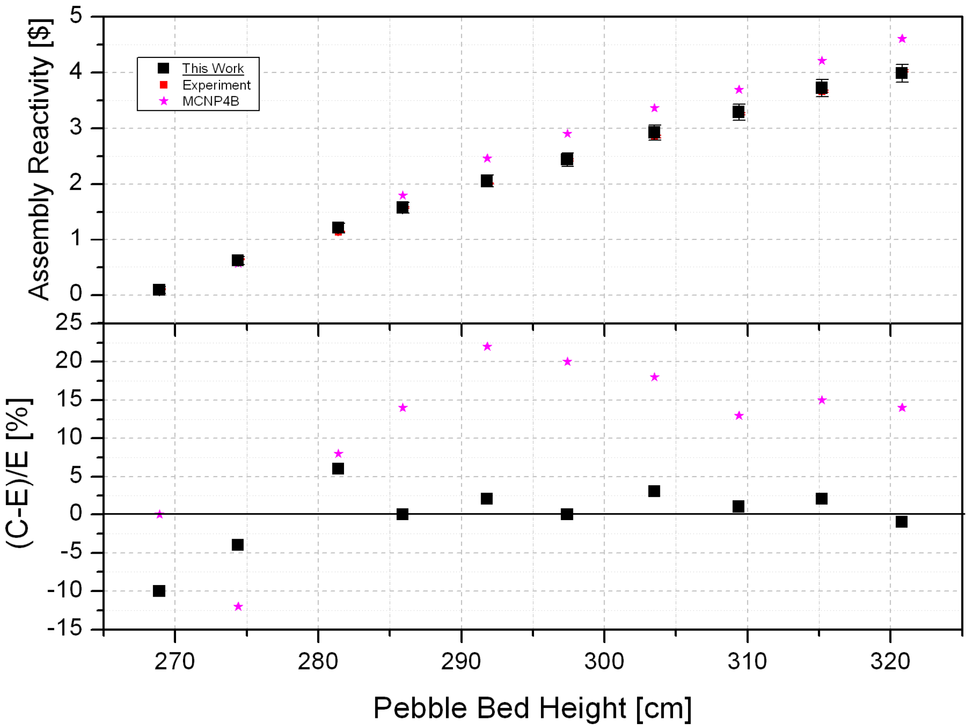

Figure 20: Assembly reactivity as a function of pebble bed loading height, ASTRA critical facility, Configuration no.1, H_{PB} = 268.9 cm

In general (refer to Table 34 and Figure 20), there is very good agreement between the experimental and MCNP5 calculational values for assembly reactivity analysis; (C-E)/E values are below 7%. However, when making comparisons between pebble layer loading experimental and MCNP5 results, the agreement is not as good, with (C-E)/E values below 27%.

The reason for this difference in agreement for the two cases can be found in the modelling approach followed. This indicates that when the assembly reactivity results are compared (experiment and MCNP5), the effect of sphere cutting on geometry boundaries is almost unfelt (globally this contributes a small portion of the overall pebble count). This is mainly due to a low ratio of spheres being cut as compared to the total represented. However, when looking at the same analysis on pebble layer loading, the sphere cutting effect is felt more readily since the ratio of the total spheres cut on the geometry boundaries to the total spheres represented in the layer is larger.

MCNP5 is very good at representing the assembly reactivity part of this benchmark task, with (C-E)/E values are all less than 7%. However, when it comes to pebble layer loading reactivity, there is less agreement, with (C-E)/E values less than 27%.

.6 TASK 4 - REACTION RATES DISTRIBUTION

.6.1 Introduction and Procedure

This section presents the introduction and procedure followed in order to quantify the spatial distribution of reaction rates as calculated for the ASTRA critical facility assembly.

This task is performed on a Configuration No. 1 for the ASTRA critical facility, taking into account a 268.9 cm pebble bed height and all control elements in h_{out} positions (refer to Table 13), except MR1 which is at 122.8 cm above the top surface of the bottom reflector.

Three types of detectors were considered: ^{115}In, ^{164}Dy and ^{235}U, refer to section .2.4 for more detail. The measured reactions for the detectors were ^{115}In (n, γ), ^{64}Dy (n, γ) and ^{235}U (fission).

Experimentally, the indication is that at a fixed power level, all gamma activity measurements were performed for each detector of interest and for the monitor detector (this monitor was used to exclude time dependence in the measurements by the normalisation of the obtained detector activity values to the value of the detector-monitor activity at the same measurement time). Without going into a detailed explanation about the measurement system and computer processing of the data, the reported reaction rates are given as a ratio to the monitor detector (thus relative units are used).

Since the positions of each ordinary and monitor detector are known exactly, it is expected that the relative reaction rate results for all the detector types monitor position would report a value equal to 1. This is the case for the ^{115}In and ^{164}Dy detectors with monitor results reporting a relative reaction rate of 1. However, when considering experimental data reported for the ^{235}U detector (whose monitor is located at Channel N1, h = 130 cm), firstly no monitor relative reaction rate is provided and by using the results provided (nearest detector results in channel N1, represented by a height of 100 cm and 135 cm), there is a clear indication that the relative reaction rate at the said monitor position would not be equal to 1. This indicates a clear discrepancy. Thus far, with the provided information, we understand the mass of ordinary and monitor detectors to be the same. However, it is also reported that both detector masses were not known exactly. This could be the reason why this discrepancy is noticed in the reported ^{235}U reaction rate results. In spite of this, it must be stated clearly that we do not fully understand the source of this discrepancy.

This presents our main problem in an effort to reproduce the same reaction rate distribution results as the experiment throughout the assembly. In seeking more clarity on the followed experimental procedure, it was identified that Appendix A of [11] presents the following relationship for finding the relative detector activity A_{u_j} per unit mass of the fissile material (^{235}U):

$$A_{u_j} = \frac{A_{D,j}}{A_{mon,j}} = \left[\frac{N_{D,j} - N_{NaI}^{(n)} - N_{D,j}^{(n)}}{M_{D,j}} \right] \bullet \left[\frac{N_{mon} - N_{NaI}^{(n)} - N_{mon}^{(n)}}{M_{mon}} \right]^{-1} \tag{4}$$

where:

$A_{D,j}$ – characterises the fission activity in the j-th uranium detector;

A_{mon} – characterises the fission activity in the uranium monitor;

$N_{D,j}$ – characterises number of fissions in the j-th uranium detector;

$N_{D,j}^{(n)}$ – background level in the uranium detector determined prior to irradiation in the assembly;

$N_{NaI}^{(n)}$ – background level in the scintillation counter (NaI crystal);

$M_{D,j}$ – mass of fissile material (^{235}U) in the uranium detector;

N_{mon} – characterises the number of fissions in the uranium monitor;

$N_{mon}^{(n)}$ – background level in the detector-monitor;

M_{mon} – mass of fissile material (^{235}U) in the detector-monitor.

which helps to understand how the experimental relative reaction rates were processed. One is also able to identify possible sources of uncertainties in the equation. As mentioned before, the masses of ordinary and monitor detectors are an obvious source of uncertainty in the equation.

The way in which we calculate the individual detector reaction rates is such that the same atomic density is used on all detectors (this following experimental documentation which seems to indicate that the mass for ordinary and monitor detectors is the same); therefore we further eliminate the need to consider mass in our analysis. Since we have already identified the suspicious relative reaction rate result at the monitor position for the ^{235}U detector, our subsequent analysis is done through the use of the following relationship:

$$A_{u_j} = F \cdot A_{u_j}^{MCNP5} \tag{5}$$

where:

A_{u_j} − characterises the experimental relative reaction rate in the ^{235}U monitor;

$A_{u_j}^{MCNP5}$ − characterises the un-normalized MCNP5 relative reaction rate in the j-th uranium detector;

F − this the normalization factor applied to all the ^{235}U MCNP5 detector reaction rates
in order to obtain relative reaction rates.

In the above equation, we consider the MCNP5 un-normalized relative reaction rate ($A_{u_j}^{MCNP5}$) to be proportional to the experimental relative reaction rate in a specific detector (A_{u_j}) and then try to compute a normalization factor that brings us to the experimental result. Since this is done for all the ^{235}U detectors, this factor should be common for all the MCNP5 results that need to be normalized in order to obtain relative reaction rates to be compared with their experimental counterparts. The common normalization factor is obtained via minimizing the sum square distance between the experimental and calculated results. The following equation shows this relationship:

$$\sum (A_{u_j} - F \cdot A_{u_j}^{MCNP5})^2 = \min \tag{6}$$

with F representing the said normalization factor. This factor was determined to be 1.178. All the reported ^{235}U MCNP5 relative reaction rates are normalized with this factor. As mentioned before, this normalization approach was not considered for the ^{115}In and ^{164}Dy detectors, since their monitor reaction rate normalized results did not indicate the same discrepancy as that identified for the ^{235}U detector.

The next two sections present the axial and radial reaction rate profiles, as calculated using MCNP5 for different detector types as explained above.

In all the reaction rates profile plots, a PC Cristall profile is shown, which only serves the purpose of comparing the MCNP5 and experimental results against a Kurchatov Institute tool for the same experimental representation.

.6.2 Task 4a - Axial Reaction Rates Distribution in Channels N1 and N5

This section presents experimental and MCNP5 reaction rate results for detectors located in varying heights for channels N1 (r_1 = 6.75 cm) and N5 (r_5 = 80.35 cm). Three types of detectors were used for this analysis; ^{235}U, ^{115}In and ^{164}Dy. For more information on their design, refer to section .2.4.

Table 35 presents the distribution of ^{235}U detector reaction rates along the critical assembly height h, in Channels N1 (r_1 = 6.75 cm) and N5 (r_5 = 80.35 cm). Table 36 presents the distribution of ^{164}Dy and ^{115}In detector reaction rates along the critical assembly height h, in Channel N1.

Figure 21, Figure 22 and Figure 23 show the reaction rate profiles for channel N1 (r_1 = 6.75 cm) obtained from the ^{235}U, ^{164}Dy and ^{115}In detectors respectively. Figure 24 shows the ^{235}U reaction rate profile for channel N5 (r_5 = 80.35 cm).

Table 35: Distribution of Uranium detector[(a)] Reaction Rates along the Critical Assembly Height in Channels N1 and N5 for Configuration No. 1 (H_{PB} = 268.9 cm)

Channel N1 (r_1[(b)] = 6.75 cm)					**Channel N5 (r_5[(b)] = 80.35 cm)**		
j	Coordinate along the height h_j[(c)], cm	Reaction rate A[(d)] [relative units]		j	Coordinate along the height h_j[(c)], cm	Reaction rate A[(d)] [relative units]	
		Experiment[(e)] [10]	This Work[(f)]			Experiment [10]	This Work[(f)]
				1	10	0.445	0.375 (-16)
2	30	0.942	0.901(-4)[(g)]	2	30	0.448	0.428 (-4)
3	50	1.005	1.021 (2)	3	50	0.53	0.478 (-10)
4	70	1.106	1.112 (1)	4	70	0.596	0.536 (-10)
5	85	1.182	1.162 (-2)	5	85	0.595	0.556 (-7)
6	100	1.146	1.19 (4)	6	100	0.631	0.578 (-8)
7	135	1.175	1.173 (0)	7	135	0.568	0.572 (1)
8	160	1.041	1.078 (4)	8	160	0.543	0.525 (-3)
9	205	0.735	0.77 (5)	9	205	0.384	0.379 (-1)
10	250	0.313	0.302 (-4)	10	250	0.17	0.172 (1)

(a) The MCNP5 modelled uranium detectors are as specified in Table 14. Further detector information can also be found as part of section .2.4.

(b) Radial distances at which the experimental channels are located in the assembly (Figure 6 and section .3.4).

(c) The experimental channels height h_j has been measured from the top surface of the bottom reflector.

(d) The experimental reaction rates A are normalized to the ^{235}U (monitor) located in channel N1 at h = 130 cm (refer to also Figure 6). However, the value of this detector is not reported in the experimental documentation. The approach used in normalizing the values for MCNP5 calculations is explained in section .6.1.

(e) The experimental measurement of gamma activity has an associated relative error of 3% per detector (monitor and ordinary) measured.

(f) MCNP5 reaction rates tallies have a relative error less than 1% and all pass the 10 statistical checks done by MCNP.

(g) The value in brackets represents the calculated (C-E)/E difference in percentage [%].

Table 36: Distribution of Dysprosium and Indium detector[(a)] Reaction Rates along the Critical Assembly Height in Channel N1[(b)] for Configuration No. 1 (H_{PB} = 268.9 cm)

Dysprosium Detector				**Indium Detector**			
	Coordinate along the height h_j[(c)], cm	Reaction rate A[(d)] [relative units]			Coordinate along the height h_j[(c)], cm	Reaction rate A[(d)] [relative units]	
		Experiment [(e)] [10]	This Work[(e)]			Experiment [10]	This Work[(e)]
1	30	0.781	0.77 (-1)[(f)]	1	30	0.888	0.739 (-17)
2	70	0.994	0.949 (-5)	2	70	1.141	0.934 (-18)
3	135	1	1 (0)	3	135	1	1 (0)
4	205	0.584	0.656 (12)	4	205	0.534	0.671 (26)
5	250	0.234	0.257 (10)	5	250	0.311	0.272 (-13)

(a) The MCNP5 modelled dysprosium and indium detectors are as specified in Table 15 and Table 16 respectively. More details about the detectors can also be found as part of section .2.4.

(b) Channel N1 is located within the reactor cavity, at the radial distance of r_1 = 6.75 cm.

(c) The experimental channels height h_j has been measured from the top surface of the bottom reflector.

(d) Reaction Rates A are normalized to a respective detector located in channel N1 at h = 135 cm (refer to also Figure 6).

(e) MCNP5 reaction rates tallies have a relative error less than 1% and all but one (at h = 70 cm, which fails only one test) pass the 10 statistical checks done by MCNP.

(f) The value in brackets represents the calculated (C-E)/E difference in percentage [%].

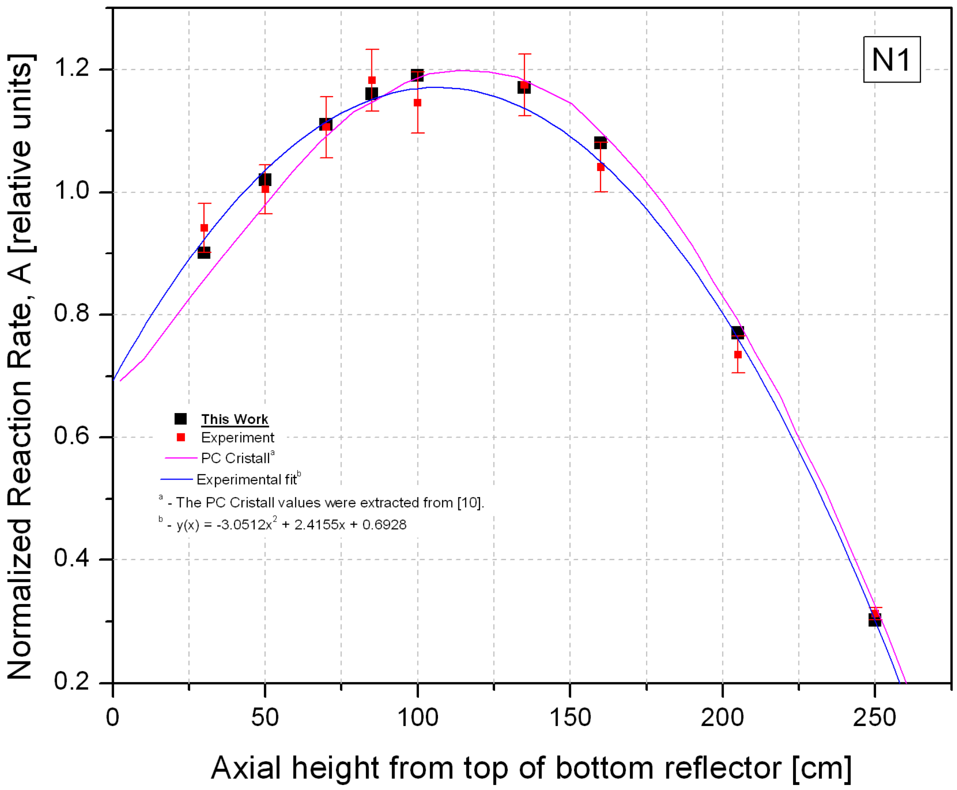

Figure 21: U^{235} detector normalized reaction rate axial profile at a radial position of 6.75 cm, ASTRA critical facility Configuration No. 1, H_{PB} = 268.9 cm

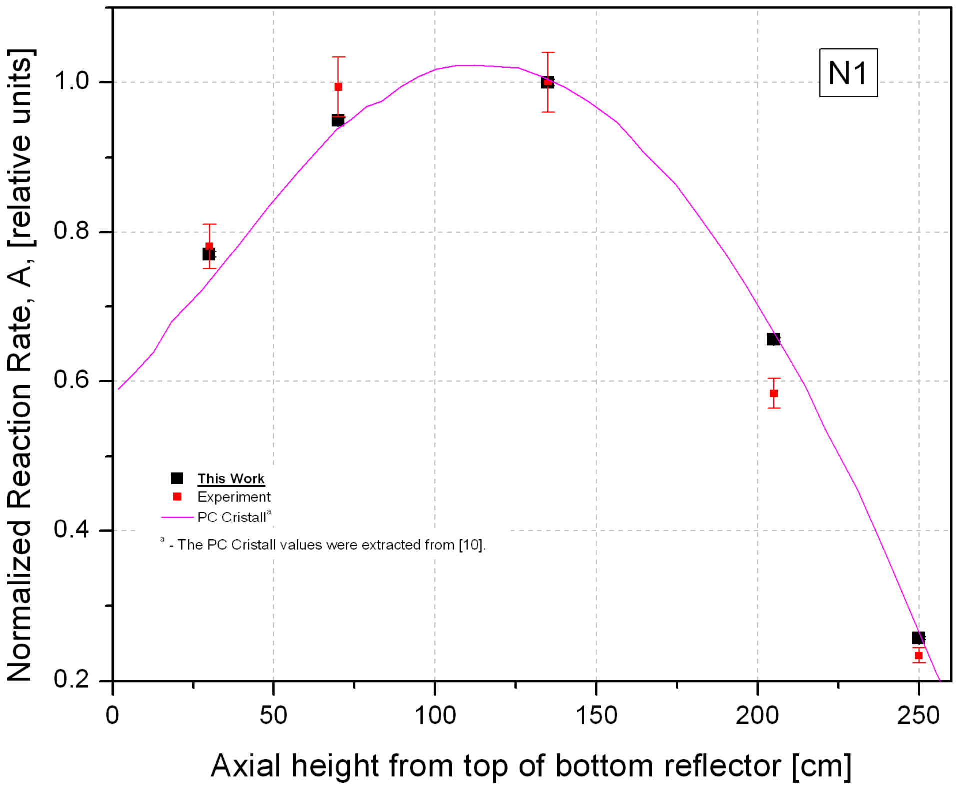

Figure 22: Dysprosium detector normalized reaction rate axial profile at a radial position of 6.75 cm, ASTRA critical facility Configuration No. 1, H_{PB} = 268.9 cm

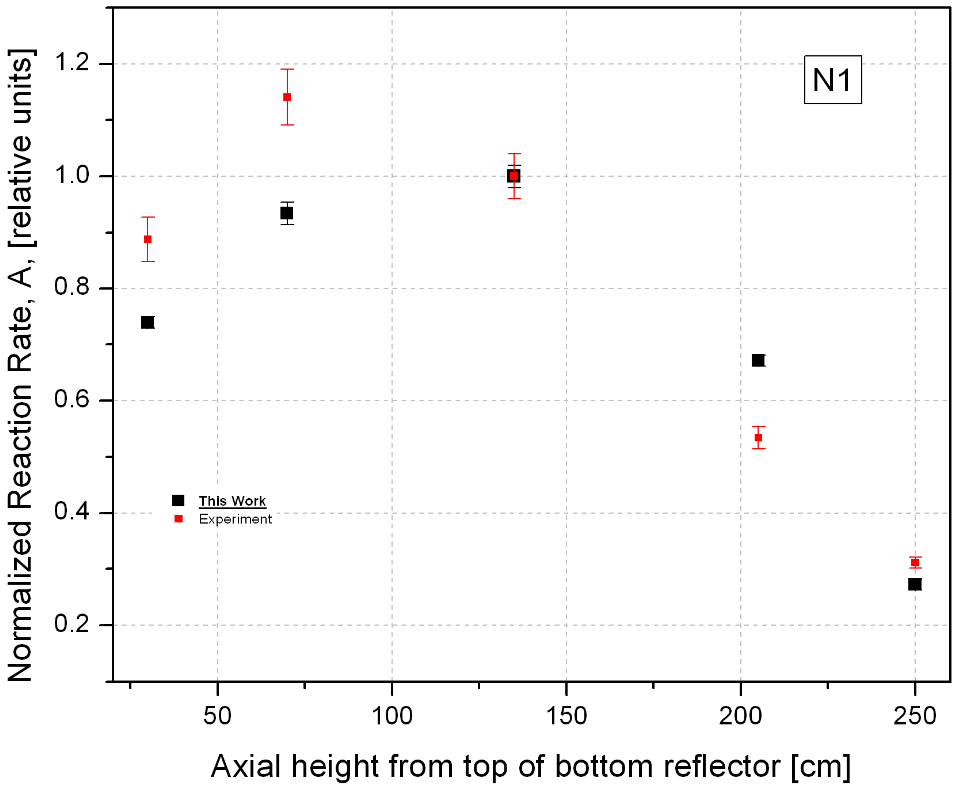

Figure 23: Indium detector normalized reaction rate axial profile at a radial position of 6.75 cm, ASTRA critical facility Configuration No. 1, H_{PB} = 268.9 cm

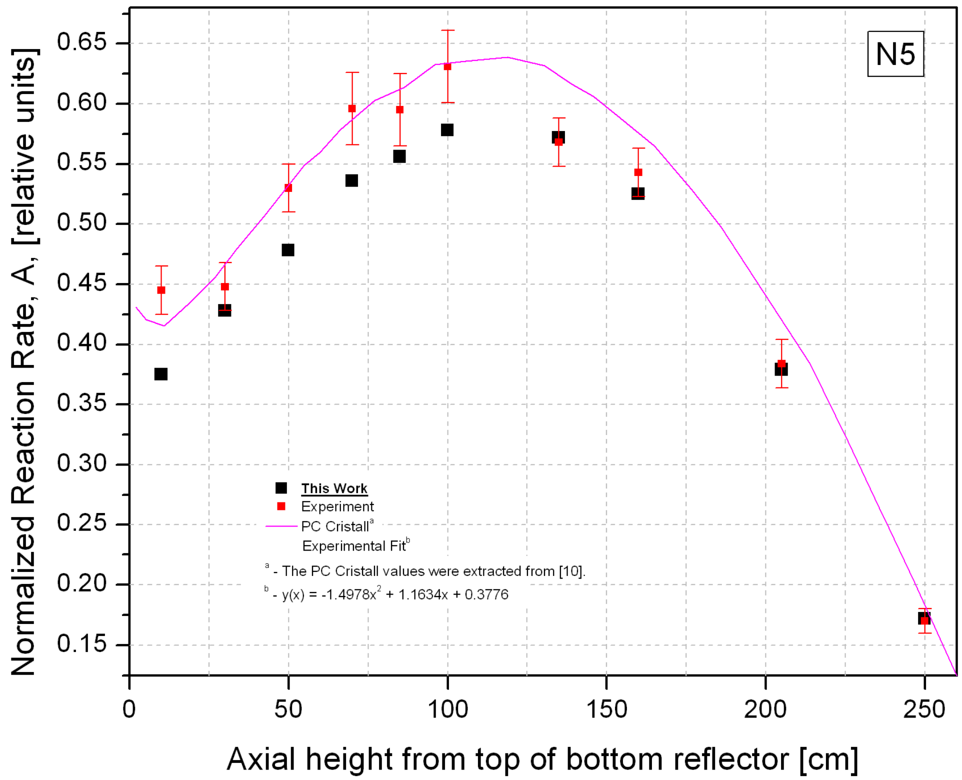

Figure 24: U^{235} detector normalized reaction rate axial profile at a radial position of 80.35 cm, ASTRA critical facility Configuration No. 1, H_{PB} = 268.9 cm

The MCNP5-computed ^{235}U axial reaction rate results for channel N1 (r_1 = 6.75 cm) show a very good agreement with the experimental results; with the reported (C-E)/E values below 5% (refer to Table 35 and Figure 21). The good agreement seen in channel N1 analysis (particularly with the ^{235}U detector) is believed to be mainly due to this region being well represented (only graphite spheres surround the immediate outer radius for this experimental channel). MCNP5 results for the other two detectors (dysprosium and indium) show lesser agreement with the experimental results (refer to Table 36) - reported (C-E)/E values for the dysprosium detector are as high as 12%, whilst those for the indium detector are as high as 26%.

The MCNP5-computed ^{235}U axial reaction rate results for channel N5 (r_5 = 80.35 cm) show a very good agreement with the experimental results for heights above 135 cm, with the reported (C-E)/E values below 3% (refer to Table 35 and Figure 24). However, for heights lower than 135 cm, the agreement is not as good, with (C-E)/E values below 16%).

Even though the experiment mentions very clearly that there is no top reflector for the current modelled Configuration No. 1 ASTRA critical facility, we have studied further the effect of including a top reflector in our model. An illustration of how the inclusion of the top reflector affects the N5 profile can be seen in Figure 25.

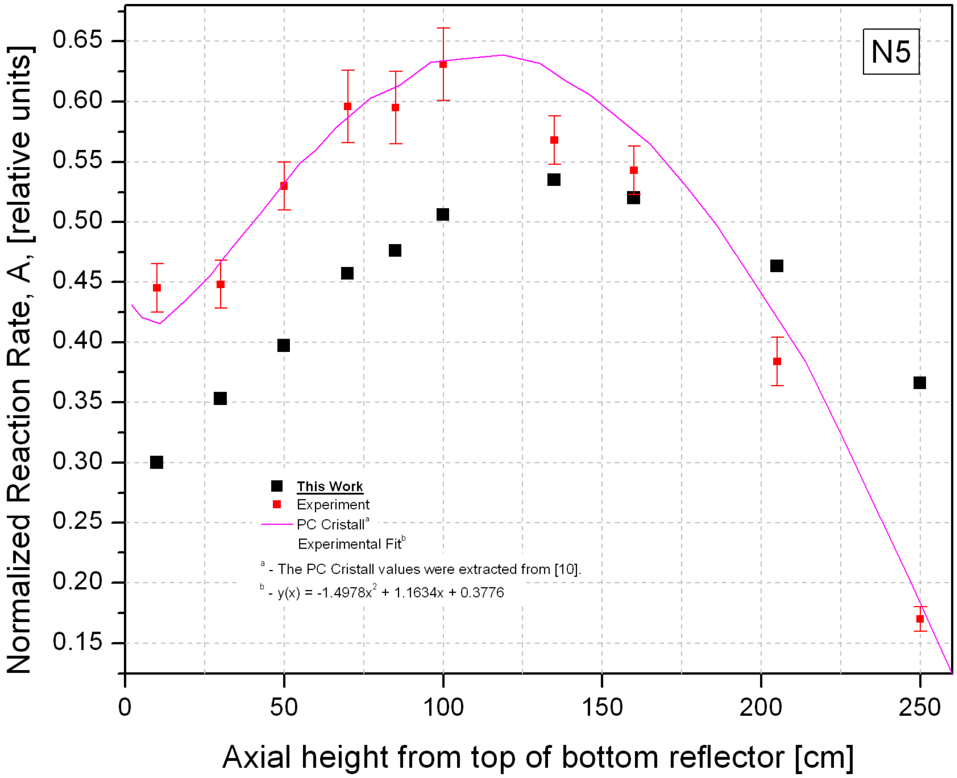

Figure 25: U^{235} detector normalized reaction rate axial profile at a radial position of 80.35 cm, ASTRA critical facility Configuration No. 1, H_{PB} = 268.9 cm with a Top Reflector

This study indicates that the reasons for the lack of agreement seen in the lower experimental channel N5 between MCNP5 and experimental results is not due to not modelling the top reflector, in line with what the experiment specifications provided in the first place. We currently do not understand the reason for the odd shape in the lower section of channel N5.

In general, MCNP5 does well in representing this benchmark task (Task 4a), particularly for channel N1 (r_1 = 6.75 cm) considering the ^{235}U and ^{164}Dy detectors; there is a challenge in getting the same agreement for the ^{115}In detector. When considering channel N5, we find that MCNP5 does well representing heights above 135 cm, however, for the detectors located lower than this, there is a challenge in getting the same agreement.

.6.3 Task 4b - Radial Reaction Rate profiles across the assembly in heights h = 135 cm and h = 205 cm

In this section, experimental and calculational results are presented for detectors located at the same heights (135 cm and 205 cm), and varying only in radial distances across the ASTRA critical facility Configuration No. 1 assembly. This analysis is done to investigate the radial reaction rate profile. In this case, only the ^{235}U and ^{164}Dy detectors are used when analysing the reaction rate profiles - the information on the detectors can be found in section .2.4.

Table 37 and Table 38 present the radial distribution of ^{135}U and ^{164}Dy detector reaction rates at heights 135 cm and 205 cm, for the ASTRA critical facility Configuration No. 1. Figure 26 to Figure 29 show the ^{135}U and ^{164}Dy detector reaction rate profiles at 135 cm and 205 cm assembly heights.

Table 37: Distribution of Uranium detector(a) Reaction Rates along the Critical Assembly Radius at heights h = 135 cm and h = 205 cm for Configuration No. 1 (H_{PB} = 268.9 cm)

Height h = 135 cm					Height h = 205 cm		
j	Radial distance r_j(b), cm, translating to Channel N_j (j =1 - 9, except 8)	Reaction rate A(c) [relative units]		j	Radial distance r_j(b), cm, translating to Channel N_j (j =1 - 9, except 8)	Reaction rate A(c) [relative units]	
		Experiment(d) [10]	This Work(e)			Experiment(d) [10]	This Work(e)
1	6.75	1.124	1.173 (4)(f)	1	6.75	0.752	0.77 (2)
2	24.75	1.043	1.076 (3)	2	24.75	0.74	0.705 (-5)
3	45.15	0.762	0.764 (0)	3	45.15	0.515	0.501 (-3)
4	64.85	0.615	0.552 (-10)	4	64.85	0.392	0.368 (-6)
5	80.35	0.587	0.572 (-3)	5	80.35	0.407	0.379 (-7)
6	90.05	0.67	0.680 (2)	6	90.05	0.462	0.455 (-2)
7	113.2	0.686	0.710 (4)	7	113.2	0.479	0.481 (0)
9	163.2	0.113	0.188 (67)	9	163.2	0.077	0.135 (75)

(a) The MCNP5 modelled uranium detectors are as specified in Table 14. Further detector information can also be found as part of section .2.4.

(b) r_j radial distances at which the uranium detectors are located in the assembly core and side reflector (at a given height h).

(c) Reaction Rates A are normalized to the uranium-235 (monitor) located in channel N1 at h = 130 cm and r_j = 6.75 cm (refer to also Figure 6).

(d) The experimental measurement of gamma activity has an associated relative error of 3% per detector (monitor and ordinary) measured.

(e) MCNP5 reaction rates tallies have a relative error less than 1% and all pass the 10 statistical checks done by MCNP.

(f) The value in brackets represents the calculated (C-E)/E difference in percentage [%].

Table 38: Distribution of Dysprosium detector[a] Reaction Rates along the Critical Assembly Radius at heights h = 135 cm and h = 205 cm for Configuration No. 1 (H_{PB} = 268.9 cm)

Height h = 135 cm					Height h = 205 cm		
j	Radial distance r_j[b], cm, translating to Channel N_j (j =1 - 9, except 8)	Reaction rate A[c] [relative units]		j	Radial Distance r_j[b], cm, translating to Channel N_j (j =1 - 9, except 8)	Reaction Rate A[c] [relative units]	
		Experiment[d] [10]	This Work[e]			Experiment[d] [10]	This Work[e]
1	6.75	1	1 (0) [d]	1	6.75	0.584	0.656 (12)
2	24.75	1.054	0.915 (-13)	2	24.75	0.68	0.599 (-12)
3	45.15	0.669	0.642 (-4)				
4	64.85	0.554	0.46 (-17)	4	64.85	0.349	0.306 (-12)
5	80.35	0.55	0.48 (-13)				
6	90.05	0.569	0.576 (1)	6	90.05	0.405	0.385 (-5)
7	113.2	0.675	0.609 (-10)	7	113.2	0.445	0.412 (-7)
9	163.2	0.06	0.163 (171)	9	163.2	0.037	0.117 (215)

(a) The MCNP5 modelled dysprosium detectors are as specified in Table 16. More details about the detectors can also be found as part of section .2.4.

(b) r_j radial distance at which the dysprosium detectors are located in the assembly core and side reflector (at a given height h).

(c) Reaction Rates A are normalized to the detector located in channel N1 at h = 135 cm (refer to also Figure 6).

(d) The value in brackets represents the calculated (C-E)/E difference in percentage units [%].

(e) MCNP5 reaction rates tallies have a relative error less than 1% and all pass the 10 statistical checks done by MCNP.

(f) The value in brackets represents the calculated (C-E)/E difference in percentage [%].

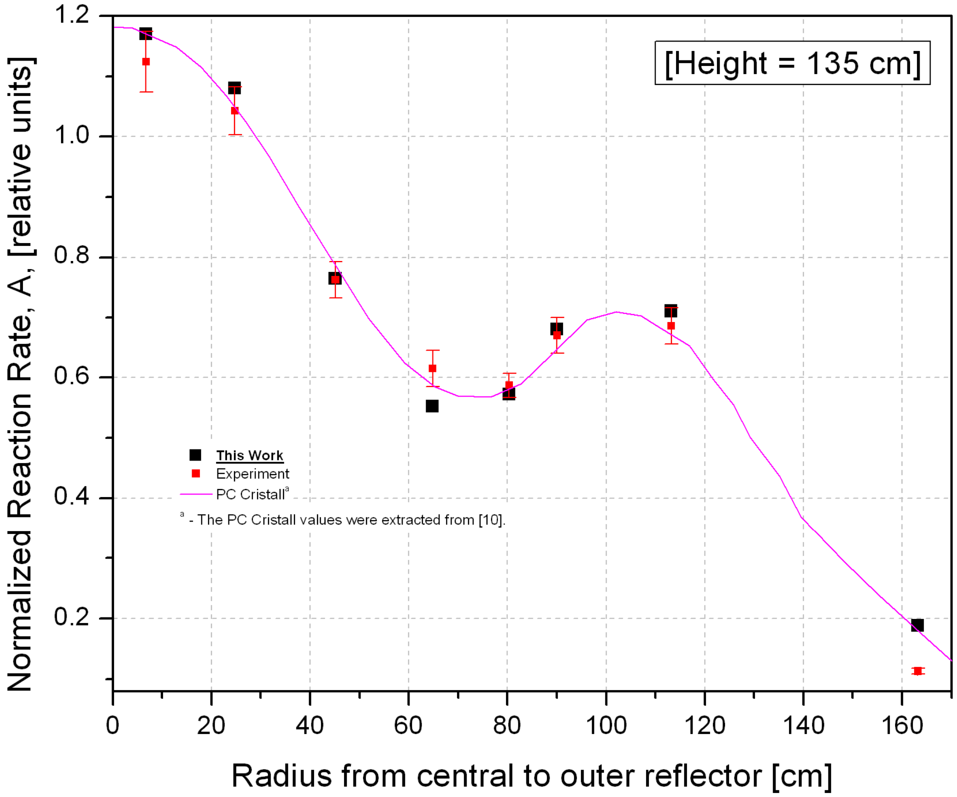

Figure 26: U^{235} detector normalized reaction rate radial profile at an axial height of 135 cm, ASTRA critical facility Configuration No. 1, H_{PB} = 268.9 cm

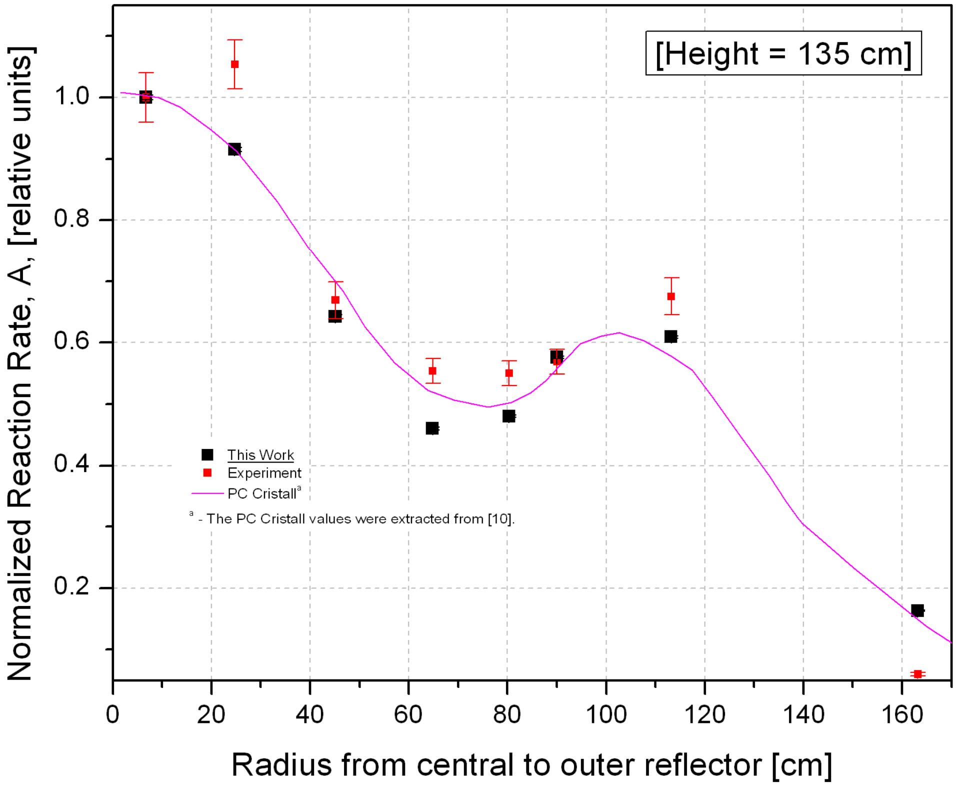

Figure 27: Dysprosium detector normalized reaction rate radial profile at an axial height of 135 cm, ASTRA critical facility Configuration No. 1, H_{PB} = 268.9 cm

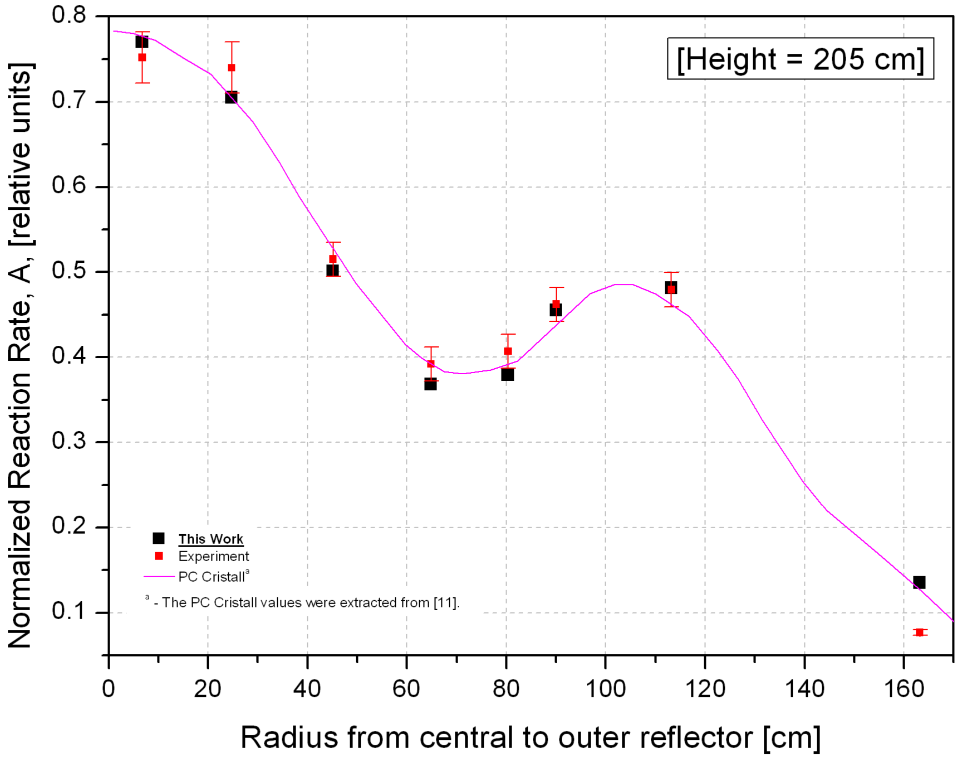

Figure 28: U^{235} detector normalized reaction rate radial profile at an axial height of 205 cm, ASTRA critical facility Configuration No. 1, H$_{PB}$ = 268.9 cm

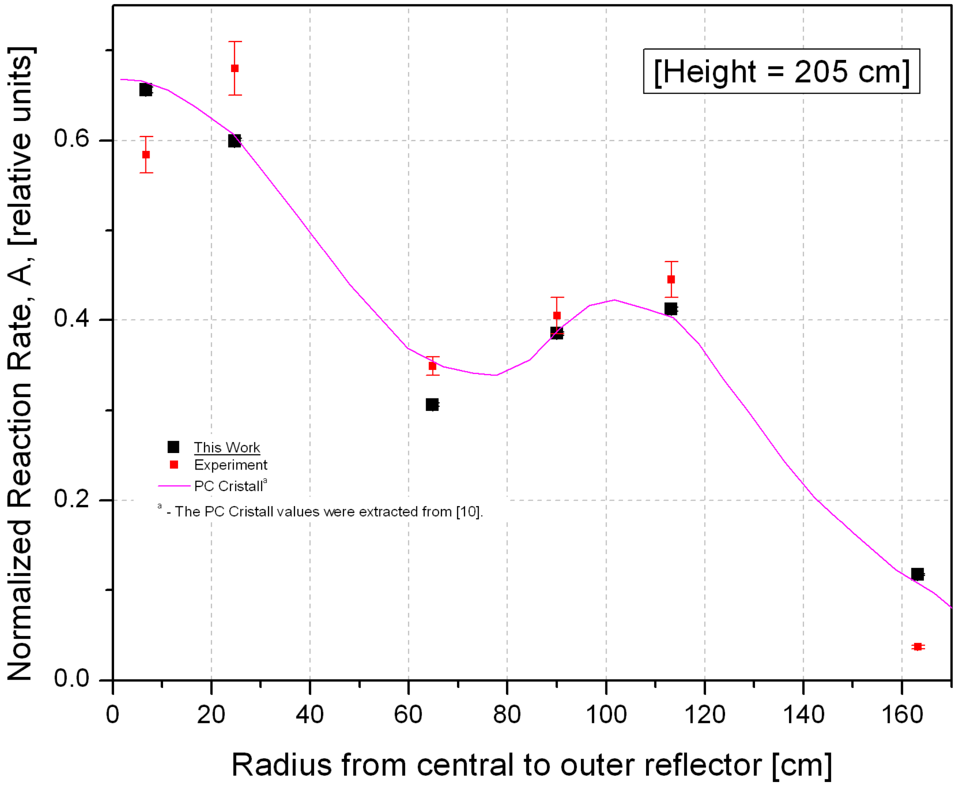

Figure 29: Dysprosium detector normalized reaction rate radial profile at an axial height of 205 cm, ASTRA critical facility Configuration No. 1, H$_{PB}$ = 268.9 cm

The MCNP5 ^{235}U detector radial reaction rate results for the height 135 cm show a good agreement with experimental results in all radial distances except the last position at the side reflector block (refer to Table 37 and Figure 26). Resultant (C-E)/E values are below 10% (generally lower than 4%); the last side reflector block reaction rate result has a value of 67%, a notable discrepancy. The MCNP5 radial reaction rate profile is mostly in agreement with the experimental one and the PC Cristall profile provides a similar profile as that provided by MCNP5. The last position calculational discrepancy seems to be overpredicted by PC Cristall in the same manner. One of the tests performed to check this discrepancy is that of adding a 5 cm thick iron material to the end surface of the outer reflector. This test was done in order to check whether we have unintentionally not included detail beyond the side reflector for our MCNP5 model of the ASTRA critical facility. No significant changes in the calculated reaction rates were identified for this test, suggesting that at least the 5 cm iron material was not one of the materials considered on the outer boundary. The lack of precise experimental information for the reactor external is a concern, especially when considering some of the available ASTRA critical facility diagrams where a definite material of some specification is part of the design (refer to Figure 30).

Figure 30: The ASTRA critical facility at the Russian Research Centre, Kurchatov Institute, Moscow [35]

The inability to represent the last side reflector position for this task confirms what we have also calculated in terms of control rod worth for CR2 in Task 2, pointing to a possibility that the modelling efforts are missing some experimental detail around the outer side reflector block.

One of the items to be addressed further in trying to find the source of the disagreement is a lack of precise experimental information around the last side reflector block. This could include the graphite plugs and most likely an external material information that is not included in the modelling effort. The effect of including this detail could affect the radial neutron spectrum at this position, and thus have a direct influence on the reaction rates experienced within different detectors located in the assembly.

The MCNP5 ^{164}Dy detector radial reaction rate results for the height 135 cm show lesser agreement with experimental results as compared to the ^{235}U detector results, once more confirming the same issue with the last position of the side reflector block (refer to Table 38 and Figure 27). Resultant (C-E)/E values are within 17% for all but the last position in the side reflector, which has a value of 171%. The PC Cristall code analysis of the same shows a similar result. Experimentally, there seems to be a suspicious measurement regarding the second point at r = 24.75 cm, it indicates the maximum reaction rate for this detector at a height of 135 cm, however all the computational tools show different as seen in Figure 27. At this stage, we have no elements to support why this is looking the way it does, there is therefore a need to address it in future.

The MCNP5 ^{235}U detector radial reaction rate results for the height 205 cm show a good agreement with the experimental results in all radial distances, except for the last position at the end of the side reflector block (refer to Table 37 and Figure 28). Resultant (C-E)/E values are below 7%; the last position in the side reflector has a value of 75%, again a notable discrepancy as discussed above. The same reasons as discussed above at h = 135 cm are suspected to be behind this discrepancy.

The MCNP5 ^{164}Dy detector radial reaction rate results for the height 205 cm show lesser agreement with experimental results, in particular the last position of the side reflector (refer to Table 38 and Figure 29). Resultant (C-E)/E values are within 12% for all but the last position in the side reflector, which has a value of 215%. The PC Cristall code analysis of the same shows a similar result.

In general, the ^{235}U detector MCNP5 radial reaction rate results show a good agreement with experimental results, apart from the last side reflector position. Even though the profiles and high-discrepancy region (last side reflector position) follow the same trends as those calculated using the ^{235}U detector, the agreement between MCNP5 and experimental results is not as good for the ^{164}Dy detectors. All the MCNP5 reaction rate results, including at the last side reflector position, have been well converged. The conclusion is that we are possibly missing some experimental detail in our modelling efforts, most likely that which deals with an outer boundary material and the said graphite plug. The effect of including this detail could affect the radial neutron spectrum at this position, and thus have a direct influence on the reaction rates experienced within different detectors located in the assembly.

CONCLUSION AND RECOMMENDATIONS

.1 CONCLUSIONS

The objective of this research was to perform validation of the MCNP model of the ASTRA facility for one of PBMR's computational tools, MCNP5, by benchmarking the code modelling of HTR cores against experimental data from the ASTRA critical facility. In doing this, the aim was to demonstrate how suitable our modelling approach, the code, and its associated cross section data are in representing the experiments. This work was done in order to add to PBMR's efforts in validating its computational tools used as part of quantifying specific nuclear physics characteristics of the reactor, whose knowledge facilitates design support and helps in defining its safety case.

This work was achieved through the development of a detailed MCNP5 model of the ASTRA critical facility and performing characteristic neutronics parameter analysis covering a selected experimental effort done at the Kurchatov Institute for a PBMR-type configuration in 1999. Only Configuration No. 1 (H_{PB} = 268.9 cm, all control rods in out positions except MR1, which is inserted to 122.8 cm above the top surface of the bottom reflector) experiments were fully addressed as part of this research.

A summary of the analysis tasks performed in order to quantify the nuclear physics parameters is presented below, along with task conclusions:

.1.1 Task 1 - Core Height

This task involved the demonstration of MCNP5 ability to predict the experimental critical height, taking into account the model specifications given. In summary, this task did not yield a good agreement between the calculation and experimental critical height. The critical height as determined by MCNP5 was 255 cm as compared to the experimental height of 268.9 cm (representing a k_{eff} overestimation in reactivity of 1 123 pcm).

A stochastic volume calculation on the MCNP5 model indicates that cutting of pebbles, introduced as a result of the modelling approach followed, results in an underestimation of the total spheres loaded in the experiment and is only 1.7% (-3% for absorber spheres, -1.9% for moderator spheres, and -1.5% for fuel spheres).

However, it is worth mentioning that the MCNP5 and Tripoli4.3 model results are in close agreement for a similar model representation and approach; the Tripoli4.3 k_{eff} overestimation in reactivity is 1 170 pcm. This provides some confidence level in knowing that another independent tool and analysis comes up with similar results, however, this does not mean that the experiment is wrong in any way.

Note that the experimental specifications provided do have an associated level of inconsistency since simple calculations using the total number of spheres loaded in the assembly and the experimentally measured loading height result in a packing fraction of 0.635, not the claimed 0.625. However, a test calculation using this packing fraction results in a higher k_{eff} overestimation in reactivity. What is clear, then, is that more information is needed to clarify this issue amongst others, however, for all the subsequent calculations the packing ratio used is 0.625.

A number of geometrical modelling, cross section and a lack of experimental information aspects that could not be satisfactorily addressed in this research are suggested for future work in section .1.2.

In conclusion, we note that MCNP5 overestimates the experimental k_{eff} value by 1 123 pcm in comparison for the same configuration set-up. More work with respect to trying to obtain a more representative model for this configuration needs to be done in future.

.1.2 Task 2 - Control rod worth depending on its position in the side reflector, individual control rod worth and the worth of a combination of rods with their interference

During this task, the suitability of MCNP5 had to be demonstrated in representing experimental results covering control rod worth as a function of its position in the side reflector, individual control rod worth, and the worth of a combination of rods with their interference.

In terms of the control rod worth as a function of its position in the side reflector, the MCNP5 and the experimental results agree well up to a position of 53 cm (measured from the core boundary), with the last two positions in the side reflector showing bad agreement (in particular the last side reflector block position).

One test was performed to understand the disagreement - this covers the plugging and unplugging of the H-13 block (against the experimental procedure of keeping the block unplugged for all the CR2 calculations). This test did not help to understand the identified disagreement, leaving us to only consider that it could possibly be because of a lack in experimental detail for the external side reflector blocks.

In terms of the individual and a combination of control rod worth results, MCNP5 agrees very well with the experimental results, predicting the worths very close to one another. MCNP5 interference coefficients therefore also predict similar trends to the experiment.

It is interesting to note that the Kurchatov Institute's own computational tool (PNK), calculates this experiment with very similar results to those reported for MCNP5. This also gives confidence that, even though our model criticality result is overestimated by 1 123 pcm, the plant-state-to-plant-state comparison for control rod worth calculations, characterized by different rod movements, still agrees fairly well for the experiment and MCNP5.

In conclusion, MCNP5 shows a very good agreement with experimental results for most of these control rod worth calculations, with the exception of the last two CR2 positions, where the disagreement is thought to be related to a lack in detail for the side reflector blocks in the surrounding area.

.1.3 Task 3 - Control rod reactivity depending on depth of insertion in side reflector and the assembly reactivity as a function of pebble bed loading height

This task involved the demonstration of the suitability of MCNP5 in predicting experimental control rod reactivity as a function of its depth in the side reflector block and the assembly reactivity as a function of pebble bed loading height. Two control rods were selected to study the control rod reactivity as a function of its depth in the side reflector; these are CR5 and MR1.

In terms of CR5, there is generally a good agreement between MCNP5 and the experimental results for insertion depths lower than 208.4 cm (MCNP5 coordinates; refer to Table 32), and a slight challenge in maintaining this agreement in the few insertion depths above this point. This is identified as due to the very close plant states for the two cases, which makes it difficult to separate respective results from the two with poor convergence. The two cases were further converged to a satisfactory point. After this, the MCNP5 calculated control rod worth shape and results are quite close to the experimental results, thus showing a good representation of the experiment.

In terms of MR1, the agreement between MCNP5 and experimental results is not as good as in CR5. The need to converge these results is important, not only as a result of close plant states (in particular at the initial CR insertion positions), but also the total reactivity of this rod, being quite small as compared to that of the CR5. After addressing the convergence issue, the MCNP5 control rod worth shape and results show a good agreement with experimental results, thus also indicating that this experiment has been represented fairly well.

Note that the above good control rod worth results comparisons are despite the challenges associated with uncertainty in the experimental detail of the control rods and graphite plugs.

In terms of the assembly reactivity as a function of the pebble bed loading height, the MCNP5 results agree very well with the experimental results. When comparing pebble layer reactivity, in general there is not as good an agreement between the experimental and MCNP5 results. This is understood be to mainly due to the overall sphere cutting ratio of the modelled layers as compared to modelling the total assembly. The sphere cutting ratio for pebble layer loading due to our modelling approach is higher than when considering an assembly, thus making it understandable to expect more disagreements for this comparison as compared to the assembly reactivity one.

In conclusion, there is a good agreement between the MCNP5 and experimental results when analysing the control rod worth as a function of its insertion depth in the side reflector, more so for CR5 than for MR1. It is also important to note that despite the model k_{eff} overestimation (Task 1), the control rod differential reactivity comparisons between the MCNP5 and experimental results using the same model for different plant states (covering the different insertion depths of the rods) are quite good. The MCNP5 assembly reactivity results in comparison to experimental results are also quite good. However, there is a modelling approach sphere cutting issue for the pebble layer loading reactivity which results in not as good an agreement for those MCNP5 results as compared to the experimental results.

.1.4 Task 4 - Spatial distribution of reaction rates in axial and radial directions

In this task, the suitability of MCNP5 had to be demonstrated in representing the spatial distribution of reaction rates in axial and radial directions. The reaction rates were first calculated in two axial channels (N1 - r_1 = 6.75 cm and N5 - r_5 = 80.35 cm) using three types of detectors for channel N1, ^{235}U, ^{115}In and ^{164}Dy; and only the ^{235}U detector for channel N5. Following this, reaction rates radial profiles were calculated in two fixed axial heights (h = 135 and 205 cm). In the case of the radial profiles reaction rate distribution, two types of detectors were used, the ^{235}U and ^{164}Dy detectors.

In terms of ^{235}U axial reaction rates in channel N1, there is a very good agreement between the MCNP5 results and the experimental results. The MCNP5 results for the other detectors in channel N1 show lesser agreement with the experimental results, with the ^{115}In detector the worst at agreeing with the experimental results. The challenges associated with this lack of agreement for the indium and dysprosium detectors have not been studied in the current effort due to time constraints. This will be further discussed as part of future work in the following subsection.

In terms of ^{235}U axial reaction rates in channel N5, there is very good agreement between the MCNP5 results and the experimental results in the last top-third of the detector points, however, all those in the bottom two-thirds do not agree as well, albeit also showing a good agreement. It must be mentioned that we do not fully understand the reason for this shape change in the bottom two-thirds of the channel.

In terms of the ^{235}U radial profile reaction rate results calculated by MCNP5 for the two heights (135 cm and 205 cm), there is a very good agreement with the experimental results for all but one position, at the last side reflector graphite block, where a clear discrepancy is identified. We envisage this discrepancy to be as a result of a lack of precise experimental information at this region. There are two experimental information aspects to investigate, namely the outer reactor boundary material and the immediate graphite block plug.

In terms of the ^{164}Dy radial profile reaction rate results calculated by MCNP5 for the two heights (135 cm and 205 cm), there is a slight lack of agreement with the experimental results for all the positions, and a complete lack of agreement in the last side reflector position. In this case, apart from seeking more precise experimental information about the last graphite plug and an outer reactor boundary material, more needs to be done in terms of an analysis of the reactor neutron spectrum profile and convergence considerations. This is discussed further in the future work section to follow (.2).

In conclusion, the MCNP5 and experimental results for ^{235}U detectors used to calculate the N1 axial and the radial profiles at two heights (h = 135 cm and 205 cm) agree well with each other. However, the ^{235}U MCNP5 results for channel N5 have a non-understood profile change for the lower third of the channel. There is a general challenge in obtaining good MCNP5 results at the last side reflector block, something that has been suggested to be as a result of a lack of precise experimental information for the outer reactor boundary material and the immediate graphite plug. There is also a general challenge in obtaining good agreement for other detectors (^{164}Dy, and to a lesser extent ^{115}In), something that has not been investigated in this effort, and it is planned as part of future tasks.

The above summary on each task indicates that MCNP5 generally does relatively well in predicting the experimental results (nuclear physics parameters), however, there are areas of concern, both experimentally and in our MCNP5 consideration (both for reactivity and reaction rate results). Concerning the experimental uncertainty, the MCNP5 results on the last side reflector block seem to consistently lack agreement with their experimental counterparts (something that is also seen from the Kurchatov Institute's tools used to calculate the same results), forcing us to consider a lack of precise experimental information to be behind our models not being representative enough of the experimental set-up. On the model uncertainty, as previously discussed, the arrangement of moderator, fuel and absorber spheres in the reactor cavity (in particular the core region) and the neutron flux spectrum and profiles throughout the assembly need to be investigated in future.

.2 RECOMMENDATIONS FOR FUTURE WORK

Recommendations for future work related to this research project are detailed below:

.2.1 The MCNP5 ASTRA Critical Facility Model

.2.1.1 Sphere arrangement

The current MCNP5 model for the ASTRA critical facility was built to address calculation tasks focused on Configuration No. 1 of the four main configurations investigated at the facility. This, as explained in Chapter 0, is characterized by a pebble bed height of 268.9 cm, and all the control rods in out positions, except for the MR1 control rod, which is located 122.8 cm above the top surface of the bottom reflector.

Stochastic volume calculations (Appendix C) on this model indicate that an overall sphere volume representation of -1.7% (644 less spheres).is seen for the MCNP5 model. The highest misrepresentation to the modelled spheres is that of the absorber spheres, which are 3% less in the assembly, followed by the moderator spheres (-1.9%) and fuel spheres (-1.5%), respectively.

It is suggested that in future studies, different arrangements of moderator, absorber and fuel spheres are studied, particularly in the core region. This study is expected to contribute towards the understanding of the difference seen in the MCNP5 model as part of calculating the critical pebble bed height, with the current model reporting an overestimation in k_{eff} of 1 123 pcm.

.2.1.2 Neutron flux profiles and spectra

Understanding of the neutron flux profiles would help to interpret the different interference coefficients and their meaning as part of control rod worth for a combination of rods.

Neutron spectrum is important to study in order to gain insight in the way neutron transport is done throughout the assembly, and also to understand the specific detector type's sensitivity in the reactor's neutron spectrum. The other important aim of studying neutron spectrum is that of ensuring proper convergence of the calculated results.

The studies detailed above are expected to ultimately provide a better understanding of the calculated reaction rates and, to a lesser extent, the control rod worth calculated with this MCNP5 model.

.2.2 The MCNP5 Nuclear Cross Section Data Evaluation

It is suggested that in future studies, the use of different nuclear cross-section data be evaluated and quantified. This study may even help identify the appropriate sets of cross sections to use in order to best cover all the model neutron physics characteristics.

.2.3 Other ASTRA Critical Facility Benchmark Evaluations

In this section, a list of all experiments done at the ASTRA critical facility to test PBMR neutron physics characteristics is provided. Table 39 provides a list of configurations that were set up and experiments done for in order to fully understand the current research effort and thus its contribution towards validation of MCNP5 modelling of HTR cores.

Table 39: A list of critical configurations of assemblies simulating the PBMR reactor at the ASTRA Facility; information from [9] and [11]

No.	Configuration	Overall Number Spherical Elements in the Assembly FS/MS/S/Total	Average Height of the Pebble Bed [cm]	Critical Position of Control Rods by MCNP5 Coordinates [cm]			
				CR1	CR2	CR5	MR1
1	Without the top reflector and cavity	27477/9659/1448/38584	268. 9	↑	↑	↑	122.8±26
1b	Without the top reflector and cavity	27144/9545/1434/38123	267.3	↑	↑	↑	62.1
2	Without the top reflector and cavity	29275/10311/1542/41128	285.8	↑	↑	151.3±2	↑
3	Without the top reflector and cavity	32929/11553/1734/46216	320.8	↓	↑	121.3±1	↑
4	With the top reflector and cavity	32929/11553/1734/46216	320.8	↑	↓	172.3±1	↑

↑ = Control rod fully extracted, ↓ = Control rod fully inserted

Control rods not listed in the table are fully extracted.

Note that thus far our research efforts cover Configuration No. 1. This was done for four types of experiments, covering:

a. Task 1 - Core height.
b. Task 2 - Control rod worth, depending on its position in the side reflector an individual control rod worth with their interference.
c. Task 3 - Control rod differential reactivity, depending on side reflector insertion depth and assembly reactivity as a function of pebble loading height.
d. Task 4 - Spatial distribution of reaction rates in axial and radial directions.

These experiments cover the validation effort required for Configuration No. 1 to a large extent, with a few more tests listed below which were performed under the same experimental effort with the same configuration, but are not covered in the current research effort:

a. Measurement of reactivity effects of groups of spherical Fuel, Moderator and Absorber Elements (a group of 20 spheres introduced into the central reflector experimental channel).
b. Measurement of reactivity effects of individual spherical Fuel, Moderator and Absorber Elements (once more introduced in the central reflector experimental channel).
c. Measurement of reactivity effects of graphite plugs and other materials placed in side reflector channels.

Configuration No. 1b was used in order to test different loading arrangements of Fuel, Moderator and Absorber elements in the mixing region as requested by PBMR due to circulation of spheres in the equilibrium mode of the reactor operation and due to transient modes of circulation at load following conditions. All the initial experiments (Tasks 1 to 4) were repeated for this configuration.

Configuration No. 2 was used to obtain plant criticality at a different height using different control elements, effectively covering only Task 1.

Configurations No. 3 and No. 4 were used to perform measurements of energy spectra and absolute values of neutron fluxes in different areas of the assembly with evaluation of the assembly power and kinetic parameters.

.2.4 Experimentalist Contact

A number of experimental items were modelled as appropriately as possible, however, a few needed to be clarified (for instance, by requiring more information from the experimentalists):

- The control rod design has been shown in a few ASTRA figures (including the ICSBEP [42]) to have more detail than is provided in the experimental documentation. More precise information on this could help build more accurately represented calculational models.
- The graphite plugs and side reflector blocks information seems to have a level of uncertainty when needing to represent in the model. Certainly from other sources, like the ICSBEP [42], the blocks have a more detailed design than presented in the experimental documentation. Knowledge of this detail could help build more representative calculational models.
- An outer boundary material is not included in the experimental documentation provided, however, figures of the ASTRA critical facility presented in this document clearly show that there is some sort of material represented on the boundary of the side reflector. The knowledge of this detail could resolve some of the main discrepancies revealed at those positions, and help to built more representative calculational models.

- The reported packing fraction is 0.625, however, this has been shown to not fully correspond to the other model aspects (pebble height and total number of spheres loading). The correct representation of this detail would help to build a more representative calculational model.
- The discrepancy related to the ^{235}U detector relative reaction rate experimental results; this covers the identification that the position where the normalization detector is said to be in has a relative reaction rate that is different from 1. There is also a reported uncertainty about the masses of the used detectors. More clarity on this would help in performing more appropriate analysis and representing the calculational model more accurately.

REFERENCES

The following documents are referred to in this document.

[1] Koster, A et al., *'PBMR design for the future'*, Nuclear Engineering and Design 222 (2003) 231-245.

[2] Tompkins, B et al., *'Nuclear News (March 2009 edition): 11th Annual Reference Issue',* ISSN: 0029-5574, Volume 52, Number 3, A publication of the ANS, Illinois, US, Mar. 2009.

[3] National Nuclear Regulator, Requirements for licensing submissions involving computer codes and evaluation models for safety calculations, Report RD-0016, Rev. 0, Centurion, South Africa.

[4] Ponomarev-Stepnoi, N N et al., *'Experiments on HTR criticality parameters at the ASTRA facility of the Kurchatov Institute',* Nuclear Engineering and Design 222 (2003) 215-229.

[5] Russian Research Center 'Kurchatov Institute', Task A-1.1. Creation of the Annular Core of the Critical Assembly at the ASTRA Facility at Room Temperature with Attainment of Criticality, Stage A-1.1.3. Selection and Substantiation of an Annular Core Critical Assembly Configuration Simulating the PBMR Reactor Core At the ASTRA Facility, Russian Research Center – 'Kurchatov Institute', Moscow, Russia, 6 Apr. 1999.

[6] Russian Research Center 'Kurchatov Institute', Task A-1.1. Creation of the Annular Core of the Critical Assembly at the ASTRA Facility at Room Temperature with Attainment of Criticality, SUBTASK A-1.1.10b. Documentation and Statistical Analysis for Main Physical Components of the ASTRA Facility Critical Assembly, Russian Research Center – 'Kurchatov Institute', Moscow, Russia, Oct. 1999.

[7] Russian Research Center 'Kurchatov Institute', Task A-1.2. Investigation of Annular Core Neutronics at the ASTRA Facility at Room Temperature, Report Stage A-1.2.1. Development of a detailed list of Neutronic Experiments in the Annular Core Critical Assembly Simulating the PBMR Reactor at the ASTRA Facility, Russian Research Center – 'Kurchatov Institute', Moscow, Russia, May 1999.

[8] Russian Research Center 'Kurchatov Institute', Task A-1.2. Investigation of Annular Core Neutronics at the ASTRA Facility at Room Temperature, Report Stage A-1.2.2. Performance of additional Laboratory and Chemical Analyses to determine Sizes, Density and Composition of Materials for Basic Components of the Critical Assembly, and Neutronics Calculations on the Basis of their Results, Russian Research Center – 'Kurchatov Institute', Moscow, Russia, Oct. 1999.

[9] Russian Research Center 'Kurchatov Institute', Task A-1.2. Investigation of Annular Core Neutronics at the ASTRA Facility at Room Temperature, Report Stage A-1.2.3. Investigation of Critical Parameters with Varying Height of the Pebble Bed, Worth of Control Rods depending on their position in the Side Reflector, and Differential Reactivity of the Control Rod depending on the Depth of its Insertion, with Calculational Analysis of Results Obtained, Russian Research Center – 'Kurchatov Institute', Moscow, Russia, 28 Feb. 2000.

[10] Russian Research Center 'Kurchatov Institute', Task A-1.2. Investigation of Annular Core Neutronics at the ASTRA Facility at Room Temperature, Report Stage A-1.2.4. Measurement of Reactivity Effects of Components and Materials Important for the PBMR Reactor, and of Spatial Distribution of Reaction Rates, Neutron Fluxes and Power in Axial and Radial directions in the ASTRA Facility Assembly, Russian Research Center – 'Kurchatov Institute', Moscow, Russia, 28 Feb. 2000.

[11] Russian Research Center 'Kurchatov Institute', Subtask BLP-1.2. Investigation Neutron Physical Characteristics of the Assembly Configurations 0 and 1, Report Creation of the Annular Core (Modification 1) and Performance of Experiments with this Core, Russian Research Center – 'Kurchatov Institute', Moscow, Russia, Mar. 2001.

[12] Raepsaet, X et al., TRIPOLI-4.3 Modeling of Pebble Bed configuration of ASTRA Critical Facility of the Kurchatov Institute, Topical Meeting Mathematics and Computation, Supercomputing, Reactor Physics and Nuclear and Biological Applications - M&C 2005, Avignon, Palais des Papes, France, 12-15 September 2005.

[13] Kuijper, J C, et al., HTR-N Reactor Physics and Fuel studies, 2nd International Topical Meeting on HIGH TEMPERATURE REACTOR TECHNOLOGY, Beijing, CHINA, 22-24 September 2004.

[14] Hogenbirk, A et al., HTR-PROTEUS Benchmark Calculations – Part 1: Unit cell results LEUPRO-1 and LEUPRO-2, Netherlands Energy Research Foundation (ECN): ECN-C--95-087, Petten, Netherlands, Sep. 1995.

[15] Hogenbirk, A, HTR-PROTEUS – Results of MCNP calculations for LEUPRO-1 and core 5, Netherlands Energy Research Foundation (ECN): ECN-I--97-008, Petten, Netherlands, Sep. 1997.

[16] Difilippo, F C, *'Monte Carlo Calculations of Pebble Bed Benchmark Configurations of the PROTEUS Facility',* Nuclear Science Engineering: 143, 240-253 (2003).

[17] Karriem, Z et al., MCNP Modelling of HTGR Pebble-Type Fuel, Proceedings of the Advanced Monte Carlo for Radiation Physics, Particle Transport Simulation and Applications (MC-2000) Conference, Lisbon, Portugal, 23-26 Oct. 2000.

[18] Colak, U et al., *'HTR-10 full core first criticality analysis with MCNP',* Nuclear Engineering Design 222 (2003) 263-270.

[19] Colak, U et al., *'Monte Carlo Criticality Calculations for a Pebble Bed Reactor with MCNP',* Nuclear Science and Engineering: 149, 131-137 (2005).

[20] Albornoz, F, 400 MW PBMR MCNP Core and Core Structures Model Report, Pebble Bed Modular Reactor (Proprietary) Limited, report 015684 Revision 1, Proprietary Class 2, Centurion, South Africa 05 Apr. 2006.

[21] Albornoz, F et al., MCNP Modelling of the PBMR Equilibrium core, ANS Topical Meeting on Reactor Physics - PHYSOR-2006, Vancouver, British Columbia, Canada, 10-14 September 2006.

[22] Armishaw, M et al., Particle Packing Considerations for Pebble Bed Fuel Systems, Proceedings of the International Conference on Nuclear Criticality Safety 2003 (ICNC'03) Conference, Tokaimura, Ibaraki, Japan, p. 401-405 20-24 Oct. 2003

[23] Brown, F B et al., *'Stochastic geometry capability in MCNP5 for the analysis of particle fuel',* Annals of Nuclear Energy 31 (2004) 2039-2047.

[24] Murata, I et al., *'New Sampling Method in Continuous Energy Monte Carlo Calculation for Pebble Bed Reactors',* Journal of Nuclear Science and Technology, Vol. 34, No. 8. p. 734-744, August 1997.

[25] E. Teuchert, et al., V.S.O.P. ('94) Computer Code System for Reactor Physics and Fuel Cycle Simulation Input Manual and Comments, FORSCHUNGSZENTRUM JÜLICH:Jül-2897, Jülich, Germany, Apr. 1994.

[26] X-5 Monte Carlo Team, MCNP – A General Monte Carlo N-Particle Transport Code, Version 5 - Volume I: Overview and Theory, LA-UR-03-1987, Los Alamos National Laboratory, Los Alamos, New Mexico, USA, 10 Mar. 2005.

[27] Sen, S et al., Comparison of VSOP and MCNP results of the PBMR Equilibrium core models, 3rd International Topical Meeting on High Temperature Reactor Technology, Report - C00000155, Johannesburg, South Africa, 1-4 Oct. 2006.

[28] International Atomic Energy Agency, Evaluation of High Temperature Gas Cooled Reactor Performance – Benchmark analysis related to the PBMR, GT-MHR, HTR-10 and the ASTRA Critical Facility, TECDOC TBD – draft.

[29] Bakulin, S V et al., Study of HTGR Nuclear Criticality Safety at the GROG and ASTRA facilities, International Conference on Nuclear Criticality ICNC-95, Albuquerque, New Mexico, USA, 17-21 Sep. 1995.

[30] Matzner, D, PBMR Project Status and the way forward, 2nd International Topical Meeting on High Temperature Reactor Technology, Beijing, China, 22-24 Sep. 2004.

[31] Stacey, W M, Nuclear Reactor Physics, ISBN 0-471-39127-1 (Published by John Wiley & Sons, Inc).

[32] Larsen, E W, Hybrid Monte Carlo - Deterministic Methods for Simulating Radiation Interactions with Matter, Department of Nuclear Engineering, North Carolina State University, 20 February 2003.

[33] Duderstadt, J J et al., Nuclear Reactor Analysis, ISBN 0-471-22363-8 (Published by John Wiley & Sons, Inc), 1976.

[34] Lewis, E E et al., Computational Methods of Neutron Transport, ISBN 0-471-09245-2 (Published by John Wiley & Sons, Inc)., 1984.

[35] Naidoo, D, VSOP Benchmark of the ASTRA Critical Facility with Special Emphasis on the Equivalent Control Rod Model, North-West University, Potchefstroom, South Africa, 2004

[36] Reitsma, F et al., *'Evaluating the control rod modelling approach used in South African PBMR: comparison of VSOP calculations with ASTRA experiments'*, Nuclear Engineering and Design 222 (2003) 147-159.

[37] Kugeler, K, Reactor Safety, NUCI888 course, North-West University, Potchefstroom, South Africa.

[38] Brown, F, *'Fundamentals of Monte Carlo Particle Transport',* Lecture notes for Monte Carlo course, Report reference: LA-UR-05-4983.

[39] Ivanov, K, Monte Carlo Methods and Applications, NUC E 525 Monte Carlo Methods, PBMR offices, Centurion, May 2008.

[40] Seker, V. et al, Personal communication: 'ASTRA TEST FACILITY CRITICALITY BENCHMARK RESULTS', Nuclear Energy Department, Hacettepe University, Ankara, Turkey (11 February 2009).

[41] Russian Research Center *'*Kurchatov Institute*'*, 'ASTRA Critical Facility for Experimental Neutronic Study of Modular HTGR', Russian Research Center – *'*Kurchatov Institute*'*, Moscow, Russia, 27 Apr. 1999.

[42] OECD/NEA, 'International Handbook of Evaluated Criticality Safety Benchmark Experiments', Organization for Economic Co-operation and Development/Nuclear Energy Agency, NEA/NSC/DOC(95)03 (release September 2008).

APPENDICES

.1 APPENDIX A: MONTE CARLO METHOD

.1.1 Boltzmann Transport Equation

The Boltzmann transport equation (devised by Ludwig Boltzmann) is used to describe the statistical distribution of particles in a fluid. The equation has proved useful in a number of other applications including particle distribution, which makes it suitable to be used in the treatment of nuclear reactor transport situations with limitations noted in more heterogeneous cases.

The time-independent and linear form of this equation is presented below (all details from [38]):

$$\Psi(\mathrm{r, v}) = \int \left[\int \Psi(\mathrm{r', v'}) C(\mathrm{v'} \rightarrow \mathrm{v, r'}) + Q(\mathrm{r', v}) \right] T(\mathrm{r'} \rightarrow \mathrm{r, v}) d\mathrm{r'} \tag{7}$$

where:

- $\Psi(\mathrm{r, v})$ = particle collision density
- $Q(\mathrm{r', v})$ = source term
- $C(\mathrm{v'} \rightarrow \mathrm{v, r'})$ = collision kernel, change velocity at fixed position
- $T(\mathrm{r'} \rightarrow \mathrm{r, v'})$ = transport kernel, change position at fixed velocity

The source term for the Boltzmann equation is given by:

$$Q(\mathrm{r, v}) = \begin{cases} S(\mathrm{r, v}) & \Leftarrow \text{ Fixed source} \\ S(\mathrm{r, v}) + \int \Psi(\mathrm{r, v'}) F(\mathrm{v'} \rightarrow \mathrm{v, r}) d\mathrm{v'} & \Leftarrow \text{ Fixed Source + Fission} \\ \frac{1}{K} \int \Psi(\mathrm{r, v'}) F(\mathrm{v'} \rightarrow \mathrm{v, r}) d\mathrm{v'} & \Leftarrow \text{ Eigenvalue} \end{cases} \tag{8}$$

where:

- $S(\mathrm{r, v})$ = fixed source
- $F(\mathrm{v'v, r})$ = creation operator (due to fission), particle at (r, v') creates particle at (r, v)
- K = eigenvalue

Assumptions:

- Static, homogenous medium.
- Time-independent.
- Markovian - next event depends only on current (r, v, E), not on previous events.
- Particles do not interact with each other.
- Neglect relativistic effects.
- No long-range forces (particles fly in straight lines between events).
- Material properties are not affected by particle reactions.

.1.2 Components of the Monte Carlo Method

The main components of the Monte Carlo method are discussed in detail in the following sections, and all the details have been taken from [39].

.1.3 Random Variable (RV)

In a Monte Carlo process, events are mapped onto numerical values for mathematical treatment. The numerical values essentially capture only the mathematical properties; which are necessary to answer probabilistic questions. These numerical values are called random variables.

There are two types of random variables; the discrete and continuous random variables. Discrete random variables are characterized by taking on one of specific values, each with some sort of probability greater than zero. Continuous random variables are considered with any of a range of values e.g. real numbers in a set [0, 1], and so there are a number of ranges (e.g. 0 to ½) that have a probability of occurring greater than zero.

A random variable has an associated probability distribution (discrete random variable) or probability density function (continuous random variable).

.1.4 Random Number (RN)

This refers to a sequence of numbers with the characteristics that the occurrence of each number is unpredictable. To assure this unpredictability (randomness), the numbers have to pass randomness tests.

.1.5 Random Number Generator (RNG)

This refers to a source of random numbers uniformly distributed on the unit interval. There are two general approaches for generating random numbers:

- Experimental (tables, on-line) - an experiment is used to generate a sequence of random numbers, which are saved in computer memory as tables.
- Algorithmic (deterministic) - an algorithm is used to generate random numbers. Because of its deterministic nature, this random number is commonly called the ‘pseudo-random’ number generator (PRNG), with its associated random numbers called ‘pseudo-random numbers’.

There are several factors which need to be respected by either of the random numbers, and this determines which random number generator to choose for a particular application. These factors include;

- Randomness.
- Reproducibility.
- Length of the sequence of random numbers.
- Computer memory.
- Generating time.
- Computer time.

The algorithmic random number generator is one of the most practical RNGs to use, since its sequence is reproducible and it requires minimal effort (computer resources, engineer time). Algorithmic random number generators are grouped into two types, namely the Congruential and Fibonacci generators. The Congruential RNG is based on integer generation proposed by D H Lehmer. It uses a formulation of the form:

$$x_{k+1} = ax_k + c \quad \mathrm{mod}\, M,\ for\ c < M < IMAX \tag{9}$$

where x_0(or seed), a, c, and M are all given integers.

The Fibonacci RNG is a floating point generator. It is characterized by computing a new number by a combination (difference, sum, or product) of two preceding numbers. It uses a formulation of the form:

$$x_{k+1} = x_{k-17} - x_{k-5} \tag{10}$$

where the Fibonacci lags 17 and 5.

.1.6 Probability Distribution Functions (PDFs)

A probability density function is defined for both discrete and continuous random variables as follows:

.1.6.1 Discrete Random Number PDF

The PDF, $p(x)$, is defined as the probability that the outcome of a random process is x_n. As an example for a well-balanced cubical die, the probability of any given event x_n (=1, 2,… or 6) is given by:

$$p(x_n) = \frac{1}{6}, \quad for\ n = 1,6 \tag{11}$$

Note that the PDF is normalized such that the probability of getting any of the possible outcomes is exactly 1.

.1.6.2 Continuous Random Number PDF

The $p(x)dx$ is the probability that the random variable (x) will assume a value in the range of x and $x+dx$. Note that $p(x)$ is defined such that the probability of getting some value x in the range [a, b] is equal to 1.

.1.7 Cumulative Distribution Functions (CDFs)

A cumulative density function is defined for both discrete and continuous random variables as follows:

.1.7.1 Discrete Random Number CDF

The CDF, $P(x)$, is defined as the probability that the outcome of a random process has a value not exceeding x_n. As an example for the cubical die, we have:

$$P(x_n) = \sum_{i=1}^{n} p(x_i), \quad for\ n = 1,6 \tag{12}$$

.1.7.2 Continuous Random Number CDF

$P(x)$ is defined as:

$$P(x) = \int_a^x dx'\, p(x') \tag{13}$$

which represents the probability that the random variable will assume a value not exceeding x.

.1.8 Fundamental Formulation of Monte Carlo

If we can assume that we can generate the random numbers, we would like to obtain the random variable (x) corresponding to a random process with $p(x)$. Let us consider that the random variable (x) is related to the random number η; hence we can write:

$$p(x)dx = q(\eta)d\eta, \quad for\ a \le x \le b\ and\ 0 \le \eta \le 1 \tag{14}$$

Then we may integrate both sides of this equation in ranges of [a, x] and [0, η] to obtain:

$$\int_a^x dx'\, p(x') = \int_0^\eta d\eta'(1)$$

or

$$P(x) = \eta \tag{15}$$

This equation gives a relation for obtaining a continuous random variable x using a random number η. The discrete random number variables are dealt with in the following way: since random number η is a continuous variable, while a discrete random variable (n) only assumes certain values, we set the following relations:

$$\min[P(n)] \ge \eta \tag{16}$$

This means that the first n which leads to a $P(n)$ greater than or equal to η would be the selected random variable.

More information about the usage of this methodology in developing physical processes, i.e. determination of free-flight path-length, selection of interaction type, the selection of scattering angle, and a Monte Carlo algorithm for estimation of transmitted particles is provided in [39], where all the information used for this section has been extracted from.

.1.9 Sampling Procedure

Building from the FFMC section above in terms of the physical process development (sampling), one needs to simulate each physical process numerous times to achieve an acceptable standard deviation. This means that the FFMCs for different types of physical processes as discussed in the previous section are also used repetitively. However, due to the problem considered or the type of physical process considered, the solution to the FFMC can be complicated and time-consuming. It is therefore necessary to devise efficient procedures to address the solution to the FFMC.

Assuming an understanding of the FFMC components, we can start to demonstrate the relevance of these relationships to the Monte Carlo calculations. A uniformly distributed [0, 1] sequence of numbers, η is provided by random number generators (RNGs). The FFMC allows us to then use the RNG to sample uniformly distributed $P(x)$ in an unbiased manner: therefore $P(x) = \eta$. It follows then that by repeatedly calling the RNG for values of η, we obtain an unbiased distribution $P(x)$ values. However, we need to sample the distribution of x and not $P(x)$.

Therefore, we must perform the inversion $x = P(\eta.)^{-1}$ after each call to the RNG. This step is very important for the accurate and economical Monte Carlo simulation of particle transport, since it ensures the proper representation of the physical processes. All the information used to compile this section is taken from [39].

A few inversion techniques have been devised and a brief summary of each is provided in the following sections:

.1.9.1 Analytical Inversion

This is a common technique for inversion, which is also regarded as the most accurate since there is direct use (no pre- and post-processing) of data. The FFMC is inverted to obtain a formulation for the random variable x in terms of random number η; equation shown below:

$$x = P(\eta)^{-1} \tag{17}$$

.1.9.2 Numerical Inversion

In cases where analytical inversion is impractical or impossible to implement, we then proceed with following a numerical procedure as discussed below:

a. We partition the PDF (defined in [a, b]) into N equiprobable intervals [C_{j-1}, C_j], such that C_0 = a, C_N = b, and:

$$\int_{C_{j-1}}^{C_j} p(x)dx = \frac{1}{N} \tag{18}$$

$$p_j = \frac{1}{N(C_j - C_{j-1})}, \quad j = 1, N \tag{19}$$

b. Generate two random numbers (η_1 and η_2).

c. Select an interval using:

$$j = INT(N \cdot \eta_1) + 1 \tag{20}$$

d. Select (or sample) random variable $\boldsymbol{x}$ within jth interval using:

$$x = C_{j-1} + \eta_2 (C_j - C_{j-1}) \tag{21}$$

.1.9.3 Probability Mixing Method

If the PDF, $p(x)$ can be partitioned into n non-negative functions, i.e.

$$p(x) = \sum_{i=1}^{N} p_i(x), \quad p_i(x) \geq 0, \quad a \leq x \leq b \tag{22}$$

then, rather than forming the FFMC formulation, we may sample x from a two-step procedure:

a. Sample the i-th function according to:

$$\sum_{i=1}^{i-1} p_i^{'} \leq \eta_1 \leq \sum_{i=1}^{i} p_i^{'} \tag{23}$$

where $p_i = \int_a^b p_i(x)dx$

b. Sample x by performing the FFMC for the $p_i(x)$ function given by:

$$\eta_2 = P_i(x) = \left(\frac{1}{p_i}\right)\int_a^x p_i(x')dx' \tag{24}$$

.1.9.4 Rejection technique

Once more this method is only applied when the analytical inversion is impractical or impossible to implement and when exact computation of $p(x)$ (i.e. PDF) is straightforward, we may consider the rejection technique as discussed below:

a. Enclose $p(x)$ by a frame $P_{max}(b-a)$; refer to Figure 31:

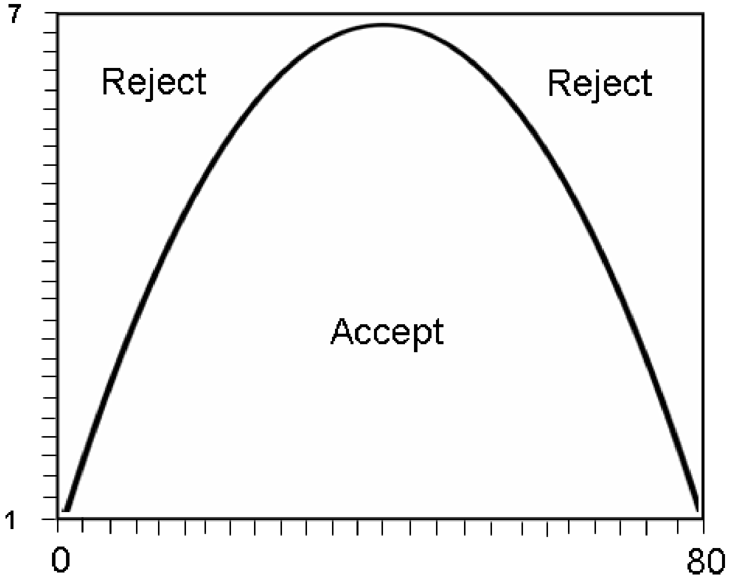

Figure 31: An illustration of the rejection method

b. Generate two random numbers η_1 and η_2.

c. Sample random variables x using:

$$x = a + \eta_1(b-a) \tag{25}$$

d. Accept x if:

$$\eta_2 p_{\max} \leq p(x) \tag{26}$$

Note that for this technique all the pairs ($x, y = \eta_2 p_{\max}$) are acceptable if they are bounded by $p(x)$, otherwise they are rejected. Only the area under the PDF (or CDF) is sampled.

.1.9.5 Numerical Evaluation

The PDF is represented as a histogram for this technique. Then its CDF is obtained using:

$$P_i = \sum_{i'=1}^{i} p_{i'}(x_{i'} - x_{i'-1}), \quad for \quad i = 1, n \tag{27}$$

Hence, $P(x)$ can be determined via:

$$P(x) = \frac{x - x_{i-1}}{x_i - x_{i-1}} P_i + \frac{x_i - x}{x_i - x_{i-1}} P_{i-1} \tag{28}$$

The FFMC for $\boldsymbol{x}$ reads as:

$$\eta = \frac{x - x_{i-1}}{x_i - x_{i-1}} P_i + \frac{x_i - x}{x_i - x_{i-1}} P_{i-1} \tag{29}$$

Therefore, $\boldsymbol{x}$ is sampled as:

$$x = \frac{(x_i - x_{i-1})\eta - x_i P_{i-1} + x_{i-1} P_i}{P_i - P_{i-1}} \tag{30}$$

.1.9.6 Table look-up

In this technique, tables of x-η are developed following the analytical inversion procedure and this data is stored in the computer memory to be used when the calculation is done. As an example, typical χ^2 distribution tables are used.

.1.10 Scoring (or Tallying)

In a particle transport problem, there are a number of nuclear physics parameters that require quantification; these may include particle flux, current, reaction rate, heating, radiation damage, etc. The use and importance of such parameters along with the basic neutron transport fundamentals for their definition are as explained in section .1. This section discusses tallying in steady-state and time-independent systems.

.1.10.1 Tallying in a steady-state system

In a steady-state system, it is important to determine the distribution of particles in the overall system. As an example, one may sub-divide the Monte Carlo model to look at I spatial volumes (ΔV), J energy intervals (ΔE), and K angular bins ($\Delta\Omega$), and perform particle tallying (counting) for each division. There are four commonly used techniques for scoring (or tallying); these include the:

- Collision estimator.
- Path-length estimator.
- Surface-crossing estimator.
- Analytical estimator.

The following sections present the four common scoring techniques considered for a steady-state system.

.1.10.1.1 Collision estimator

As it was explained above, here we discretized the space, energy and angle domains into I, J, and K intervals, respectively. Then, we score any particle of weight w moving into direction $\hat{\Omega}$ within $\Delta\Omega_k$, with energy E within ΔE_j, which has a collision within ΔV_i.

Let us consider a collision counter array given by $C(i, j, k)$; then this counter gets increased by the particle weight following this relation:

$$C(i, j, k) = C(i, j, k) + w \tag{31}$$

Note that for no ‘biasing’ in the problem, the particle weight equals 1.

Let us then have a look at the collision density after H histories:

$$g(\overline{r}_i, E_{j,} \hat{\Omega}_k) = \frac{C(i, j, k)}{H \Delta V_i \Delta E_j \Delta\Omega_k} \left\{ \frac{\dfrac{collision}{steradian - cm^3 - eV - s}}{\dfrac{source}{s}} \right\} \tag{32}$$

and the angular flux is given by:

$$\psi(\overline{r}_i, E_{j,} \hat{\Omega}_k) = \frac{g(\overline{r}_i, E_{j,} \hat{\Omega}_k)}{\Sigma_t(E_j)} \left\{ \frac{\dfrac{collision}{steradian - cm^3 - eV - s}}{\dfrac{source}{s}} \right\} \tag{33}$$

where Σ_t is the total cross section.

Integrating the angular flux along all the angular intervals, we are able to obtain a scalar flux representation, given below:

$$\phi(\overline{r}_i, E_j) = \sum_{k=1}^{K} g(\overline{r}_i, E_{j,} \hat{\Omega}_k) \Delta\Omega_k = \frac{\sum_{i=1}^{K} C(i, j, k)}{H \Delta V_i \Delta E_j \Sigma_t(E_j)} \left\{ \frac{\dfrac{collision}{cm^2 - eV - s}}{\dfrac{source}{s}} \right\} \tag{34}$$

and the rate of reactions of any type (c) as:

$$R_c(\overline{r}_i) = \sum_{j=1}^{J} \phi(\overline{r}_i, E_j) \Sigma_c(E_j) \Delta E_j = \frac{\sum_{j=1}^{J} \dfrac{\Sigma_c(E_j)}{\Sigma_t(E_j)} \sum_{k=1}^{K} C(i, j, k)}{H \Delta V_i} \left\{ \frac{\dfrac{reactions}{cm^3 - s}}{\dfrac{source}{s}} \right\} \tag{35}$$

where Σ_c is the cross section of type c.

Note that this estimator is not effective in optically thin media, where the interaction probability is low.

.1.10.1.2 Path-length estimator

This estimator was devised to address the major shortcoming of the collision estimator (inefficiency in optically thin media). The path-length estimator is derived based on the fact that the particle flux can be defined as the total path-length of particles in a volume.

The estimator sums over the path-length of particles: with any particle of weight w moving in direction $\hat{\Omega}$ within $\Delta\Omega_k$, with energy E within ΔE_j, which traces a path-length within volume ΔV_i counted.

A counter for path-length estimator can be defined as:

$$p(i,j,k) = p(i,j,k) + w \cdot p \tag{36}$$

Note that particles can leave different forms of traces in a volume:

- Path-length starts in the volume and ends outside the volume.
- Path-length starts and ends in the volume.
- Path-length starts on the boundary and ends inside the volume.
- Path-length starts and ends on the boundary.

We may then use the counter $(p(i,j,k))$ to estimate the angular and scalar fluxes. The angular flux may be given by:

$$\psi(\overline{r}_i, Ej, \hat{\Omega}_k) = \frac{p(i,j,k)}{H\Delta V_i \Delta E_j \Delta\Omega_k} \left\{ \frac{\dfrac{path-length(cm)}{steradian-cm^3-eV-s}}{\dfrac{source}{s}} \right\} \tag{37}$$

and for the scalar flux we may write:

$$\phi(\overline{r}_i, E_j) = \frac{\sum_{k=1}^{K} p(i,j,k)}{H\Delta V_i \Delta E_j} \left\{ \frac{\dfrac{path-length(cm)}{cm^3-eV-s}}{\dfrac{source}{s}} \right\} \tag{38}$$

In order to estimate the reaction rate, we define a different counter given by:

$$CP(i,j) = CP(i,j) + w\Sigma_c(E) \tag{39}$$

where Σ_c is the probability per unit length for the reaction of type c. By considering the above formulation, the reaction rate formulation is given by:

$$Rc(\overline{r}_i) = \frac{\sum_{j=1}^{J} CP(i,j)}{H\Delta V_i} \left\{ \frac{\dfrac{reaction}{cm^3-s}}{\dfrac{source}{s}} \right\} \tag{40}$$

.1.10.1.3 Surface-crossing estimator

This estimator is used when a surface is considered instead of a volume, as in the case of the collision and path-length estimators. In order to reduce a volume into a surface, the thickness of the volume would have to be decreased, however, this results in loss in accuracy since less particles can travel in that volume, hence the need for an introduction of a surface estimator. This technique is used to estimate the current and flux at a surface, these are discussed below.

.1.10.1.3.1 Estimation of partial and net current densities

In order to estimate energy-dependent current densities, we develop a counter to account for any particle weight (w), with direction $\hat{\Omega}$ and energy E within ΔE_j, crossing the normal component of surface area $\Delta A_i \hat{n}$. To distinguish between those particles which are moving to the left and those moving to the right, we devise the following counter:

$$SC(i,j,kk) = SC(i,j,kk) + w * \left| \hat{n} \cdot \hat{\Omega} \right| \tag{41}$$

Where kk = 1 or 2 refers to the positive or negative senses of the surface, respectively. Accordingly, the positive and negative currents are given by:

$$J_+(\overline{r}_i, E_j) = J_{(\hat{n}\cdot\hat{\Omega}>0)}(\overline{r}_i, E_j) = \frac{SC(i,j,1)}{H \Delta A_i \Delta E_j} \left\{ \frac{\frac{\text{no. of particles}}{cm^2 - eV - s}}{\frac{source}{s}} \right\} \tag{42}$$

and

$$J_-(\overline{r}_i, E_j) = J_{(\hat{n}\cdot\hat{\Omega}<0)}(\overline{r}_i, E_j) = \frac{SC(i,j,2)}{H \Delta A_i \Delta E_j} \left\{ \frac{\frac{\text{no. of particles}}{cm^2 - eV - s}}{\frac{source}{s}} \right\} \tag{43}$$

respectively. The net current density through the surface μA_i is given as:

$$J_{net}(\overline{r}_i, E_j) = J_+(\overline{r}_i, E_j) - J_-(\overline{r}_i, E_j) \left\{ \frac{\frac{\text{no. of particles}}{cm^2 - eV - s}}{\frac{source}{s}} \right\} \tag{44}$$

.1.10.1.3.2 Estimation of flux on a surface

The surface-crossing estimator can also be used to estimate flux of volumetric quality. As explained in the previous section, the only major consideration is that of a thin enough volume thickness (in this case consider a foil) Δx and area ΔA. We may use the path-length estimator to estimate the flux within the volume $\Delta V_i = \Delta A_i \Delta x_i$ for particles with energy E within ΔE_j as:

$$FP(i,j) = F(i,j) + w \cdot p \tag{45}$$

It can then be shown that a scalar flux can be computed by using the following equation:

$$\phi(\overline{r}_i, E_j) = \frac{FP(i,j)}{H \Delta V_i \Delta E_j} \tag{46}$$

It can also be shown that substituting for $\Delta V_i = \Delta A_i \Delta x_i$ and introducing a new counter:

$$FS(i,j) = FS(i,j) + w \frac{1}{\left| \cos\theta \right|} \tag{47}$$

One can write the scalar flux in this format:

$$\phi(\overline{r}_i, E_j) = \frac{FS(i,j)}{H \Delta A_i \Delta E_j} \tag{48}$$

There is difficulty with this technique when considering the angle θ approaching 90°, since the FS counter tends to infinity.

.1.10.1.4 Analytical estimator

Thus far, volume and area estimators have been evaluated. It is also of interest to investigate what happens in the case of a 'point' or small volume. We consider a particle that is born or that has just had a scattering collision; the probability that it will be detected at a certain point is evaluated analytically.

Without going through a lot of detail, which is presented in [39], we can write the relevant counter as:

$$AF(i', j', k') = AF(i', j', k') + w * F_S \tag{49}$$

Where the consideration is that this counter estimates particles moving in $\Delta\Omega'$ about $\hat{\Omega}'$ with energy E' within $\Delta E'$.

Thus, the angular flux can be written as:

$$\psi(\overline{r}_i', E'_j, \hat{\Omega}'_k) = \frac{AF(i', j', k')}{H \Delta E'_j \Delta\Omega'_k} \tag{50}$$

and the scalar flux can be written as:

$$\phi(\overline{r}_i', E'_j) = \frac{\sum_{k'=1}^{K'} AF(i', j', k')}{H \Delta E'_j} \tag{51}$$

One of the advantages of this technique is that each scattered or born (source) particle results in a tally. It is also possible to obtain precise results after a few thousand histories in a highly scattering medium with this technique without the use of variance reduction techniques. Since the sampling is done far from the point of interest, this result can be very inaccurate. The technique may also lead to small weights if the particle site is far from the point of interest, or if the probability of scattering into the solid angle of interest is very small. To avoid this problem, an exclusion volume around the point of interest is introduced, which perform analog Monte Carlo within that volume.

.1.10.2 Tallying in time-dependent systems

In order to take into account time-dependence in Monte Carlo simulations, additional bookkeeping is done.

Without going into too much detail, which is available in [39], we can see what the counter, angular, and scalar flux equations look like. The time-dependent counter CFT is written as:

$$CFT(i, j, k, n) = CFT(i, j, k, n) + \frac{w}{\Sigma_t} \tag{52}$$

which collects the weight w of all particles with energy E within ΔE_j, moving in direction $\hat{\Omega}$ within $\Delta\Omega_k$, and suffers a collision within ΔV_i in time interval of $\Delta t_n = (t_{n+1} - t_n)$.

Hence we can estimate the angular flux as:

$$\psi(\overline{r}_i, E_j, \hat{\Omega}_k, \Delta t_n) = \frac{CFT(i,j,k,n)}{H \Delta V_i \Delta E_j \Delta \Omega_k} \tag{53}$$

where H represents the no. of histories considered and the scalar flux can be estimated by:

$$\phi(\overline{r}_i, E_j, \Delta t_n) = \frac{\sum_{k=1}^{K} CFT(i,j,k,n)}{H \Delta V_i \Delta E_j} \tag{54}$$

It can also be illustrated that the collision rate can also be estimated by introducing another counter that takes into account the collision cross section.

.1.10.3 Estimate variance associated with the flux or current

As discussed in previous sections, flux and different forms of currents are estimated in finite ranges of space, energy, and direction. This means that each tally volume acts as a detector of particles. In order to estimate the uncertainty associated with the flux or current, we can treat the tallying as a binary process (the particle is either detected or not).

One of the methods used to account for this uncertainty is the Bernoulli distribution, which is discussed in section .1.10.3.1; following this is a general experiment methodology (section .1.10.3.2).

.1.10.3.1 Bernoulli distribution for estimation of variance

The variance for a Bernoulli distribution is expressed as:

$$\sigma^2 = pq \tag{55}$$

Where p is the probability of success and q is the probability of failure.

In the context of the current discussion on Monte Carlo estimators, the probability of success is equal to $\frac{c}{n}$, where c is the number of counts (successes) and n is the number of experiments done. Therefore the variance is represented by:

$$S^2 = \frac{c}{n}\left(1 - \frac{c}{n}\right) \tag{56}$$

and the relative error is given by:

$$R_x = \frac{S}{\frac{c}{n}} = \frac{\sqrt{pq}}{\frac{c}{n}} = \frac{\sqrt{\frac{c}{n}\left(1 - \frac{c}{n}\right)}}{\frac{c}{n}} = \sqrt{\frac{c}{n} - 1} \tag{57}$$

Considering that the central limit theorem is valid, we can write:

$$R_{\overline{x}} = \frac{R_x}{\sqrt{n}} = \sqrt{\frac{1}{c} - \frac{1}{n}} \tag{58}$$

.1.10.3.2 General experiment with outcomes x_i's

For a general experiment with outcomes x_i, after n trials, the sample average and variance are given by:

Sample average:

$$\overline{x} = \frac{1}{n}\sum_{i=1}^{n} x_i \tag{59}$$

Sample variance:

$$S_x^2 = \frac{n}{n-1}\left(\overline{x^2} - \overline{x}^2\right) \tag{60}$$

.1.11 Statistics

Statistics make use of scientific methods of sampling when the population is unknown. The theory of statistics is closely linked to that of probability. The probability theory deals with determining the probability that an unknown sample turns out to have certain characteristics, in this case the population is considered as known. In case of statistics theory, sampling of an unknown population is done in order to estimate its composition.

In general, there are three main quantities that a statistical analysis seeks to report on, particularly when considering an unknown population. These include:

- The sample average/mean.
- The sample variance/standard deviation.
- The confidence level on the estimated mean.

The above quantities address the accuracy and precision of any Monte Carlo calculation.

The statistical theory is based on a number of fundamental components from probability theory. These include:

- True mean (for a continuous and discrete variable).
- True variance (for a continuous and discrete variable).
- Sample mean.
- Sample variance.
- Bernoulli probability law.
- Binomial distribution.
- Poisson distribution.
- Normal distribution.
- Corollary to the DeMoivre-Laplace theorem.
- Central limit theorem.
- The determination of the Confidence Level for a Monte Carlo simulation.

All of these components are discussed in detail in [39] and no further information is provided in this document.

.1.12 Variance Reduction Techniques

Variance Reduction Techniques (VRTs) are important for simulation where the probability of occurrence of an outcome of interest is very low, and thus the result obtained is not precise, accurate and timely enough. This methods apply a bias in the basics physics (represented by PDFs) of the system considered such that the quantities of interest can be estimated in a shorter time with a smaller variance.

In order to prevent an ‘unbiased’ sample mean, each particle is assigned to a statistical weight (w) which is defined based on the ‘unbiased’ and biased density functions. Weight conservation is one of the most important Monte Carlo requirements for a sound calculation and this is why weight usage within VRT is useful during the biased consideration.

There are in effect a number of variance reduction techniques which have been considered in the past and some have made it to commercial codes. Some of those are listed below:

- Implicit capture.
- Biasing the path-length to the next collision.
- Exponential transformation.
- Splitting technique.
- Source biasing.
- Point detector biasing.
- Weight window technique.
- Forced collisions.

The above list is further outlined and discussed in [39].

.1.13 Vectorization and Parallelization

The concept of vectorization and parallelization has been in development since the early 1980s with the view of designing vector and parallel hardware to increase computer performance (MFLOPS – Million Floating Point Operations per Second) by order of magnitudes.

The use of such systems has made it possible to solve complex problems that would have taken sizeable resources and long execution periods had they been considered in the conventional way (scalar and serial computers). The use of these systems is made possible through the design of new software, which can utilize vector and parallel processing capabilities of the supercomputers.

In order to gain an insight into the basis and operation of these concepts, one needs to understand the following components:

- Vector processing.
- Parallel processing.
- Vectorization of the Monte Carlo methods.
- Parallelization of the Monte Carlo method.

.2 APPENDIX B: MCNP5 CALCULATION PARAMETERS SELECTED

In order to select the parameters needed for performing criticality calculations to quantify the reactor physics parameters in section 0, a few test runs were executed for each Task. A number of items were important to control these calculations:

a. The standard deviation is an estimation of the criticality eigenvalue confidence interval. This is directly influenced by the selected total number of cycles that needs to be performed before the calculation stops and by the batch size selection.
b. In order to provide better calculational efficiency in running parallel calculations (limited communication time, i.e. fewer rendezvous), the batch size for each cycle had to be high enough.
c. The Shannon entropy is used in MCNP to test the source distribution convergence, hence the need to pay attention to it. This directly affects the choice of the cycles initially skipped and the total number of cycles that needs to be performed. This test was passed in all the calculations performed for all the tasks done.

The final selection was done as follows:

a. Task 1, 2a - batch size = 1 000 000, cycles skipped = 15, total number of cycles performed = 115 (typically, there are selected cases where many more cycles needed to be performed to ensure greater converge the results).
b. Task 2b = batch size = 200 000, cycles skipped = 15, total number of cycles performed = 115 (typically, there are select cases where a lot more needed to be performed to converge the results more).
c. Task 3a - batch size = 1 000 000, cycles skipped = 10, total number of cycles performed = 110.
d. Task 3b - batch size = 200 000, cycles skipped = 10, total number of cycles performed = 110.
e. Task 4 - batch size = 1 200 000, cycles skipped = 10, total number of cycles performed = 1 000.

.3 APPENDIX C: STOCHASTIC VOLUME CALCULATION

As explained in section .2.1, a stochastic volume calculation was done for the constructed MCNP5 model of the ASTRA critical facility. The aim was to perform checks on local and global packing fraction, sphere ratio representation, amongst other characteristic checks on the model. Table 40 presents the input data considered when performing the volume calculations for the ASTRA critical facility MCNP5 model, whilst Table 41 presents the final volume calculation results, Note that this analysis was done for the Configuration No. 1 [6] experimental benchmark.

It is worth mentioning that all total volume output results presented in Table 41 pass all 10 statistical checks performed by the MCNP code, and the relative errors from each result do not exceed 0.04%.The effect of modelling the ASTRA critical facility using the regular lattice approach results in an underestimation of the Absorber Spheres by 3%, the Fuel Spheres by 1.5%, whiles the Moderator Spheres are underestimated by 1.9%. These numbers indicate that there is a need to further study regular lattice representations that minimize the effect of cutting spheres, with the aim of better respecting the masses and ratios of fuel, absorber and moderator in each region. A fully stochastic modelling of this ASTRA configuration is not possible, due to the consideration of the total number of spheres required to model (38 584) and their respective parts (kernels, coatings, graphite matrix and shell); the cell count causes this consideration to be beyond the capabilities of MCNP.

The global underestimation of spheres is 1.7%, with no further studies done to investigate how the impact of reducing this would affect the overall reactivity. This study is part of future work activities listed in section .2. This model, however, still reports a k_{eff} result that shows an overestimation to reactivity of 1 123 pcm, which takes into account our modelling approach for loaded spheres and all other assembly components. Since the study of fully random kernels and spheres was not addressed in this work, no concluding remark can be passed about the volume representation of kernels and spheres in the reactor central cavity apart from what is in section .2 and the stochastic volume calculation results in Table 41, which indicate that sphere representation is impacted in some way by the current approach (refer to section .2).

Table 40: Stochastic volume calculation input data for the ASTRA critical facility MCNP model used (based on Configuration No. 1 experimental benchmark)

Parameter	Magnitude	Unit
Sphere outer radius	3	cm
Matrix outer radius - FS	2.5	cm
Matrix outer radius - AS	2	cm
Kernel outer radius - UO_2 - FS	0.025	cm
Kernel outer radius - B_4C- AS	0.003	cm
# UO_2 kernels per FS	4189	
# B_4C kernels per AS	4.482×10^5	
Inner radius - IRR	5.25	cm
Outer radius - IRR	36.25	cm
Outer radius - MR	52.75	cm
Pebble bed height	268.9	cm
Pebble bed packing fraction	0.625	
# of Fuel Spheres [FS]	27477	
# of Absorber Spheres [AS]	1448	
# of Moderator Spheres [MS]	9659	
Total pebble bed spheres	38584	
Ratio FS/AS/MS in Mixing Region (MR)	47.5/2.5/50	
Ratio FS/AS in Core Zone (CR)	95/5	

Table 41: Stochastic volume calculation output data for the ASTRA critical facility MCNP model used (based on Configuration No. 1)

Volume	Fuel Spheres[a] [FS]				Absorber Spheres [AS]				Moderator[b]	Helium[c]	Core[d]	Packing Fraction to[e]		Ratio of FS/total[f]	Ratio of AS/total	Ratio of MS/total
	Kernel	**Matrix**	**Shell**	**Total**	**Kernel**	**Matrix**	**Shell**	**Total**	**MS**			**Helium**	**Core**			
FR	6.50E+03	1.55E+06	1.14E+06	2.69E+06	6.14E+01	4.05E+04	9.83E+04	1.39E+05		1.71E+06	4.54E+06	0.6241	0.6241	0.9510	0.0490	0.0000
MR	8.87E+02	2.11E+05	1.54E+05	3.66E+05	8.92E+00	5.88E+03	1.40E+04	1.99E+04	3.91E+05	4.63E+05	1.24E+06	0.6269	0.6269	0.4711	0.0255	0.5034
IRR									6.80E+05	4.06E+05	1.09E+06	0.6262	0.6262			1.0000
Total	7.38E+03	1.76E+06	1.29E+06	3.06E+06	7.04E+01	4.64E+04	1.12E+05		1.07E+06	2.58E+06	6.87E+06	0.6249	0.6249			
# of Spheres																
FR	23692	23759	23911	23822	1212	1212	1235	1228	0	25145	0.9999	0.9986	0.9986	1.0010	0.9807	
MR	3237	3239	3236	3238	176	176	176	176	3460	6819	0.9997	1.0030	1.0030	0.9918	1.0219	1.0067
IRR	0	0	0	0	0	0	0	0	6015	5984	0.9996	1.0019	1.0019			1.0000
Total	26929	26998	27147	27061	1388	1388	1411	1404	9475	37948	0.9998	0.9999	0.9999			
# spheres DTR	-548	-479	-330	-416	-60	-60	-37	-44	-184	-636						
% DTR	-2.0%	-1.7%	-1.2%	**-1.5%**	-4.1%	-4.2%	-2.6%	**-3.0%**	**-1.9%**	-1.6%						
Total # spheres in RCC	37940															
% DTR	-1.7%															

FR - Fuel Region; MR - Mixing Region; IRR - Inner Reflector Region; DTR - Difference to Reference; RCC - Reactor Central Cavity

[a] These volume calculations represent the total volume occupied by parts making up the Fuel Sphere in a specific region where the FS is located (e.g. total kernel volume of the FS in the FR, MR and IRR). The same analogy applies when considering the Absorber Spheres volume calculations.

[b] These volume calculations represent the total Moderator Spheres volume in each region where it is located (e.g. total volume occupied by Moderator Spheres in MR and IRR)

[c] These volume calculations represent the total volume occupied by helium in each region (e.g. total helium volume in the FR, MR and IRR).

[d] These volume calculations represent the total volume of each region (FR,MR and IRR).

[e] This packing fraction to Helium calculation is done per region and represent the ratio of the sum total volume occupied by all parts of the Fuel, Absorber and Moderator Spheres to the sum total volume occupied by all parts of the FS, AS, MS and helium for that region. The packing fraction to core calculation is done in the same way but not taking into account the helium volume in the calculation.

[f] These calculations are done to check the representation of the fraction of spheres of interest (FS, AS and MS) to all spheres modelled in that particular region.